Optical design of titania films in dye-sensitized solar cells and perovskite solar cells

Dissertation

von

Bo Su

Technische Universität München
Physik-Department
Lehrstuhl für Funktionelle Materialien
2018

TECHNISCHE UNIVERSITÄT MÜNCHEN
Physik-Department
Lehrstuhl für Funktionelle Materialien

Optical design of titania films in dye-sensitized solar cells and perovskite solar cells

Bo Su

Vollständiger Abdruck der von der Fakultät für Physik der Technischen Universität München zur Erlangung des akademischen Grades eines

Doktors der Naturwissenschaften (Dr. rer. nat.)

genehmigten Dissertation.

Vorsitzende:		apl. Prof. Dr. Norbert Kaiser
Prüfer der Dissertation:	1.	apl. Prof. Dr. Peter Müller-Buschbaum
	2.	Prof. Dr. Friedrich C. Simmel

Die Dissertation wurde am 07.03.2018 bei der Technischen Universität München eingereicht und durch die Fakultät für Physik am 03.04.2018 angenommen.

ABSTRACT

Mesoporous titania is a cheap and widely used material for photovoltaic applications. To enable a large-scale fabrication with a controllable pore size, a diblock copolymer-assisted sol-gel route based on spray coating is chosen, in which polystyrene-block-polyethylene oxide is used as the structure-directing template. The dominant structure features of titania films are not just influenced by the sol-gel recipe but also by the spray protocols. Furthermore, periodic structures within mesoporous titania films used in photovoltaic devices are successfully prepared via wet-imprinting for dye sensitized solar cells and perovskites solar cells via photolithography approaches. To investigate the mechanism of plasmonic enhancement in quasi-2D perovskite films, gold-titania core-shell nanoparticles are deposited on structured titania films, followed by the deposition of a quasi-2D perovskite layer. The short charge carrier lifetime in quasi-2D perovskite films indicates that the localized surface plasmon resonance enhances the charge carrier dissociation rates. In addition, the degradation process of a 2D/3D perovskite solar cell under moisture conditions is investigated.

Zusammenfassung

Mesoporöses Titania ist ein günstiges und gebräuchliches Material für photovoltaische Anwendungen. Um großtechnische Herstellungsverfahren und kontrollierbare Porengrößen zu ermöglichen, wird eine diblock-copolymer-basierte Sol-Gel-Methode mittels des Sprühbeschichtungsverfahrens angewandt. Hierbei dient Polystyrol-block-Polyethylenoxid als strukturgebendes Templat. Die vorherrschenden strukturellen Eigenschaften der Titaniafilme werden nicht nur von der Sol-Gel-Rezeptur/(Zusammensetzung), sondern auch von den angewandten Sprühprotokollen beeinflusst. Zudem können periodisch strukturierte nanoporöse Titaniafilme zur Herstellung von photovoltaischen Apparaten mittels Nassdruckverfahren, im Falle von farbstoffsensibilisierten Solazellen, und mittels Photolithographie, im Falle für Perovskitsolarzellen, dargestellt werden. Um den Mechanismus der plasmonischen Verbesserung in quasi-2D Perovskitschichten zu untersuchen, werden Gold-Titania Kern-Schale-Nanopartikel auf Titaniadünnfilmen aufgebracht, gefolgt von einer 2D-Perovskitschicht. Die kurze Lebensdauer der Ladungsträger in quasi-2D Perovskitfilmen weist darauf hin, dass die lokalisierte Oberflächenplasmonenresonanz die Dissoziationsrate der Ladungsträger verbessert. Des Weiteren wird der Zersetzungsprozess einer 2D/3D Perovskitsolarzelle unter Feuchtigkeitsbedingungen untersucht.

TABLE OF CONTENTS

ABSTRACT II

LIST OF ABBREVIATIONS XII

1. INTRODUCTION 1

2. THEORETICAL ASPECTS 5

2.1 Nanostructured titania films 5
2.1.1 Titania properties 5
2.1.2 Polymer basics 7
2.1.3 Basic principles of sol-gel chemistry 9
2.2 Principles of solar cells 10
2.2.1 Dye-sensitized solar cells 10
2.2.2 Perovskite solar cells 12
2.3 Localized surface plasmon resonances 15
2.4 Grazing incidence X-ray scattering 17

3. CHARACTERIZATION METHODS 21

3.1 Structural characterization 21
3.1.1 Scanning electron microscopy 21
3.1.2 Transmission electron microscopy 22
3.1.3 Atomic force microscopy 22
3.1.4 X-ray diffraction 22
3.1.5 Grazing incidence X-ray scattering 23
3.2 Spectroscopic and electrical characterization 24
3.2.1 UV-Vis spectroscopy 24
3.2.2 Photoluminescence spectroscopy 24
3.2.3 J-V characterization 25

4. SAMPLE PREPARATION 27

4.1 Materials 27
4.1.1 Sol-gel synthesis 27
4.1.2 Photolithography and imprinting materials 29
4.1.3 Perovskite materials 30
4.1.4 Other materials for solar cells fabrication 30

4.2 Processing 31
4.2.1 Synthesis of nanostructures 31
4.2.2 Deposition methods 32
4.2.3 Photolithography process and imprinting 34
4.2.4 Perovskite films fabrication 38
4.2.5 Solar cell fabrication 39

5. COMBINATION OF SOL-GEL WITH SPRAY COATING METHOD 45

5.1 Tuning of titania films thickness 46
5.2 Tuning of titania films via sol-gel recipe 48
5.2.1 Morphology 49
5.2.2 Optoelectrical properties 52
5.3 Tuning of titania films via spray parameters 53
5.3.1 Morphology 54
5.3.2 Optical characterization 55
5.4 Crystallinity tuning via calcination temperature 56
5.5 Summary 57

6. MORPHOLOGY EVOLUTION DURING SPRAY COATING 59

6.1 *In situ* spray coating GISAXS measurement 61
6.1.1 Morphology evolution during spray coating 61
6.1.2 Molding of film growth during spray coating 66
6.1.3 Morphology and crystallinity after calcination 67
6.2 Simulation of spray process 68
6.2.1 Mathematic model 69
6.2.2 Comparison of simulation data with optical images 72
6.3 Perovskite solar cell based on meso-titania 73
6.4 Summary 75

7. SUPERSTRUCTURING OF TITANIA FILMS 77

7.1 Wet imprinting 78
7.1.1 Fabrication routine 78
7.1.2 Morphology 79
7.1.3 Characterization of DSSCs based on structured titania 81
7.2 Nanoimprinting 82

7.2.1 Fabrication routine ... 82
7.2.2 Morphology ... 83
7.3 Summary ... 85

8. 2D PEROVSKITE FILM WITH PLASMONIC GOLD NANOPARTICLES ... 87

8.1 Plasmonic nanoparticles on structured titania template ... 88
8.1.1 Fabrication routine ... 89
8.1.2 Morphology ... 89
8.1.3 Optical properties ... 90
8.1.4 X-ray characterization ... 91
8.2 2D lead bromide films with plasmonic structure ... 95
8.2.1 2D/3D lead bromide layer ... 95
8.2.2 Influences of plasmonic structure on 2D lead bromide layer ... 98
8.3 Solar cell performance ... 104
8.3.1 Routine to improve the PCE of 2D PSCs ... 104
8.3.2 In-operando degradation of PSCs ... 106
8.4 Summary ... 110

9. SUMMARY AND OUTLOOK ... 113

BIBLIOGRAPHY ... 117

LIST OF PUBLICATIONS ... 135

ACKNOWLEDGEMENTS ... 139

LIST OF ABBREVIATIONS

2D	two-dimensional
3D	three-dimensional
AFM	atomic force microscopy
Au@TiO2 NPs	gold-titania nanoparticles
CB	conduction band
CdTe	cadmium telluride
CIGS	copper indium gallium selenide
c-Si	crystalline silicon
C-TiO$_2$	commercial titania paste prepared titania
D149	5-[[4-[4-(2,2-Diphenylethenyl) phenyl]-1,2,3-3a,4,8b-hexahydrocyclopent[b]indol-7-yl]methylene]-2-(3-ethyl-4-oxo-2-thioxo-5-thiazolidinylidene)-4-oxo-3-thiazolidineacetic acid
DI water	deionized water
DSSCs	dye sensitized solar cells
DWBA	distorted wave Born approximation
EIA	effective interface approximation
FF	fill factor
FK209 Co(III) TFSI	tris(2-(1H-pyrazol-1-yl)-4-tert-butylpyridine)-cobalt(III)tris(bis(trifluoromethylsulfonyl) imide)
FTIR	Fourier transform infrared spectroscopy
FTO	fluorine-doped tin oxide

GISAXS	grazing incidence small-angle X-ray scattering
GIWAXS	grazing incidence wide-angle X-ray scattering
GTRs	grating truncation rods
H_2O_2	hydrogen peroxide
H_2SO_4	sulfuric acid
HMDS	hexamethyldisilazane
HRTEM	high-resolution transmission electron microscopy
ICDD	International Center for Diffraction Data
ITO	indium tin oxide
IUPAC	International Union of Pure and Applied Chemistry
JCPDS	Joint Committee on Powder Diffraction Standards
J_{SC}	short-circuit current density
Li-TFSI	bis (trifluoromethylsulfonyl) imide lithium salt
LMA	local monodisperse approximation
LSPR	localized surface plasmon resonance
LSPs	localized surface plasmons
LUMO	lowest unoccupied molecular orbital
M_w	molecular mass
N719	di-tetrabutylammonium cis-bis(isothiocyanato) bis(2,2’-bipyridyl-4,4’-dicarboxylato)-ruthenium(II)
NIL	nano-imprint lithography
NPs	nanoparticles
PCE	power conversion efficiency
PCE	power conversion efficiency

PDI	polydispersity index
PDMS	polydimethylsiloxane
PEO	polyethylene oxide
PFOTS	1H,1H,2H,2H-perfluorooctyltrichlorosilane
PL	photoluminescence spectroscopy
PS	polystyrene
PS-*b*-PEO	polystyrene-*block*-polyethylene oxide
PSCs	perovskite solar cells
PV	photovoltaic
QW	quantum-well
RPPs	Ruddlesden-Popper perovskites
R_s	series resistance
R_{sh}	shunt resistance
SEM	scanning electron microscopy
spiro-OMeTAD	2,2’,7,7’-tetrakis (N,N di-p-methoxyphenylamine) 9,9’-spiro-bi-fluorene
SDD	sample-to-detector distance
TBP	4-tert-butylpyridine
TEM	transmission electron microscopy
Tg	glass transition temperature
TRPL	time-resolved photoluminescence spectroscopy
TTIP	titanium(IV) isopropoxide
VB	valence band
V_{OC}	open-circuit voltage

XRD	X-ray diffraction

1. INTRODUCTION

With a tremendous increase of energy consumption, a threat of fossil fuel shortage has emerged. Meanwhile, the massive emission of carbon dioxide, along with the consumption of fossil fuels, has directly led to global warming. Solar energy, as a clean and renewable energy, shows a great potential to fulfill the growing energy demand, since it is largely abundant. Bequerel discovered the photovoltaic effect in 1839,[1] then two years later the first solar cell was fabricated in Bell Laboratories with a power conversion efficiency (PCE) of 4.5%.[2] Afterwards, a rapid growth in photovoltaic (PV) industry was shown. Nowadays, the leading crystalline silicon (c-Si) solar cells reach (26.7 ± 0.5)%, and share above 90% of the PV market.[3]

Although, c-Si solar cells became the dominant photovoltaic device in the last decade, it still suffers from environmental pollution, huge energy consumption and high production costs during fabrication of the solar panels. The next generation of PV turned to cadmium telluride (CdTe) and copper indium gallium selenide (CIGS), which have a record PCE of (21.0 ± 0.4)% and (21.7 ± 0.5)%, respectively.[3] This technology still faces difficulties in large-scale industry production.[4] In 1991, dye-sensitized solar cells (DSSCs), invented by Michael Grätzelbe,[5] became a candidate as the third-generation of PV with a record of 13% on a laboratory scale.[6, 7] In this device architecture, a mesoporous titania film is used as an electron conducting layer, and it provides a large surface area to attach dye molecules. Due to the usage of liquid electrolyte, large-scale production of DSSCs may lead to instability problems. Such problems lead to the development of solid-state dye-sensitized solar cells, in which the liquid electrolyte is replaced by a hole transfer layer. Notably, Burschka et al. successfully used perovskite material to replace the dye monolayer as an absorber, and achieved a higher PCE of approximately 15% compared to DSSCs.[8] This is attributed to the unique properties of perovskite material, such as low energy direct bandgap, high absorption coefficient, balanced electron-hole mobility, high carrier mobility, a low binding energy of the photo-excited states, and a long diffusion length (L_D > 1 µm for $CH_3NH_3PbI_{3-x}Cl_x$ and ~ 100 nm for $CH_3NH_3PbI_3$). Later, perovskite solar cells (PSCs) showed the most rapid increase in performance in photovoltaic history.[9-11] The mesoporous titania with appropriate pore size and structure has been proven to enhance the performance of the device.[12-14]

In thin films photovoltaic applications, titania films with a large surface-to-volume value play an important role in boosting the PCE of solar devices. However, the usage of random orientated nanoparticles to form a mesoporous titania network has several drawbacks; for example, an inefficient electron diffusion through the random mesoporous structures is affected by a lack of control over the pore size distribution.[15-18] One way to overcome this challenge is to apply copolymers as a structure-directing template into the preparation route of the titania films.[19] Through this route, bicontinuous titania films with well-controlled pore structures can be obtained via microphase separation and micelle formation processes of the block copolymer with a titania precursor in the solution. So far, the majority of investigations using sol-gel chemistry routes still deposits films via laboratory-scale deposition methods, such as spin-coating and solution-casting.

Throughout this thesis, spray-coating is chosen as a scale-up deposition method to deposit the mesoporous titania film, which is commonly used as an electron transfer layer in thin films photovoltaics. The general aim of this study foresees how the customization of titania films influences solar cells. The graphical illustration in Figure 1.1 gives an overview of the main topics in the present thesis. Although different morphologies of titania films can be obtained by sol-gel wet-chemistry, so far, the deposition of titania film by spray-coating is rarely studied. Several key parameters of spray coating, such as spray speed, nozzle-to-sample distance, pressure and heating temperature of substrate, need to be optimized to achieve a homogenous film. Besides that, the structure of sprayed titania films is affected by the recipe of sol-gel solution and spray protocols. The question of how to achieve the tunable pore structure via varying recipes of sol-gel solution and spray protocols is answered in chapter 5. The structure evolution during spray coating is crucial to investigate, since it provides an insightful understanding of the film's formation mechanisms on a macroscale and nanoscale. Therefore, as described in chapter 6, the structure evolution is monitored by *in situ* grazing incidence small-angle X-ray scattering and the dynamical size distribution of spray droplets during spray-coating is simulated on a macroscale.

To boost the PCE of photovoltaic devices, light trapping structures are applied to the configuration of solar cells.[20-25] Significant enhancements of light absorption or charge mobilities in photovoltaic devices are reported through different approaches: (1) prolonged optical path length by superstructures or additional scattering layer;[7, 26-31] (2) plasmonic effect by metallic nanostructures or noble metal nanoparticles.[32-37] In chapter 7, mesoporous titania films with line grating structure, replicated from a blank compact disc (CD) structure, are obtained via wet-imprinting method. The wet-imprinting is applied after the blade-coating of commercial titania paste. In less than an hour, the CD structure can be sufficiently transferred to titania film. It provides an easy procedure to structure a film compared to the conventional imprinting methods that involve a complicated stamp-fabrication process and high pressure during imprinting. The depth of superstructure is crucial for PSCs, since sol-gel prepared titania films consist of copolymer and a huge loss of structure depth occurs during calcination. To overcome this, a stamp with desired structure depth is fabricated via photolithography approaches. The periodical structure is transferred from the stamp to the titania film by nanoimprinting method.

Initial studies from literatures concluded that the plasmonic enhancements in PSCs are not attributed to the increase of light harvesting. Later, there is a hypothesis which assumes that the presence of noble metal nanoparticles may favor the generation, separation, transport and collection of photon-excited species, but it is still not clearly understood. To identify the influences of the plasmonic effects in PSCs, in chapter 8, gold-titania nanoparticles ($Au@TiO_2$ NPs) with core-shell structure are employed on the structured titania films, followed by a quasi-2D perovskite layer. The samples are measured by grazing incidence wide-angle X-ray scattering (GIWAXS) and angle-resolved UV-vis. Finally, the PSC based on 2D/3D $MAPbBr_3$ are fabricated and the degradation behavior of this PSC under moisture and illumination conditions are monitored by GIWAXS.

Overall, some of the questions are addressed in this thesis:

- How to obtained the controllable pore size via spray coating?
- What’s the mechanism of a film formation during spray-coating? And what’s the evolution of the structure features during spray-coating?
- How to structure a titania film, which is prepared from a titania nanoparticle paste? How to achieve a structured sol-gel prepared titania film with a desired structure depth?
- How do the plasmonic core-shell particles enhance the performance of PSCs? Is it due to the plasmonic enhancement mechanism or the perovskite crystal?

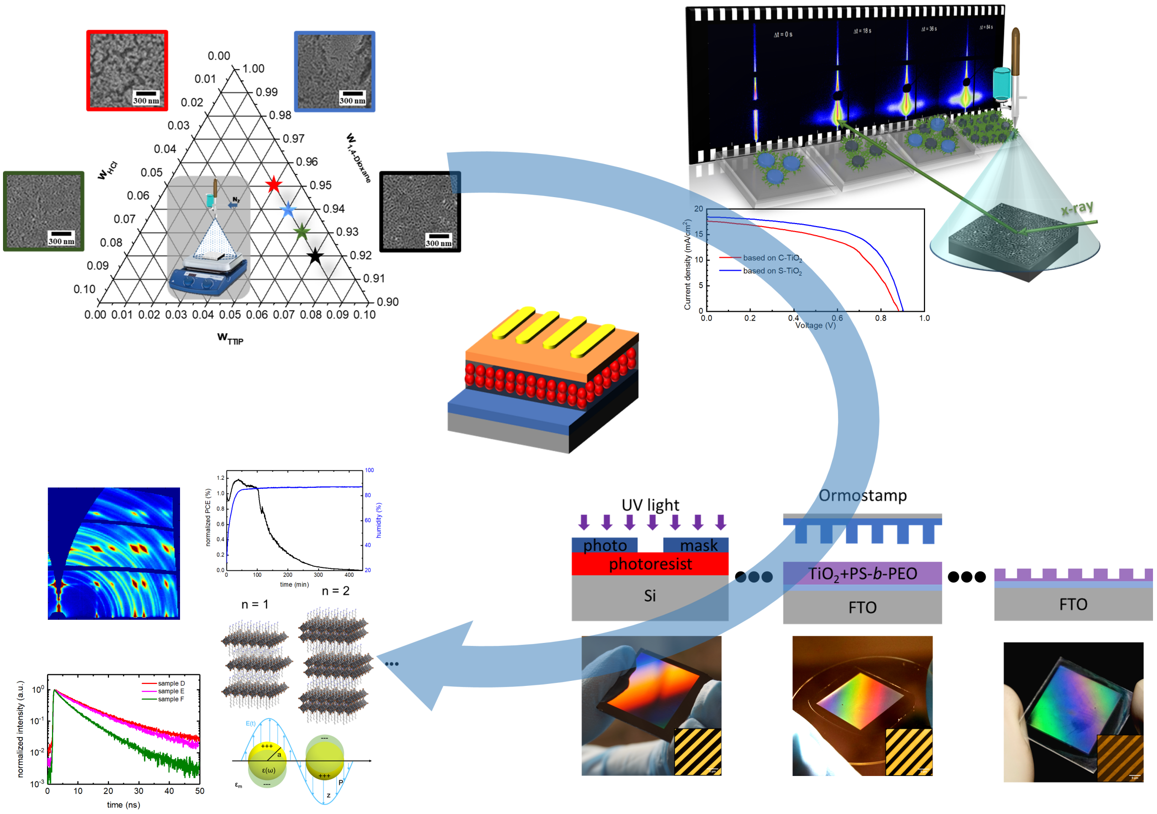

Figure 1.1 *Schematic overview of four research topics, on which these present thesis mainly focuses. These topics are: a) pore size control of block copolymer-templated sol–gel-synthesized titania films deposited via spray coating;*[38] *b) macroscale and nanoscale morphology evolution during in situ spray coating of titania films for perovskite solar cells;*[39] *c) structuring mesoporous titania films via photolithography approaches; d) influences of customized titania films on optoelectronic properties of quasi-2D perovskite films.*

2. THEORETICAL ASPECTS

This chapter aims to give a theoretical background of the materials, processes and working principles referred to this study. An introduction to nanostructured titania films is discussed in section 2.1, with a special emphasis on titania properties, diblock copolymers, and the principles of sol-gel wet chemistry. The diblock copolymer is used as a structure-directing template of the titania films. With this method, the versatile morphology of the titania films can be obtained. The fundamental principles of solar cells are introduced in section 2.2, in which we mainly focus on dye-sensitized solar cells and perovskite solar cells. The working principles of localized surface plasmons are presented in section 2.3. Lastly, the theoretical aspects of X-ray scattering are introduced in section 2.4; this section provides theoretical details on grazing incidence X-ray scattering techniques, especially for analysis of samples with a periodic line grating structure.

2.1 Nanostructured titania films

There are vast applications using titania material, for example, titania films as an electron conductive layer in photovoltaics,[40-42], as absorbing layer in photocatalysis, [43, 44] and as a sensing material in gas sensors.[45, 46] In this section, the properties of titania material are firstly introduced, followed by the basic principles of sol-gel chemistry. At the end, the photolithography approach is presented.

2.1.1 Titania properties

Titania is chemically stable and a cheap, environmental-friendly material. The band gaps for the different crystal classes: rutile, anatase and brookite phase are 3.0 eV, 3.2 eV and 3.1-3.4 eV, respectively. Therefore, titania material shows photoactivity in UV light. The crystal structures are represented in Figure 2.1. In all polymorphs, the slightly distorted TiO_6 octahedra is formed and connected by sharing the edges of octahedra. Rutile phase has a tetragonal structure with a space group of $P4_2/mnm$, and shows a thermodynamically stable form in bulk titania at most temperatures and pressures up to 60 kbar.[47] However, anatase and brookite shows less thermal stable in the bulk titania, and the phase transformation from brookite or anatase to rutile are more preferable when the temperature above 570 °C. It is attributed to the smaller surface energy of anatase and brookite phases compared to that of rutile.[48] Anatase has a tetragonal crystal structure with a space group of $I4_1$/amd, while brookite has an orthorhombic crystal structure with a space group of Pbca. Brookite is the least stable phase, and the phase transformation occurs by thermal treatment from brookite to anatase and then to rutile phase.[49] Furthermore, pure brookite rarely exists in nature. Therefore, it is not further discussed.

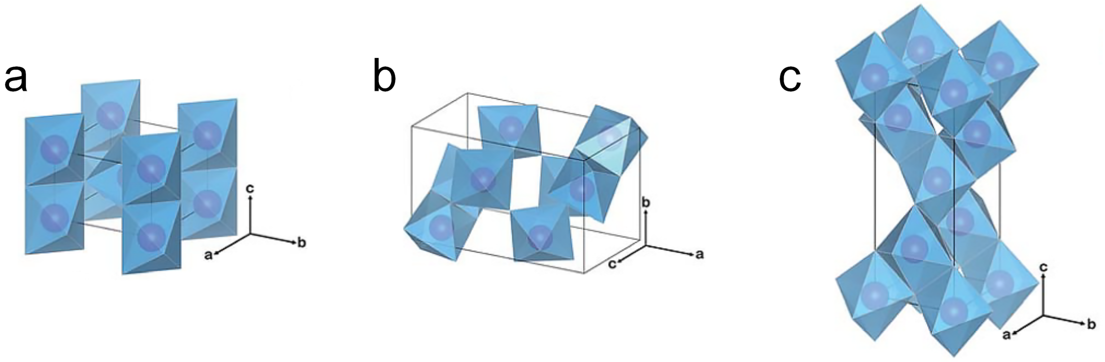

Figure 2.1 *Crystal structures of titania: a) rutile; b) brookite; c) anatase phase. The Ti atoms are represented as purple spheres, while the TiO_6 blocks are represented as blue octahedra. For better clarity, O atoms at the corner of the octahedra are omitted. (This figure is adapted from reference.[50])*

Anatase exhibits an indirect band gap, while rutile exhibits either a direct or an indirect bandgap, but still very similar to a direct band gap.[51] The result is that the carrier lifetime in anatase phase is longer than the one in rutile phase. The longer lifetime would make the carriers more likely to participate in surface reactions. The anatase phase is preferred for the photovoltaics, due to its potentially lower conduction band energy level, higher electron mobility, lower dielectric constant and longer carrier lifetime.[52] The higher photoactivity in anatase phase is attributed to a slightly higher Fermi level and a higher degree of hydroxylation.[53] When the titania films are exposed to UV light, the electron in the valence band with 2*p* and 3*d* orbitals are excited in to the conduction band, which only has 3*d* orbitals. Because of the dissimilar parity, the excited electron can only decay to 2*p* orbital in the valence band. Therefore, the probability of electron-hole recombination is reduced. Energy band bending occurs on the interface between two different materials. The band bending of anatase exhibits a deeper region with a steeper slope in regards to rutile.[54] Thus, the charge separation is more efficient in anatase phase. Additionally, the physical and chemical properties of titania films are also affected by size, shape and surface properties. For example, in the architecture of photovoltaics, the foam-like structure of titania layer, which has a large value of surface-to-volume ratio, is used to enhance the reaction efficiency at the interface between the titania and absorber layer. In order to minimize the defects in crystal structure and grain boundaries, the ordered titania single-crystal-like nanowire is introduced as the ideal structure for photovoltaics. It is expected to enhance the charge mobility thus allowing more efficiency in charge collection. However, it is still challenging to deposit well orientated nanowire. Surface modification of titania films, which affect the carrier separation, and transport processes, is also investigated for photovoltaics.[55]

2.1.2 Polymer basics

Based on the description of polymers by the IUPAC (International Union of Pure and Applied Chemistry),[56] molecules are generally classified according to their molecular mass (M_w) as: micro-molecules (M_w < 10^3 g/mol), oligomers ($10^3 \leq M_w \leq 10^4$ g/mol), and polymer macromolecules (M_w > 10^4 g/mol). Polymers are a type of string-like molecules, which are formed from a single or more types of repeat unit. One of the repeat units is called monomer, which is connected sequentially with a covalent bond as shown in Figure 2.2. In case the monomer (A) is a single type, this polymer is a so-called homopolymer (A-A-…-A-A). In case the monomers include two types (A-B), this polymer is a so-called diblock copolymer (A-B-A-B-…-A-B-A-B). From a synthesis process, the monomer molecules form a long polymer chain by chemical reaction. This process is called polymerization. For example, polystyrene has the molecular formula of $(C_8H_8)_m$. The degree of polymerization is represented as *m*, which describes the number of monomers in one polymer chain (Figure 2.2c).

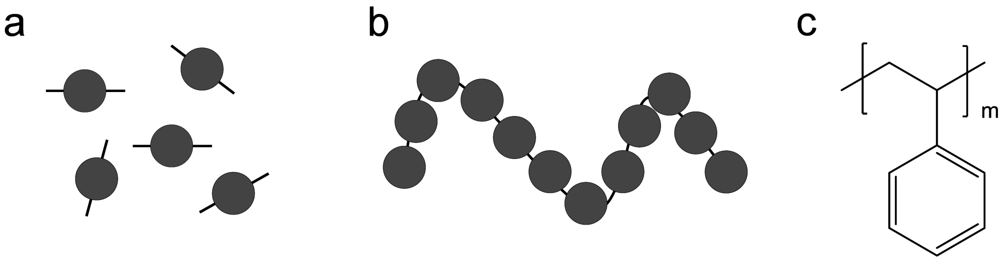

Figure 2.2 *Skeletal polymer representation: (a) monomer, (b) linear polymer, a curved line with spheres representing the monomers or segments of the polymer chain, (c) abbreviated as the skeletal formula of PS with a degree of polymerization m.*

The polymers are made by syntheses that yield not a single degree of polymerization, but a distribution, such as weight average and number average. The width of the molecular weight distribution is called polydispersity index (PDI), which can be defined as M_w/M_n (Mn represents the number average molecular weight). For example, polymer with lower PDI means the polymer has a narrow molecular weight distribution. The temperature-dependent Flory-Huggins interaction parameter χ describes the interaction between two homopolymers and is shown as

$$c = c_s + \frac{c_H}{k_B T} \tag{2.1}$$

where k_B and T are the Boltzmann constant and the temperature, respectively, while c_S and c_H are the entropic and the enthalpic terms, respectively. The end groups and the conformation of the chains mainly contribute to the entropic part.

The phase behavior of diblock copolymers is dictated by the chain length (the degree of polymerization N), polymer segment chemical character (quantified by the Flory-Huggins interaction parameter χ), and the composition (monomer volume fraction of each block f). In a diblock copolymer, two chemically distinct lengths of polymer segment are linked together via covalent bond. When the interactions of two segments are energetically unfavorable, phase separation occurs in order to minimize the surface tension. Due to the covalent bonds, which links two segments, the phase separation is restricted on the nanoscale.[57, 58] In a case of $f = 1/2$, when $cN = 10$ or $cN < 10$, the entropic factor mainly dominants and disordered structure is presented in the bulk. The transition from disorder to order starts at cN » 10.495. With further increase of χN, the increasing entropy plays a main role in this process. Therefore, sharper microdomain boundaries are formed to reduce the interface area of segment A and B.[59, 60] In the case where f ¹ $1/2$, the microphase separated structures are affected by f. In theory, a highly symmetrical phase diagram can be achieved by varying f from 0 to 1. A vast number of possible morphologies (such as a sphere, hexagonal cylinder, bicontinuous gyroid network, and lamellar structures) can be designed by varying f. Diblock copolymers show great potential in three different approaches: as an active material;[61-64] as a direct structure template;[38, 39, 65, 66] and as a combination of active material and structure director[67, 68].

The glass transition temperature (T_g) is defined as the temperature region where an amorphous polymer shows a transition from a hard, glassy state to soft, rubbery state. The glass transition temperature shows a kinetic character. For example, the glass transition temperature of polystyrene (PS) is 105 °C at a cooling rate of 1 °C/min, while it is 95 °C at a cooling rate of 0.01 °C/min.

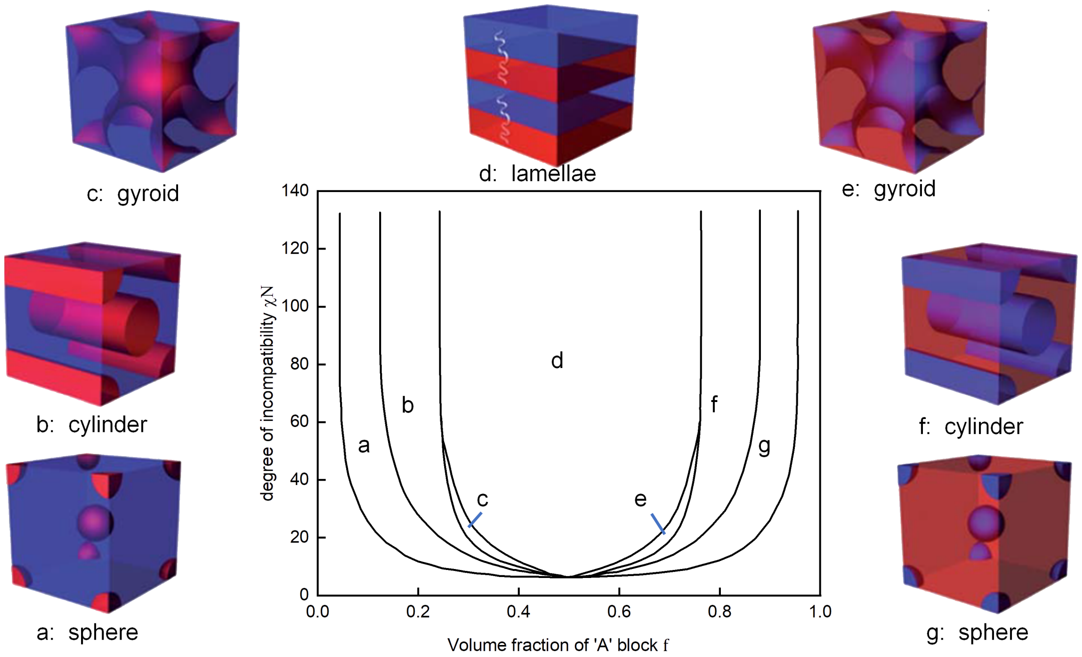

Figure 2.3 *Theoretical prediction of diblock copolymer of PA-b-PB. Segment A is represented in red color, while segment B is represented in blue color.*

2.1.3 Basic principles of sol-gel chemistry

Sol-gel chemistry is firstly introduced for the preparation of alkoxide in 1846,[69] and it is now widely used in the fabrication of ceramics, metal oxide films, and inorganic polymers from solution based reactions. After the sequential reactions, the liquid precursors transform into a colloidal solution (sol), from which a network structure (gel) is formed. In general, the sol-gel process can be described in 5 steps: (1) synthesize the colloidal solution by hydrolysis and condensation of alkoxide; (2) form the gel through polycondensation, and the metal-O covalent bond is formed; (3) expulse the solvent within the gel network; (4) dry the gel to form dense 'xerogel' or aerogel; (5) calcinate the powder or films to remove the metal-OH groups.

In this thesis, TTIP is used as a titania precursor. The hydrolysis (equation 2.2), water condensation (equation 2.3) and alcohol condensation (equation 2.4) are shown by the following equations:

$$(RO)_3Ti\text{ - }OR + H_2O \rightleftharpoons (RO)_3Ti\text{ - }OH + ROH \tag{2.2}$$

$$(RO)_3Ti\text{ - }OH + HO\text{ - }Ti(OR)_3 \rightleftharpoons (RO)_3Ti\text{ - }O\text{ - }Ti(OR)_3 + H_2O \tag{2.3}$$

$$(RO)_3Ti\text{ - }OH + RO\text{ - }Ti(OR)_3 \rightleftharpoons (RO)_3Ti\text{ - }O\text{ - }Ti(OR)_3 + ROH \tag{2.4}$$

In an aqueous solution, water molecules transfer electrons to the unoccupied d-orbitals on Ti^{4+}. However, solution's pH of the influences the degrees of hydrolysis:

$$[Ti(OH_2)]^{4+} \longrightarrow [Ti-OH]^{3+} + H^+ \longrightarrow [Ti=O]^{2+} + 2H^+ \tag{2.5}$$

Therefore, the hydroxo ligands are favorable for formation in acidic conditions, whereas oxo ligands are preferred for formation. In order to form long species instead of agglomerates of $(RO)_3Ti$-O-$Ti(OR)_3$, HCl is added to create an acidic condition. Besides that, the PS-*b*-PEO is used as a structure-guide, and amorphous titania particles selectively interact with the PEO domain with hydrogen bonding without any surfactant addition.[70] Furthermore, the Ti-O bonds are linked with adjacent titania species to form the continuous structure. The final sol-gel solution consists of TTIP, PS-*b*-PEO, 1,4-dioxane and HCl. The 1,4-dioxane acts as a good solvent for both blocks, whereas HCl is a selective solvent. After adding a small amount of HCl, micelles are formed to minimize the interfacial energy. The complex nanostructures can be achieved by varying the weight ratio of each composition. During the preparation of the sol-gel solution, the atmospheric humidity is crucial and needs to be controlled, since the water influences not only the hydrolysis of TTIP but also acts as a selective solvent in the micelles formation process.

The sol-gel solution can be used in serval deposition methods, such as spin-coating, spray-coating, solution-casting and printing. High temperature calcination is carried out in the final step to remove the polymer matrix and crystallize the titania films.

2.2 Principles of solar cells

2.2.1 Dye-sensitized solar cells

Dye-sensitized solar cells (DSSCs) are photoelectrochemical cells, in which the conversion of solar photons into electrical energy occurs. The two electrodes, based on fluorine-doped tin oxide (FTO) as a substrate, are facing each other with an electrolyte solution injected in-between. Mesoporous anatase titania film, where a monolayer of sensitizing dye is loaded, is used as a photoanode. Due to a large surface-to-volume value, mesoporous titania film with an average size of around 20 nm is the best candidate as a photoanode. After calcination, the anatase films normally is transparent. Before deposition of the mesoporous titania layer, it is crucial to deposit an ultrathin compact titania layer on top of the FTO substrate, thus separating the connection between FTO and liquid electrolyte. This prevents the recombination of the photogenerated electrons in FTO layer with the oxidizing species in the liquid electrolyte. The electrolyte consists of acetonitrile and a redox couple of I^-/I_3^-. A Pt film is used as an electrocatalyst on the counter electrode. A schematic of the dye-sensitized solar cells' architecture is shown in Figure 2.4a.

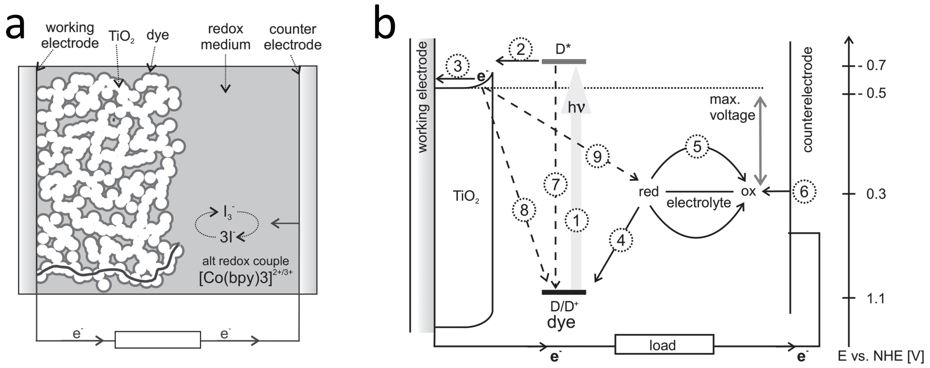

Figure 2.4 *a) Schematic of dye-sensitized solar cells architecture. A monolayer of sensitizing dye molecules is chemisorbed on the surface of titania films and surrounded by a liquid electrolyte. The FTO glass with a thin Pt film acts as a counter electrode. b) A demonstration of fundamental processes in conventional dye-sensitized solar cells. The energy level with respect to a normal hydrogen electrode (NHE) are shown on the right side. This figure is adapted from reference.*[15]

The fundamental processes in a conventional DSSC can be summarized as follows (Figure 2.4b):

(1) Photoexcitation of dye.[71] The electrons in the dye molecules are excited into the lowest unoccupied molecular orbital (LUMO) by the absorption of sunlight;

(2) Excited electron injection into the titania film.[72] An excited electron is rapidly transferred into the conduction band of titania film, and positively charged dye species are left in the electrolyte, since the conduction band of titania has a higher density of states. This process occurs on a time scale of 0.05 to 150 ps;

(3) Excited electron transportation into the FTO working electrode.[73] The electron is randomly diffused in the titania skeleton, then injected into the FTO working electrode in a time scale of 1 ps;

(4) Regeneration of the oxidized dye molecule via iodide radical.[74] The remaining positively charged dye is regenerated by receiving electrons from the iodide radical (I^- to I_3^-) in the electrolyte in a time scale of 0.5 µs, and the reactions are given by reaction 2.6 – 2.8;

$$D^+ + I^- \longrightarrow (D\cdots I) \tag{2.6}$$

$$(D\cdots I) + I^- \longrightarrow D + I_2^{-\cdot} \tag{2.7}$$

$$I_2^{-\cdot} \longrightarrow I_3^- + I^- \tag{2.8}$$

(5) Hole transportation into the counter electrode.[75] The hole is transferred by the diffusion of the iodide radical in the electrolyte towards the counter electrode;

(6) Reduction of the oxidized donor.[76] At the counter electrode, I_3^- is efficiently reduced to I^-, as shown in reaction 2.9;

$$I_3^- + 2e^- \longrightarrow 3I^- \tag{2.9}$$

(7) The decay of excited dye. It is also possible for the excited dye to go back to the ground state by radiative and nonradiative decay;

(8) Regeneration of the oxidized dye molecule via back-transfer of titania injected electron. After injection of an electron into titania, an electron can recombine with a positively charged dye molecule. Haque *et al.* reported that this recombination rate can be dramatically accelerated at a high light intensity, which causes the loss of PCE;[77]

(9) Recombination of an injected electron with the iodide redox medium.[78] During the transportation of the injected electron in titania, the recombination of an electron with electron acceptor in the electrolyte can occur at the interface of titania and electrolyte, since the titania film is infiltrated with electrolyte.

The recombination reactions, such as processes 7 to 9, mainly cause the loss of PCE in DSSCs.

2.2.2 Perovskite solar cells

Perovskite solar cells (PSCs) are based on organometal halide perovskite material as an absorber, such as $CH_3NH_3PbI_3$, $CH_3NH_3PbBr_3$, $CH_3NH_3PbI_{3-x}Cl_x$. Organic halide perovskites have ABX_3 crystal structures as shown in Figure 2.5a, where A, B, and X represent organic cation, metal cation, and halide anion, respectively. The crystallographic stability and structure are determined by tolerance factor t and octahedral factor μ. Goldschmidt firstly defined the tolerance factor as:[79]

$$t = \frac{R_A + R_X}{\sqrt{2}(R_B + R_X)} \tag{2.10}$$

where R_A, R_B and R_X represent the ionic radii of A, B, and X, respectively. For example, $0.89 < t < 1$ for cubic crystal symmetry, and $t > 1$ for hexagonal structure. The size mismatch of A, B and X results in the compression of the B-X bond, then the tilted octahedra presents in the crystal structure. Octahedral factor μ is defined as a ratio of radii of metal cation B to halide anion X ($\mu = R_B / R_X$) by Li *et al.*.[80] According to the octahedral factor, the stable perovskite structure only forms when $\mu > 0.442$.

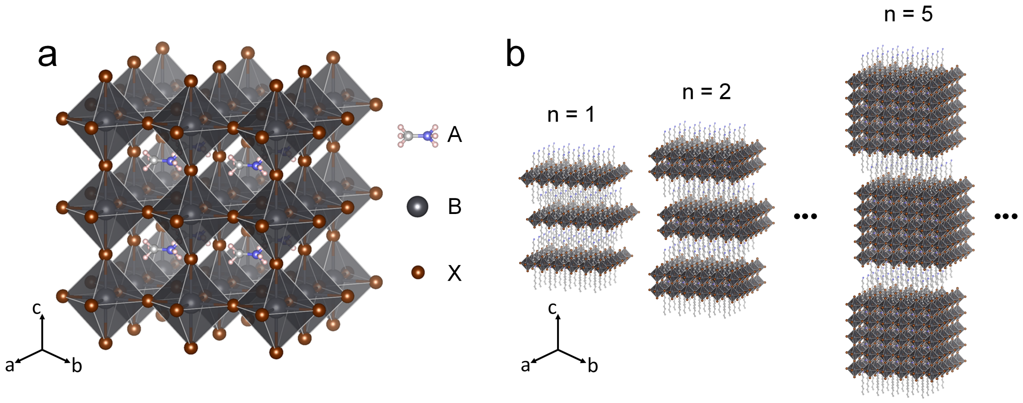

***Figure 2.5** a) Crystal structure of perovskite. A represents an organic cation, B represents a metallic cation and X represents a halide. b) 2D perovskite crystal with n lead bromide layers (n = 1, 2, 5). The long chain, which separates the layered perovskite crystal, represents octylamine ($C_8H_{17}NH_2$, OA).*

The 2D Ruddlesden-Popper perovskite can be formulated as $(RNH_3)_2A_{n-1}B_nX_{3n+1}$ (pure 2D structure when $n = 1$, quasi-2D structure when n = defined integer, 3D structure when $n = \infty$), where RNH_3 represents a long organic ammonium cation, such as $C_8H_{17}NH_2$, A represents a short organic cation, B represents a metal cation, X represents a halide anion, and n represents the number of inorganic metal halide layers. The different number of BX_6 octahedra layers are isolated and surrounded by the longer organic chains in c direction, which hold BX_6 layers together by weak van der Waals forces. This layered structure can be considered as a quantum-well structure (as shown in Figure 2.5b), in which the inorganic sheets and the longer organic chains act as “well” and “barrier”, respectively. Upon dimensional reduction, the electron-hole pairs are confined to a plane, thus the interaction of the electron and hole is enhanced. As a result of quantum confinement, the energy levels become discrete and blue-shifted.[81, 82] Therefore, a layered perovskite shows the tunable optoelectronic properties (such as the band gap,[83] exciton binding energy,[84] second-harmonic generation and stability[85]) and enhancement of quantum yield[86]. Despite a larger band gap in 2D perovskite, 2D perovskite importantly shows superior environmental stability and water resistance,[87-89] which makes it suitable for photovoltaic applications.

There are two dominate configurations of perovskite solar cells, mesostructured PSCs and planar PSCs. Mesostructured PSCs consists of scaffold titania films and sensitized absorber of organometal halide perovskite material. The working mechanism is similar to solid-state DSSCs, in which the photoexcited excitons are generated in the absorbing material, followed by the injection of electrons into the titania film, while holes are collected by hole transfer layer. However, perovskite exhibits a low binding energy of the photo-excited states and a long diffusion length (L_D > 1 µm for $CH_3NH_3PbI_{3-x}Cl_x$ and ~ 100 nm for $CH_3NH_3PbI_3$), which allows the effective and direct transportation of the photogenerated electrons and holes to the electrodes in an ultrafast injection.[90, 91] Planar PSCs consists of all planar layers, in which only compact titania films are used as a hole blocking layer and mesoporous titania is omitted. In the recent reports, the mesoporous titania scaffold can retard the charge recombination and elongate the optical light path.[14, 92] Furthermore, the well-defined crystallinity, the feature size of perovskite, and the charge mobility also benefit from the ordered mesoporous structures.[8, 12, 90, 93-95] Figure 2.6 shows the architecture of mesostructured PSC (the scaffold titania layer is omitted for the planar PSC) and vacuum energy levels of PSC.

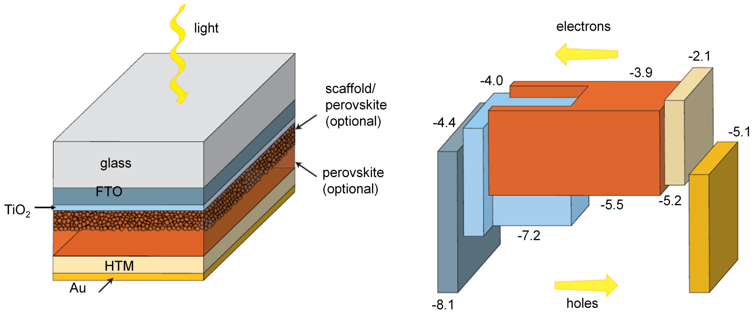

Figure 2.6 *Architecture of a mesostructured PSC and a diagram of vacuum energy levels for associated layers. The structure without scaffold titania layer corresponds to a planar PSC. HTM in this figure represents spiro-MeOTAD. This figure is adapted from reference.*[96]

In the configuration of mesostructured PSC, charge mobility in perovskites is less important, compared to the interfacial properties of perovskite. Figure 2.7 shows the fundamental processes in PSC, which are described as following: (1) photoexcitation in perovskite layer under light; (2) injection of excited electron to titania; (3) injection of hole to the HTM; (4) recombination of photogenerated species; (5) recombination of injected electrons on the interfaces of titania layer with holes in perovskite layer; (6) back charge transfer from HTM to the perovskite; (7) recombination of electrons in titania with holes in HTM. The last process only occurs in the area without perovskite capping layer.

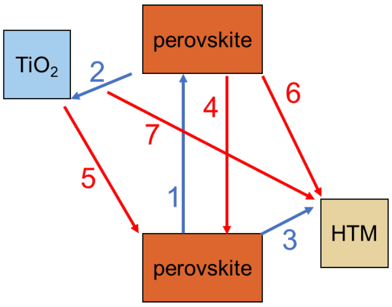

Figure 2.7 *A demonstration of fundamental processes in PSCs. The arrows with blue and red colors represent the desirable processes for solar conversion and processes associated with losses of PCE, respectively.*

2.3 Localized surface plasmon resonances

Localized surface plasmons (LSPs) are non-propagating excitations, which are generated by the coupling of metallic nanostructures to the electromagnetic field. When a metal nanoparticle with a sub-wavelength size is placed in an oscillating electromagnetic field, a resonance of noble metal nanoparticle is generated by a restoring force on the driven electron. This resonance is named as localized surface plasmon resonance (LSPR). In the case of curved metallic nanostructures, LSPR also can be excited by exposure of a noble metal nanoparticle to light. It leads to an enhancement of electric fields both inside and surrounding the nanoparticle. In the quasi-static approximation ($\lambda \gg 2a$), the maximum optical abortion occurs at the plasmon resonant frequency. As shown in Figure 2.8, the homogeneous metal particle with a sphere shape is placed in an electric field under the conditions of quasi-static approximation. The induced dipole moment in the metal particles is generated by the electrostatic field, and polarizability α in a function of incident light with wavelength λ, can be written as

$$\alpha(\lambda) = 4\pi\varepsilon_0 a^3 \left| \frac{\varepsilon(\lambda) - \varepsilon_m(\lambda)}{\varepsilon(\lambda) + 2\varepsilon_m(\lambda)} \right| \tag{2.11}$$

where ε_0, ε and ε_m are the vacuum permittivity, the dielectric constant of the metal particle and the host medium, respectively, and a represents the radius of the spherical metal particle. From Mie theory,[97, 98] the optical cross section of absorption (σ_{abs}), scattering(σ_{sca}) and extinction(σ_{ext}) are

$$\sigma_{sca} = \frac{k^4}{6\pi\varepsilon_0^2} \left| \alpha(\lambda) \right|^2 \tag{2.12}$$

$$\sigma_{abs} = \frac{k}{\varepsilon_0} \operatorname{Im}\left[\alpha(\lambda) \right] \tag{2.13}$$

$$\sigma_{ext} = \sigma_{sca} + \sigma_{abs} \tag{2.14}$$

where k represents the wavenumber of light. For a small metal nanoparticle, the absorption mainly dominates the extinction optical cross section; in contrast for a large one, the scattering mainly dominates. The enhancement of electric field of both the inside and outside of the metal nanoparticles are given by

$$\vec{E}_{in} = \frac{3\varepsilon_m}{\varepsilon + 2\varepsilon_m} \vec{E}_0 \tag{2.15}$$

$$\vec{E}_{out} = \vec{E}_0 + \frac{\varepsilon - \varepsilon_m}{\varepsilon + 2\varepsilon_m}\frac{a^3}{r^3}E_0(2\cos\theta\cdot\vec{r} + \sin\theta\cdot\vec{\theta}) \qquad (2.16)$$

where E_0 is the magnitude of the external electric field, and θ represents the angle between position vector r and the z-axis (as shown in Figure 2.8). The maximum of E_{out} occurs in a condition when $(\varepsilon+2\varepsilon_m)$ is at a minimum, which is known as the Fröhlich condition,

$$\mathrm{Re}(\varepsilon(\omega)) = -2\varepsilon_m \qquad (2.17)$$

where R_e is the real part of dielectric function and ω is the resonance frequency.

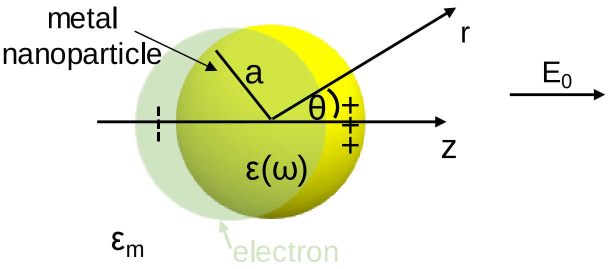

***Figure 2.8** Sketch of a homogeneous metal nanoparticle in an electrostatic field.*

The plasmonic enhancement in the photovoltaics can be defined as radiative effects and nonradiative effects. The former one includes far-field scattering and electromagnetic near-field enhancement, while the latter one includes hot-electron transfer and plasmon resonant energy transfer (as shown in Figure 2.9).

When the light impinges on metal nanoparticles with a high albedo, the light redirects and scatters into the far-field (in a magnitude of hundreds of nanometers). The scattered light can be reabsorbed by the active layer, such as dye and perovskite layer, which increases the light trapping in the solar devices. The suitable particle size for far-field scattering is a > 30 nm, while the absorption is dominated in the condition a < 30 nm. Beyond the size effect, the dielectric constant of the surrounding medium also affects the far-field scattering. For example, a core-shell structure of gold-titania nanoparticles (Au@TiO_2 NPs) is widely used in photovoltaics, due to a high dielectric constant of titania (~ 6.8). A higher dielectric constant leads to a redshift, which enables the absorption of the light beyond the absorption of dyes and perovskites.

As equations 2.15 and 2.16 indicate, the electromagnetic fields are enhanced by the metal nanoparticles in orders of magnitude higher than the light source. Thus, the metal nanoparticles act as a secondary light source, which increases the photon flux. An increase of electron-hole dissociations rate is attributed to the enhancement of localized electric field. This near-field plasmonic plays a role when the noble metal particle has a size of > 45 nm.

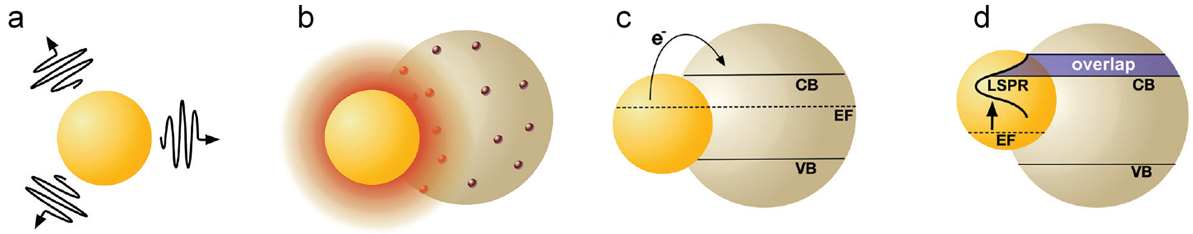

Figure 2.9 *Illustration of LSPR enhancement mechanisms: a) far-field scattering; b) electromagnetic near-field enhancement; c) hot-electron transfer; d) plasmon resonant energy transfer. (adapted from reference*[99]*)*

The hot electron-hole pairs are generated via nonradiative decays (known as Landau damping). In the condition that noble metal golds particles are attached to the titania film. The hot electrons firstly diffuse towards the interface of metal and titania. Since titania exhibits a high density of states in the conduction band, it allows fast electron injection. The hot electrons overcome the Schottky barrier and then transfer into titania films. The unwanted recombination is reduced by the hot electron transfer.

In non-radiative effects, plasmon resonant energy transfer also contributes to the plasmon enhancement. After light absorption by the noble metal nanoparticles, the resonant energy in the metal nanoparticles can be transferred into the adjacent semiconductor through a dipole-dipole coupling process. In the case of Au@TiO_2 NPs, the hot electron transfer plays a role in the plasmon enhancement, due to the direct contact between titania layer and gold nanoparticles. However, when a thick insulator layer is present in-between the semiconductor layer and gold nanoparticles, the hot electron transfer is forbidden and only the plasmon resonant energy transfer dominates the plasmon enhancement.

2.4 Grazing incidence X-ray scattering

Grazing incidence X-ray scattering techniques provide a non-destructive method to probe the morphology of the samples on a sub-nanometer to micrometer scale. The geometry of grazing incidence X-ray scattering is show in Figure 2.11. X-ray (wave vector $\boldsymbol{k}_i$) with wavelength λ impinges on the sample along the x-axis in a shallow angle of $\alpha_i < 1°$ (with respect to the sample surface), then the diffuse scattering signal (wave vector $\boldsymbol{k}_f$) with an angle of ψ_f is recorded by a detector on (y, z)-plane. This shallow incident angle leads to the formation of a large footprint on the sample surface with an area of around 3000 × 30 μm^2. Since the X-ray can penetrate film in a depth on a micrometer scale when the incident angle is larger than the critical angle of material, an average volume structure feature of the inner films can be analyzed based on the first order perturbation theory, which is named distorted wave Born approximation (DWBA).[100] In DWBA theory, the sample is considered as a homogenous flat film, and the roughness and lateral structure information are added as a first-order perturbation. The scattering pattern is recorded in the reciprocal space, and the scattering vector ***q*** is given by

$$\vec{q} = \vec{k}_f - \vec{k}_i = \frac{2\pi}{\lambda}\begin{pmatrix} \cos(\alpha_f)\cos(\psi_f) - \cos(\alpha_i)\cos(\psi_i) \\ \cos(\alpha_f)\sin(\psi_f) - \cos(\alpha_i)\sin(\psi_i) \\ \sin(\alpha_f) + \sin(\alpha_i) \end{pmatrix} \tag{2.18}$$

where α_i represents a scattering angle in (*x, z*)-plane, and ψ_i, $\psi_f = \psi$ are scattering angles in (*x, y*)-plane. Typically, ψ_i is set to 0. When the sample-to-detector distance (SDD) is large enough (> 1 m), it allows a small scattering angle, therefore the component q_x can be neglected.[101] In the framework of the effective interface approximation of DWBA, the cross section of diffuse scattering can be expressed by

$$\left.\frac{d\sigma}{d\Omega}\right|_{diff} = \frac{C\pi^2}{\lambda^4}(1-n^2)^2 \left|T_i^F\right|^2 \left|T_f^F\right|^2 P_{diff}(\vec{q}) \propto P_{diff}(\vec{q}) \tag{2.19}$$

where *dΩ* is the solid angle, *C* is the probed area, $T_{i,f}^F$ and $P_{diff}(\vec{q})$ represent Fresnel transmission coefficients and the diffuse scattering factor, respectively. It is clear that the maximum of scattering intensity occurs when $T_{i,f}^F$ also obtain their maximum, which fulfills the condition of $\alpha_i = \alpha_f = \alpha_c$. This strong characteristic scattering signal is known as Yoneda peak, which is correlated to the scattering length density and mass density.[102] In the case of Bragg peaks along the *z*-axis, it indicates the structure is parallelly aligned to the sample surface. Whereas, a perpendicularly aligned structure shows prominent Bragg peaks along the y-axis.

By reducing SDD, the wide-angle scattering can be achieved. In a wide-angle range, the curved surface of the Ewald sphere with respect to the flat crystal plane cannot be neglected and the χ angle rang of 0 to θ_B is not accessible (as shown in Figure 2.10), which results in a certain distortion in the recorded scattering pattern. It results in both q_y and q_z containing a contribution from component q_x. To display a corrected scattering pattern, χ-correction is needed.[103] After this correction, the scattering pattern is shown in a q_r vs. q_z map with a black missing wedge. Here, q_r is defined as

$$q_r = \sqrt{q_x^2 + q_y^2} \tag{2.20}$$

Besides χ-correction, additional corrections are also needed to obtain a reliable intensity distribution, such as efficiency corrections, solid angle correction and polarization correction.[104] After analysis of the scattering pattern, the crystallinity and crystal orientation can be determined. For example, for polycrystalline titania films, the Debye-Scherrer rings are shown on the scattering pattern, while prominent Bragg's spots are observed and correspond to a certain crystal with a preferential orientation.

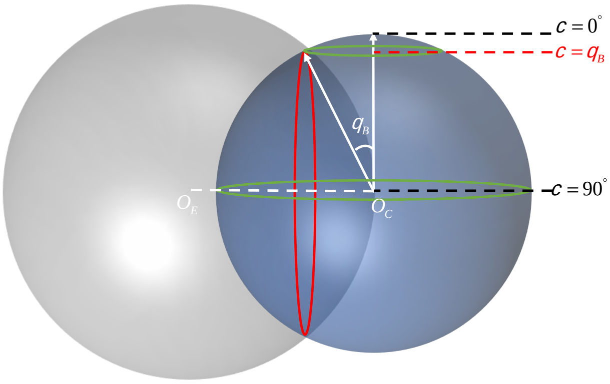

Figure 2.10 *Schematic representation of the distortion, which arises from the intersection of the Ewald sphere and the crystal orientation spheres for* θ_B *, in the 2D scattering pattern.*

For the films with a periodic structure, the grating truncation rod (GTR) is shown in the scattering pattern.[105-108] In the X-ray elastic scattering, all the observed scattering signals come from the Ewald sphere. The direct reflected beam position (specular beam position) with vector ***q*** can be observed when $\alpha_i = \alpha_f$. In this case, all the scattering signals with ***q*** arise from the doted circle as shown in Figure 2.11. The equation of Ewald sphere in reciprocal space can be written as

$$\left(q_x + \frac{2\pi}{\lambda}\right)^2 + q_y^2 + q_z^2 = \left(\frac{2\pi}{\lambda}\right)^2 \tag{2.21}$$

Since the grating on the sample has a periodicity *P*, the adjacent distance of GTRs in reciprocal space can be calculated by[109, 110]

$$\Delta q_y = \frac{2\pi}{P} \tag{2.22}$$

Several maximum intensity positions can be observed on the scattering pattern, and located along the specular beam position in direction q_y. They originate from the intersection of GTR with all positions ***q*** on the Ewald sphere as shown by the larger black dots in Figure 2.11. In this thesis, the grating structure is in the micrometer range, therefore the adjacent distances of GTRs are too small to be observed individually, and only a continuous line is detected.

When the line grating structure is aligned along the q_y-direction, GTRs present at the position of q_y=0. Whereas, in the case it is aligned along the q_x-direction, maximum points are recorded in the q_z direction.[106, 108, 111]

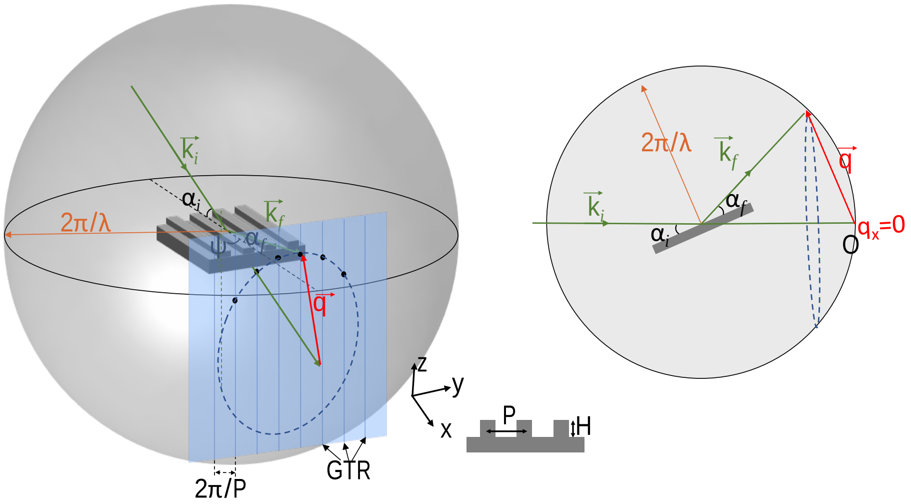

Figure 2.11 *Schematic representation of grazing incidence X-ray scattering geometry (on the right). The simplified 2D sketch is shown on the left. The periodicity of the grating sample is represented by P, while the structure height of the grating sample is represented by H. The maximum scattering intensities (larger black dots) arise at the intersections of the grating truncation rods (GTRs) with the dotted-circle.*

3. CHARACTERIZATION METHODS

In this chapter, different techniques, used in this thesis, are presented. The structural characterization method, regarding real-spacing and reciprocal-space imaging techniques, is firstly introduced in section 3.1. The spectroscopic and electronic characterization techniques are described in section 3.2. The working principle and applied parameters of each instrument are also described.

In detail, the real-space techniques include scanning electron microscopy (section 3.1.1), transmission electron microscopy (section 3.1.2), and atomic force microscopy (section 3.1.3). Additionally, reciprocal-space imaging techniques, including X-ray diffraction (section 3.1.4), and grazing incidence X-ray scattering (section 3.1.5), are also described. Furthermore, the optical and electronic properties are characterized by UV-vis spectroscopy (section 3.2.1), photoluminescence spectroscopy (section 3.2.2), and J-V characterization (section 3.2.3).

3.1 Structural characterization

3.1.1 Scanning electron microscopy

Scanning electron microscopy (SEM) is a real-space imaging technique. High resolution in a range of 1 – 10 nm can be achieved via SEM, due to the shorter wavelength of the electron compared to the one of photons. It is the ideal method for characterization of the morphology of top-surface and cross-sectional semiconductor films. In this thesis, all the SEM images are obtained from an FESEM Gemini NVision 40, which is provided by Carl Zeiss and controlled by the software SmartSEM.

The well-focused electron beam is generated by a strong electrostatic field in a range of 0 – 30 KeV under a condition of high vacuum (2×10^{-9} mbar), then it is accelerated by an external voltage before interaction with the sample surface. After scanning the sample by the incident electron beam, the electrons emitted from the surface are collected by the detectors. Here, the “InLens” detector is used to collect the secondary electrons. A low working distance in the range of 1 to 5 mm is chosen. For the hybrid titania samples, a conducting carbon tape is connected from the top surface of the sample to the sample holder to enhance the clarity of SEM images. For the cross-sectional SEM measurement, the sample stage is tilted to 60° with respect to the horizon, while a tilt correction of 30° (90°- 60°= 30°) is applied to obtain the real structure size of the films. In general, the sample for the cross-sectional measurement is cut with a diamond cutter then broken in liquid nitrogen.

3.1.2 Transmission electron microscopy

Besides the common aspects of SEM, high-resolution transmission electron microscopy (HRTEM) can additionally achieve ultra-high resolution, such as < 0.5 nm. Therefore, the crystal features are visible via HRTEM. The scanning area is controlled by two condenser lenses, then the transmitted electrons go through the lenses as follows: objective lens, objective apertures, diffraction apertures, intermediate lens, and the projector lens. For the specimen preparation, the powders are scratched from the samples, then sonicated in an ethanol solution. Afterwards, a few droplets of the powder solution are dropped on the finer mesh grids. After drying in room conditions, the TEM grid is transferred into an airlock for the measurement later.

3.1.3 Atomic force microscopy

Atomic force microscopy (AFM) is a powerful characterization method for inorganic and organic films in a magnification of Ångström. It is the ideal tool for characterization of the height profile of structured films. A laser beam is aligned on the cantilever, then the reflected signals are collected by a photodiode. In this thesis, the MFP-3D in a tapping mode from Oxford Asylum Research is used for the AFM measurement. The tetrahedral-shaped cantilever with a radius of 7 nm and a height of 14 µm (Oxford Asylum Research) is used. During scanning of the sample, the oscillation variations of the deflected laser, which are influenced by the Van-der-Waals force and Lennard Jones Potential, are detected by the photodiode. The final images, which consist of 256 × 256 data points, are analyzed by the software Gwyddion.[112]

3.1.4 X-ray diffraction

X-ray diffraction (XRD) is a commonly used technique to characterize the crystal phase, crystallite size and composition of phase mixtures. In this thesis, the Bruker D8 ADVANCE powder diffractometer, with a copper source ($K_{\alpha 1} : K_{\alpha 2}$ = 0.534) and a wavelength of 1.5418 Å, is used. The incident X-ray probes the sample at an angle of θ with respect to the samples; the diffracted beam with an angle of 2θ, is recorded by the detector. The program, named

DIFFRAC.SUITE, is used for setting the scanning protocol. A typical 2θ range of 20° to 60° is used for the titania films, however, a 2θ range of 10° to 80° is used for the perovskite films. The step size and counting time are set to 0.025 s and 20 s, respectively.

3.1.5 Grazing incidence X-ray scattering

Grazing incidence small-angle X-ray scattering (GISAXS) and grazing incidence wide-angle X-ray scattering (GIWAXS) are performed to characterize the morphology and crystal information, respectively.

For the data presented in section 5.2.1 and 5.3.1, the GISAXS experiments are performed at the SAXS beamline of the ELETTRA synchrotron radiation facility in Trieste. An 8 keV (λ= 1.54 Å) X-ray beam is focused to a size of 200 µm × 1 mm (vertical × horizontal). A sample-detector distance of 2070 mm is chosen. The scattering data are recorded with a Mar300 Image Plate detector. The incident angle is set to 0.48°.

For the data presented in section 6.1, the *in situ* GISAXS spray experiment is carried out at the PETRAIII P03 MiNaXS beamline at DESY with a photon energy of 13 keV, which corresponds to the wavelength of 0.957 Å. The Grafo T3 spray setup (Harder & Steenbeck), with a nozzle size of 0.4 mm, is implemented in combination with GISAXS. The sample-to-nozzle distance is 16 cm and the pressure of the N_2 carrier gas is 1 bar. A Pilatus 300k is used as a 2D detector to record the scattering data probed at an incidence angle of 0.245°. To avoid beam damage of the hybrid films, the sample stage is scanned along the y-direction (perpendicular to the x-ray beam direction) during the experiment, over a length of 6 mm in 0.05 mm steps. The data acquisition time for each frame is 0.1 s. 2 s of spray followed by 5 s wait time in one so-called spray cycle. In total 10 of such spray cycles are done.

For the data shown in chapter 8, GISAXS and GIWAXS experiments are performed at the P03 MINAXS beamline (PETRA III, DESY, Hamburg) with an energy of 13 keV, which corresponds to the wavelength of 0.957 Å. The finely focused X-ray with a size of 30 × 30 μm^2 impinges on the samples at an incident angle of 0.4°. A Pilatus 300k is used as a 2D detector to record the scattering data. The sample-to-detector distances are 4600 mm and 140 mm for GISAXS and GIWAXS measurements, respectively.

In this thesis, the Yoneda peak positions are calculated using the density of bulk material, in which the porous density is ignored.

3.2 Spectroscopic and electrical characterization

3.2.1 UV-Vis spectroscopy

UV-Vis spectroscopy is commonly used for the characterization of optical properties of films. In this thesis, the films are deposited on transparent substrates for UV-Vis measurement, such as glass, indium tin oxide (ITO), and fluorine doped tin oxide (FTO). A PerkinElmer Lambda 650 S with an integrating sphere (with a diameter of 150 mm) is used and controlled by the software PerkinElmer UV-Winlab. The available wavelength of the Lambda 650 S ranges from 190nm to 900 nm. After the wavelength of the incoming beam reaches 320 nm, the light source is switched from the deuterium lamp to halogen lamp automatically.

For the angular dependent UV-Vis measurement, the sample is mounted on the rotated sample holder, then put in the integrating sphere. When the incoming beam perpendicularly (with respect to the sample surface) probes the sample, the sample's angle of rotation is defined as 0°. The sample is measured in absorption mode with rotation angels from 0° to 80° in steps of 10°. In this configuration, the excess-calculated absorption is obtained. The directly reflected beam is mistreated as an absorption by the instrument. However, when the sample is tilted, the absorption is calculated correctly, due to the collection of reflected signal by the integrating sphere. When the titled angle is above 80°, the major part of the beam cannot probe the sample, which is attributed to the dimension of the incoming beam. Therefore, the absorption value obtained from the measurement always shows a smaller value than the real absorption of the films.

3.2.2 Photoluminescence spectroscopy

Photoluminescence spectroscopy (PL) is used for characterization of the radiative electron-hole recombination across the band gap. In this thesis, a Horiba Jobin Yvon Fluorolog (iHR320) machine is applied for this purpose. The PL measurement is carried out at Prof. Dr. Jochen Feldmann's group (Ludwig-Maximilians-Universtität München, Germany). The excitation wavelength is set to 365 nm (corresponding to an energy of 3.4 eV), which is well above the bandgap of perovskite (3.1 eV). The single wavelength beam is generated by a xenon lamp and then selected by a monochromator. The emitted signal of photons is recorded in a range of 400 nm to 600 nm. The data is analyzed by a software named PeakFit, using a Gaussian fitting model.

Time-resolved photoluminescence spectroscopy (TRPL), which is carried out at Prof. Dr. Jochen Feldmann's group (Ludwig-Maximilians-Universtität München, Germany) is used for carrier lifetime measurement. An excitation pulsed laser with a wavelength of 405 nm (Pico Quant LDH-P-C-405), which generates the photon-excited species in perovskite films, is chosen. For the samples with gold-titania core-shell nanoparticles, an additional excitation pulse laser with a frequency of 77.9 MHz, which aims to trigger the localized surface plasmon resonance, is focused on the sample at an angle of 30° with respect to the sample surface. The fluorescence signal is detected by a Hamamatsu C5680 streak camera with a resolution of a picosecond. The exponential decay is fitted by FluoFit, and a fluorescence decay is analyzed by PicoQuant.

3.2.3 J-V characterization

The solar cells are measured using a solar simulator (SolarConstant by K. H. Steuernagel Lichttechnik GmbH) or Newport Oriel Sol2A solar simulator under AM1.5G. The light intensity is calibrated with a silicon-based calibration solar cell with filters (WPVS Reference Solar Cell Typ RS-ID-3 by Fraunhofer ISE). Current-voltage characteristics of the perovskite solar devices are obtained by applying bias voltage with Keithley 2400.

There are several crucial parameters to determine the performance of the solar devices, such as short-circuit current density (J_{SC}), open-circuit voltage (V_{OC}), fill factor (FF), and power conversion efficiency (PCE). I_{SC} is defined as the current density at the point where V=0. V_{OC} is defined as the voltage at the point where $J=0$. FF and PCE are calculated using the equations as follows:

$$FF = \frac{P_{MP}}{P_{TMP}} \tag{3.1}$$

$$PCE = \frac{P_{out}}{P_{in}} = \frac{J_{SC}V_{OC}FF}{P_{in}} \tag{3.2}$$

where P_{MP} is the maximum power of the solar device, P_{TMP} is the theoretical maximum power, and P_{in} is the input power (normally P_{in} = 1000 W/m^2).

Additionally, the series resistance (R_s), which originates from the sheet resistance of the solar device, is determined by the slope of the J-V curve at the point of V_{OC}. It should be as small as possible. The shunt resistance (R_{sh}) influences the loss of the current. In order to reduce the leakage currents, R_{sh} should be as high as possible.

4. SAMPLE PREPARATION

In this chapter, the basic materials and processing steps, which were used in the sample preparation steps, are presented. More details about the parameters used for the respective investigations are provided in the corresponding chapters 5 to 8.

The information on the materials, which were used in the sol-gel synthesis, photolithography, thermal imprinting and perovskite materials, is provided in section 4.1. Section 4.2 introduces the different ways of processing the samples. The sol-gel synthesis process is introduced in section 4.2.1, while in section 4.2.2, spin coating, spray coating, and doctor blade coating are explained. Afterwards, the photolithography and thermal imprint process are introduced in section 4.2.3. Finally, the procedure for full assembly of a solar cell is provided in section 4.2.5, such as DSSCs, one step and two step methods for PSCs.

4.1 Materials

The materials used throughout the work can be classified into three categories: materials involved in the fabrication of the titania nanostructures via sol-gel process and corresponding DSSCs, the photoresist materials, and the perovskite materials including corresponding PSCs. All the materials through these studies were used as purchased.

4.1.1 Sol-gel synthesis

A promising approach for controlling the morphology of metal oxide films is based on self-assembly assisted by block copolymers. This approach was introduced by Stucky,[113, 114] Wiesner,[115] MeGehee,[116] and Gutmann[117] in the late 90s, and widely used in photovoltaics. Inorganic precursors are embedded in one domain of microphase-separated blocks. Afterwards, these hybrid films can subsequently be transformed into crystallized metal oxide films by calcination at high temperature.

Titania precursors and titania

Titanium(IV) isopropoxide (TTIP, 97%) is purchased from Sigma Aldrich and is used as the precursor for TiO_2. It has a physical appearance of transparent liquid with a relative density of 0.96 g/mL at 20 °C. The chemical structure of the titania precursor is shown in Figure 4.1. The chemical formula of TTIP is $C_{12}H_{28}O_4Ti$, where the titanium atom is surrounded by four $OCH(CH_3)_2$ ligands by an oxygen bond.

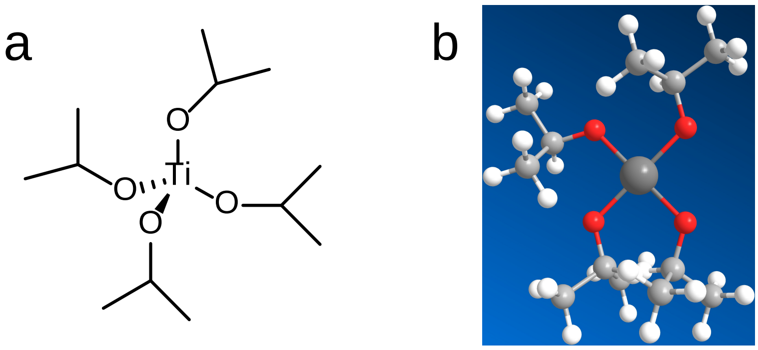

Figure 4.1 *a) Chemical structure of the titania precursor, known as titanium(IV) isopropoxide (TTIP). b) The 3D chemical structure of TTIP. The light and dark gray spheres represent carbon and titanium, respectively, while the white spheres represent hydrogen atoms, and the red spheres represent oxygen atoms.*

The titanium alkoxides are frequently used to produce titanium dioxide, according to the reaction equations 4.1 and 4.2[118, 119]

$$Ti(OR)_4 + 4H_2O \longrightarrow Ti(OH)_4 + 4ROH \tag{4.1}$$

$$Ti(OH)_4 \longrightarrow TiO_2 + 2H_2O \tag{4.2}$$

where R represents C_xH_{2x+1}. The reaction proceeds with a stepwise hydrolysis to produce $Ti(OH)_4$. Then the titania is produced by the condensation reaction of $Ti(OH)_4$. Titania is an inorganic wide band gap semiconductor, which has three major crystal phases, namely rutile, anatase and brookite. Anatase and rutile phase are the thermodynamically stable ones. Anatase phase shows a higher photocatalytic activity,[120] and exhibits a conduction band (CB) level of -4.0 eV and a valence band (VB) level of -7.8 eV, thus making titania primarily reactive to the UV light. Titania film has been proven to be an effective electron transport layer for hybrid solar cells and perovskite solar cells, with an electron mobility of 1.0×10^{-4} $cm^2V^{-1}s^{-1}$.[17, 121] Transparent titania commercial paste Dyesol's 18NRT is also used for the TiO_2 layer. It has highly-dispersed, stable anatase nanoparticles with an average nanoparticle size of 20 nm, and also exhibits optimal rheological properties that provide a good uniform surface and versatile porosity.

Polystyrene-*block*-polyethylene oxide and solvents

The block copolymer, named polystyrene-*block*-polyethylene oxide (PS-*b*-PEO), is used as a structure-directing agent. It is obtained from Polymer Source Inc., Canada, with a polydispersity index of 1.07 and PS fraction of 0.77. The average molecular weight is 30 kg/mol. The other batch of PS-*b*-PEO has a polydispersity index of 1.02, an average molecular weight is 20.5 kg/mol, and a PS volume fraction of 0.72. While the glass transition temperature is around 107 °C and -65 °C for PS and PEO block, respectively.

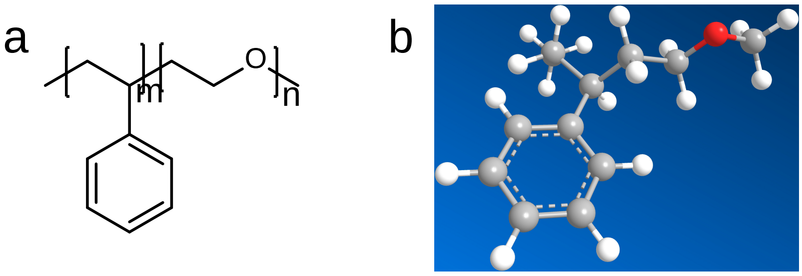

Figure 4.2 *a) Sketches of the chemical structure of PS-b-PEO. b) The 3D chemical structure of PS-b-PEO. The gray spheres represent carbon atoms, the white spheres represent hydrogen atoms, and the red spheres represent oxygen atoms.*

PS-*b*-PEO is an amphiphilic diblock copolymer. The polystyrene (PS) acts as the hydrophobic segment, whereas the polyethylene oxide (PEO) block acts as the hydrophilic segment. 1,4-dioxane (≥ 99.5%, extra pure) and HCl (37%, extra pure) are obtained from Carl Roth. 1,4-dioxane is used as a good solvent for both PS and PEO blocks, and HCl is used as a selective solvent.

4.1.2 Photolithography and imprinting materials

For all the various experiments with photolithography and imprinting processes, different masters have been used. These are OrmoStamps for soft embossing (thermal imprint), and polydimethylsiloxane (PDMS) stamps for wet imprinting.

For soft embossing, the materials OrmoPrime and OrmoStamp are used for imprint stamp fabrication. Both of them were purchased from micro resist technology, Berlin. They are designed for excellent pattern fidelity and have high thermal stability (up to 270 °C) and mechanical stability. For the photolithography step, the silicon (Si-Mat, (100) orientation, p-type boron doped) is used as a substrate for silicon master. The photoresist S1818, 351 Developer (both from Microposit) and hexamethyldisilazane (HMDS, from Micro resist technology) are used during silicon master fabrication. 351 developer is diluted with deionized water with a volume ratio of 1:5. The HMDS acts as an adhesion promotion layer for photoresists to stick to the silicon substrate. Before the thermal imprint, the silicon master is treated with anti-sticking agent 1H,1H,2H,2H-perfluorooctyltrichlorosilane (PFOTS), which is purchased from Sigma Aldrich.

For wet imprinting, polydimethylsiloxane (PDMS) is used for structure replicate media. This material is purchased from Dow Corning, which includes two components: the polymer and a curing agent. Both are transparent viscous liquids. However, after curing and drying, the PDMS hardens and transforms into a rubber state. The PDMS stamp replicates the periodic structure of a conventional blank compact disc (CD, Platinum 700MB, 4M Systems SA).

4.1.3 Perovskite materials

For 2D perovskite films, lead (II) bromide ($PbBr_2$, ≥ 98%, Sigma Aldrich), methylammonium bromide (CH_6BrN, MABr, Dyesol) and octylamine ($C_8H_{17}NH_2$, OA, Sigma Aldrich) are used. For 3D perovskite films, lead (II) iodide (PbI_2, 99.9985%, Alfa Aesar) and methylammonium iodide (MAI, Solaronix) are used. The chemical structure of MABr, MAI and OA are presented in Figure 4.3.

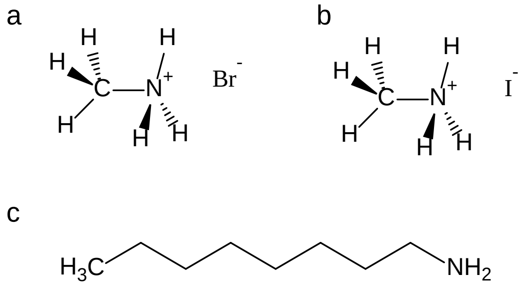

Figure 4.3 *Sketches of the chemical structures of a) MABr, b) MAI and c) OA.*

4.1.4 Other materials for solar cells fabrication

Both DSSCs and perovskite solar cells use 2,2',7,7'-tetrakis (N,N di-p-methoxyphenylamine) 9,9'-spiro-bi-fluorene (spiro-OMeTAD, Merck) as a hole-conducting layer. It is a disk shape molecule and shows charge mobilities on the order of 10^{-4} cm/Vs. The chemical structure of spiro-OMeTAD is shown in Figure 4.4 (a).

In DSSCs, the dye di-tetrabutylammonium cis-bis(isothiocyanato) bis (2,2'-bipyridyl-4,4'-dicarboxylato)-ruthenium(II) (N719) and 5-[[4-[4-(2,2-Diphenylethenyl) phenyl]-1,2,3-3a,4,8b-hexahydrocyclopent[*b*]indol-7-yl]methylene]-2-(3-ethyl-4-oxo-2-thioxo-5-thiazolidinylidene)-4-oxo-3-thiazolidineacetic acid (D149) are used. The chemical structures of dye N719 and D149 are shown in Figure 4.4 (b) and (c), respectively. Both of them are purchased from Sigma Aldrich. N719 is a ruthenium-based dye, which has an octahedral complex with two bipyridine ligands. M. Grätzel et al. reported this type of dye anchors to the TiO_2 surface via F-type anchoring mode (two of four carboxylic acid groups bridge the titanium ions in a bridging coordination, and the rest two carboxylic acid groups are in protonated state), which is verified by Fourier transform infrared spectroscopy (FTIR).[122] The organic dye D149 is a metal-free and environmentally friendly indoline dye. The extinction coefficient of D149 (68700 M^{-1} cm^{-1} at 526 nm) is around five times larger than that of ruthenium dye N719 (13900 M^{-1} cm^{-1} at 541 nm).[123, 124]

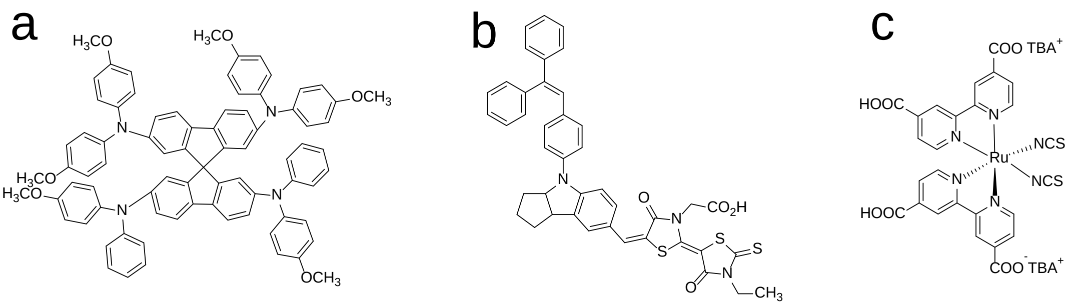

Figure 4.4 *Sketches of the chemical structures of a) hole conductor spiro-OMeTAD, b) organic dye D149, and c) the ruthenium-based dye N719.*

4.2 Processing

In this section, the several processing steps, through which the various nanostructured films can be obtained, are introduced, starting from preparation of the sol-gel solution, over different deposition methods, to photolithography and imprinting, then to perovskite films and solar cell fabrication.

4.2.1 Synthesis of nanostructures

Sol-gel wet chemistry is widely used to synthesize nanostructured titania films. Firstly, PS-*b*-PEO, which acts as structure guide, is dissolved in a non-selective solvent. In this study, the 1,4-dioxane ($C_4H_8O_2$) is used as a non-selective solvent, which means that it can dissolve both PS and PEO blocks. The diblock copolymer concentration of 16.09 mg/ml is fixed, if not defined otherwise. However, a small amount of 1,4-dioxane is split from the full amount of 1,4-dioxane, which is used to dilute the TTIP and HCl solution. It is important that the copolymer can still be dissolved thoroughly by the remaining 1,4-dioxane solution. The polymer solution is stirred for 1 hour at room temperature at 1100 rpm, then filtered by a poly-tetrafluoroethylene with a pore size of 0.2 µm (PTFE, $(C_2F_4)_n$, from Carl Roth). The diluted TTIP and HCl solution are refilled and injected using PTFE tubes at the speed of 0.7 ml/min and 0.25 ml/min, respectively, which is controlled by a motorized syringe (PHD 2000 Infuse/Withdraw, from

Harvard). After mixing solutions, the vial is sealed by parafilm and stirred for 1 hour at 800 rpm before spin coating or spray coating.

Another method to achieve titania film is spin coating with diluted commercial titania paste (Dyesol 18NRT). 18NRT paste is diluted in ethanol with the weight ratio of 2:7. The mixture is under ultrasonication for 3 hours at room temperature, then transferred to the shaker and shaken for 24 hours. Then the stock solution is sealed and stored at room temperature. For DSSCs, the 18NRT paste is used as purchased.

Anatase phase of titania film, obtained from both of sol-gel and commercial paste methods, crystalizes through high temperature calcination step. In this step, samples are placed in a tube furnace (GERO or Heraus instruments) in ambient atmosphere. For sol-gel processed film, the samples are calcinated at 450 °C for 30 min after heating at a rate of 2 °C/min, if not defined otherwise. During this step, the polymer matrix is removed and the amorphous titania crystallizes to anatase phase. For the diluted commercial paste processed film, the samples are calcinated at 500 °C for 30 minutes after heating at a rate of 2 °C/min.

4.2.2 Deposition methods

In this study, the films are deposited on solid substrates, such as silicon substrate (Si-Mat, (100) boron doped), glass (soda-lime glass) or fluorine-doped tin oxide (FTO, NSG Tec 7, Pilkington, 80% - 82% of visible transmittance, 6 - 8 Ω/□). Before deposition, the substrate is cleaned by an acid bath or a sequential ultrasonic bath. The latter is explained in section 4.2.5.

Acid cleaning

To remove the dust, organic remains, and silicon dioxide from the surface of silicon substrates, the silicon substrates are cleaned with an acid solution. 54 mL of deionized water (DI water), 84 mL of hydrogen peroxide (H_2O_2, from Carl Roth) and 198 mL of sulfuric acid (H_2SO_4, from Carl Roth) are mixed together in a pre-cleaned glass beaker at room temperature. Afterwards, the acidic bath is heated up to 80 °C, before the silicon substrates are immersed into the bath for 15 mins. The silicon substrates are then rinsed with copious amounts of DI water. After rinsing, the substrates are dried by nitrogen and then directly followed by deposition of the desired films. The surface of the substrates shows a hydrophobic property after acid cleaning.

Spin-coating

Spin-coating is widely used in thin film production, and it provides high reproducibility and homogeneity of the thin films. Spin-coating is a fast-non-equilibrium process, which includes three steps: firstly, during the turbulent process, the majority of the solution dropped on the substrate is flung-off already; secondly, a convection-dominating process is started; finally, the solvent diffuses to the interface of film and air, and evaporates. However, the typical maximum thickness is 1 µm. In this thesis, a Delta 6 RC TT (Süss MicroTec Lithography GmbH) spin-coater is used. The substrates, which are held by a vacuum during rotation, are placed on the chuck of the spin-coater. An acceleration, rotation speed and rotation time are defined by a controller program. Normally, the solution is dropped on the center of the substrate, then the defined program is started immediately. However, for the compact TiO_2 film of the perovskite solar cell, it is spin-coated dynamically, which means the solution is dropped after the stage reaches the final rotation speed, which produces homogenous thin titania film.

There are several impact factors concerning the thickness of the final film, such as spinning speed, concentration of the polymer solution, and viscosity.[125] However, for the sol-gel complex solution, it is difficult to control the film thickness through changing the concentration and viscosity, due to the interaction of each component. Multiple spin-coating provides one possible method to achieve a thicker film. Samples are left on the chuck after finishing the previous spin-coating step, then the solution is dropped on the sample again before starting the next spin round. It effectively increases the film thickness. However, the homogeneity of the final films becomes worse starting from 4 or more spin-coating cycles.

Blade coating

In this study, blade coating is used for depositing the titania films with thicknesses in the micrometer range. Scotch tape is used as a spacer, which defines the thickness of the film. The blade is purchased from Carl Roth.

Two layers of scotch tape are attached to the long side of the substrate, then the TiO_2 paste is placed on the top edge of the substrate. The paste is spread over the substrate by blading the paste from top to bottom at an angle of around 45°. The strips of the scotch tape are removed directly after drying at room temperature.

Spray coating

Spray coating is an up-scale deposition method, which provides uniform and high-quality coating. It has been applied in photovoltaic applications,[126-128] energy storage devices,[129, 130] catalysis,[131, 132] and electrode layer coating[133, 134]. It can be simplified into three processing steps: the atomization of the ink solution by N_2 gas, aerosol transport of the droplet, and droplet deposition on the substrate and film growth.

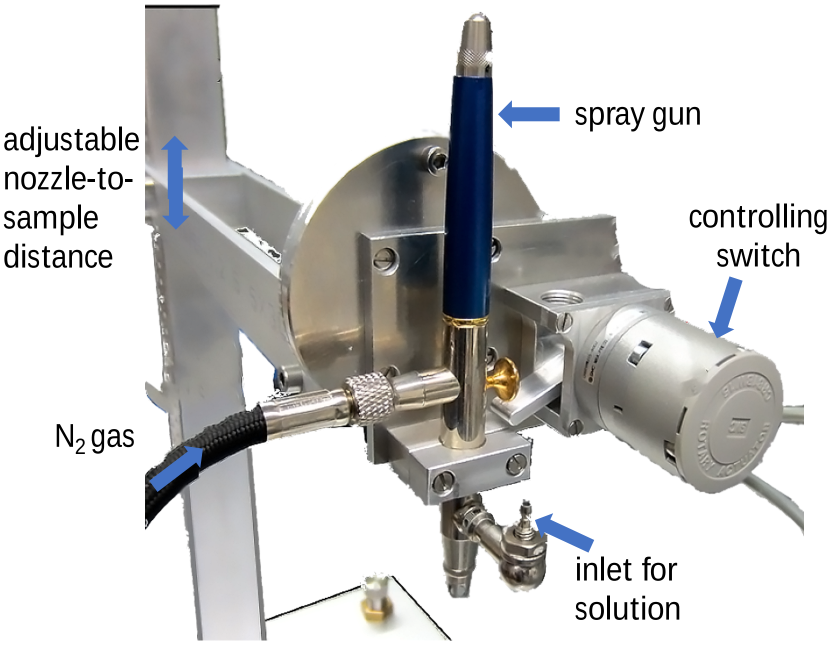

Figure 4.5 *Photograph of semi-automatized spray set up.*

The spray setup is shown in Figure 4.5. The substrate is placed on a heating state directly under the spray nozzle. There are several spray parameters which influence the film homogeneity, thickness, and morphology. Such parameters include pressure of carrier gas, nozzle-to-sample distance, substrate temperature, spray speed, and spray protocol. More details are discussed in section 6.2.

For the *in situ* GISAXS experiment, which is carried out at the PETRAIII beamline P03 MiNaXS at DESY, the sample is placed on a heating stage (DHS 1100, Anton Paar) at a constant temperature of 50 °C. The Grafo T3 (Harder & Steen-beck) spray setup is operated with a nozzle size of 0.4 mm. The sample-to-nozzle distance is 16 cm and the pressure of the N_2 carrier gas is 1 bar. A Pilatus 300k is used as a 2D detector to record the scattering data probed at an incidence angle of 0.245°, which was chosen to be well above the critical angles of PS (0.09°), PEO (0.10°) and TiO_2 (0.18°). To avoid beam damage of the hybrid films, the sample stage is scanned along the y-direction (perpendicular to the X-ray beam direction) during the experiment over a range of 6 mm in 0.05 mm steps. The data acquisition time for each frame is 0.1 s. 2 s of spray followed by a wait time of 5 s in one so-called spray cycle. In total 10 of such spray cycles are done.

4.2.3 Photolithography process and imprinting

In this section, the general photolithography process, imprint Ormostamp fabrication and imprint methods (wet imprinting and nano-imprinting) are introduced. Hybrid titania films are prepared by blade coating for wet imprinting, and prepared by spin coating for nano-imprinting.

Photolithography process

Silicon substrates, with the size of 3 x 3 cm^2, are cleaned by acid bath. In order to promote the adhesion of the photoresist to the silicon surface, the substrates are functionalized by hexamethyldisilazane (HMDS). After heating substrates to 160 °C for 10 mins, during which moist residuals are removed from the surface, the substrates are cooled down to room temperature and placed in an evaporation setup (Figure 4.6). 500 µl of HMDS is evaporated onto the silicon surface at 80 °C, which is well below the boiling point of HMDS (120 °C). The sample is taken out after 2 mins of evaporation, and is covered with less than 10 nm of HMDS layer.

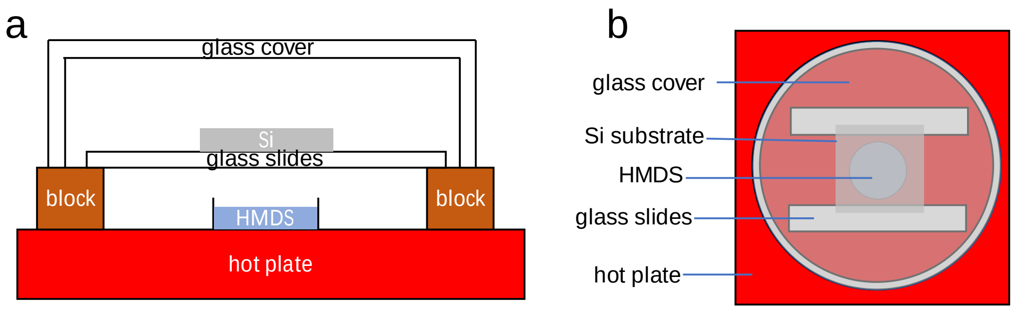

Figure 4.6 *Schematic setup for HMDS evaporation. a) The cross-sectional view of evaporation setup. b) The top view of the evaporation setup.*

After functionalizing the substrate with HMDS, the samples are spin coated by positive photoresist (S1818, Microposit) at 4000 rpm for 30s. Afterwards, the samples are soft-baked on a hotplate at 115 °C for 1 min, then cooled down to room temperature.

A mask aligner (MJB 3, Karl Suss) is used for the UV exposure step. The UV-light is created by a mercury arc lamp with a wavelength of λ=365 nm. The illuminated area is controlled by a chromium mask. Afterwards, the samples are dipped into the developing solution (351 developer, diluted by DI water with a ratio of 1:5, Microposit), then dipped into DI water to stop further development from any residual developer solution. After drying with nitrogen, the samples are heated on a hotplate at 120 °C for 5 min for the so-called hard-bake, aiming to enhance the mechanical stability and eliminate the light sensitivity of the film.

Afterwards, the samples are etched by reactive ion etching (Oxford Plasma Lab 80 Plus) under the following conditions: 220 W as forward power, 20 W as a reflected power, C_4F_8 and SF_6 as gas sources, 25 °C and 15 mTorr. The etching depth is controlled by the time with a constant etching rate. Finally, the samples are put into an ultrasonic acetone bath at 50 °C for 10 min to remove the photoresist remains. A schematic sketch of the photolithography process is shown in Figure 4.7.

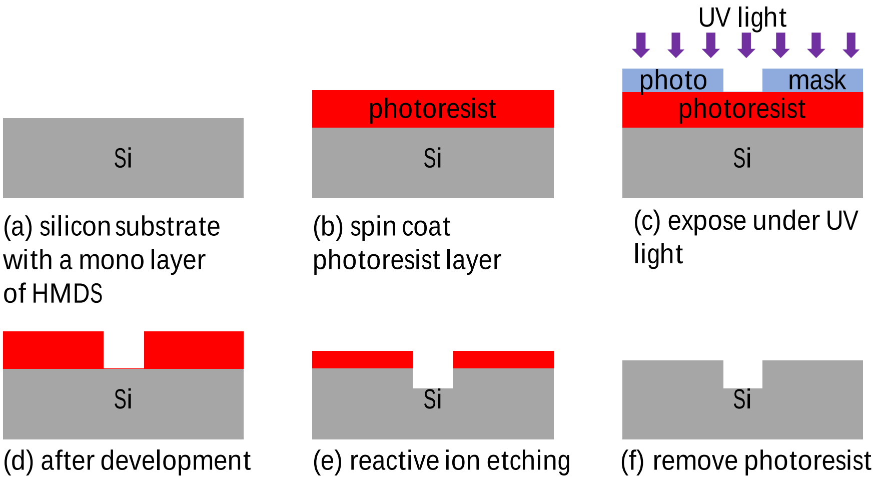

Figure 4.7 *Sketch of the photolithography process. a) silicon substrate with a monolayer of HMDS, b) after spin coating photoresist layer, c) exposure step, d) after development, e) after reactive ion etching, f) final silicon master after removing photoresist.*

Ormostamp fabrication

The OrmoStamps are fabricated in a clean room, to achieve a defect-free replica. Firstly, the silicon masters are treated by trichloro(1H,1H,2H,2H-perfluorooctyl) silane (PFOTS) in a desiccator with a certain vacuum for 1 h, during which multiple layers of PFOTS are deposited on the Si substrates. To achieve a monolayer of PFOTS, the silicon masters are heated at 150 °C for 1 h.

Secondly, thin glass slices (0.15 mm of thickness, 50 mm of diameter, Thermo Scientific) are cleaned in an ultrasonic acetone bath at 60 °C for 10 min. After drying with nitrogen, the substrates are cleaned by oxygen plasma (Alpha Plasma Asher) at 600 W for 6 min to enhance the adhesion of Ormoprime on the silicon surface. Ormoprime is spin coated onto the glass substrates with 4000 rpm for 60 s. Afterwards, the samples are heated at 150 °C for 5 min.

Finally, 15 µL of Ormostamp solution is dropped onto the pretreated silicon master, then the functionalized glass slice is placed on top. Once the structured area of the silicon master is completely covered by Ormostamp solution, it is then treated by UV light by Mask aligner in soft contact mode with a 350 W mercury arc lamp for 2 min. The glass slice is peeled off the silicon master, then post-baked on a hotplate at 130 °C for 30 min.

Before using the Ormostamp samples, they are cleaned with oxygen plasma at 200 W for 1 min and treated by PFOTS as mentioned above, which aims to increase the hydrophobic property of the stamps.

Wet imprinting

Recordable compact discs (CDs) are used as the imprint master, which have channel structures with a height of 125 nm, a width of 175 nm, and a periodicity of 1.5 µm. After removing a thin aluminum layer of the compact disc, it is cleaned by isopropyl alcohol bath then dried by nitrogen.

To fabricate of the PDMS stamp, silicone-elastomer and curing agent (Sylgard 184) are mixed together with a weight ratio of 10:1. Then, the mixture is transferred into a vacuum chamber for 30 min. The bubble-free PDMS liquid is poured into a square aluminum frame on top of the precleaned CD master. Subsequently, the whole system is placed in a vacuum furnace. After applying a short vacuum, it is heated at 60 °C overnight. To avoid tearing off the PDMS stamp, it is peeled off the CD master along the channel direction. Before using the PDMS stamp, it is treated with oxygen plasma (240 W, 0.4 bar, 30 s), then treated with PFOTS.

After blade coating the commercial titania paste onto the substrate, it is heated at 70 °C for 15 min. Then, the PDMS stamp is placed on the substrate with a 0.26 kg metal block on top. Afterwards, it is put into an oven at 80 °C for 1 h.

Thermal nano-imprint

Thermal nano-imprint is a top-down technique for structuring the film. In this thesis, we combine the sol-gel method, which is a bottom-up technique, with nano-imprint to obtain a hierarchical structure of the titania film. Figure 4.8 shows the sketch of the preparation of hierarchical structured titania films via nano-imprint.

The titania hybrid film is prepared by a sol-gel route. PS-*b*-PEO is firstly dissolved in 1,4-dioxane with a concentration of 16.5 mg/ml, then stirred for 1 hour at 800 rpm at room temperature. After filtration with a PTFE filter with 0.2 µm pore size, the TTIP and HCl, which are dissolved in 1,4-dioxane solution, are added using a syringe pump (PHD 2000, Harvard Apparatus) with an infusion speed of 0.25 ml/min. During infusion, the solution is stirred at 1100 rpm. After the mixing of TTIP and HCl into the solution, the final solution is stirred for 1 hour at 800 rpm. The final solution consists of 1,4-dioxane, HCl and TTIP with a weight ratio of 0.92:0.01:0.07. The hybrid titania film is spin-coated at 2000 rpm for 60 s with the fastest acceleration, and spin-coated three times to achieve the desired thickness of around 500 nm.

After spin-coating, the hybrid film is placed on the imprinter (NIL-2.5, Obducat) with an Ormostamp on top. Then several thin aluminum foils are covered on top of the sample to protect the hydraulic press from the sharp edges of the sample. The imprinting process is performed at 130 °C, under the pressure of 55 bar for 30 min. Afterwards, the composite film is cooled down to 60 °C with a cooling nitrogen gas flow to demold the stamp. The parameters for the imprinting step are shown in Figure 4.9.

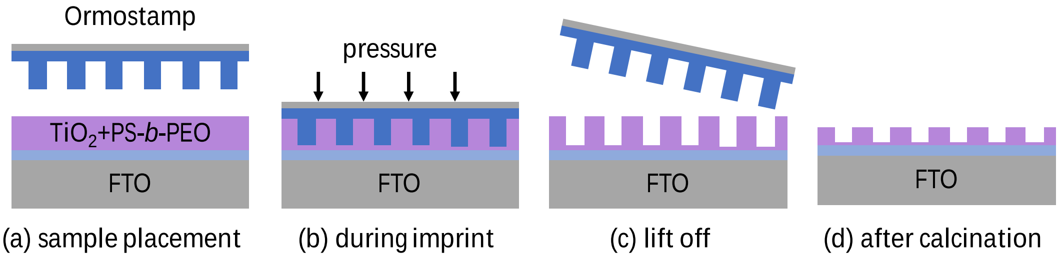

Figure 4.8 *Sketch of preparation of hierarchical structured titania film via nano-imprint. a) An Ormostamp is placed on the sol-gel prepared film. b) The Ormostamp is pressed into the film at elevated temperature and pressure. c) The Ormostamp is lifted off from the film after imprinting. d) Titania film after calcination.*

Finally, the samples are calcinated at 500 °C for 30 min after heating at a rate of 2 °C/min. The polymer is extracted from the film, and the crystalized titania film with anatase phase is obtained after calcination. However, the depth of the structure is reduced, due to the removal of the polymer template.

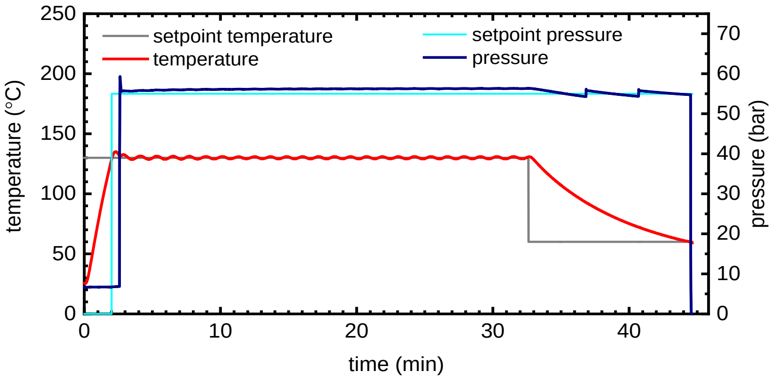

Figure 4.9 *Recorded parameters during imprinting. The light blue and grey curves represent the setpoint of pressure and temperature, respectively, while the working pressure and temperature are shown in deep blue and red curves, respectively.*

4.2.4 Perovskite films fabrication

For the preparation of $MAPbI_3$ film, the PbI_2 (99.9985%, Alfa Aesar) is dissolved in DMF (1 M) for 1 hour under 100 °C. MAI (methylammonium iodide, Solaronix) is dissolved in 2-propanol with a concentration of 40 mg/ml for 1 hour at 70 °C. After filtration with a 0.45 µm filter, the solution is allowed to cool down to room temperature. The PbI_2 solution is spin coated at 3000 rpm for 30 s, then after the solution is cooled to room temperature. Afterwards, the MAI solution is spin coated at 3000 rpm for 20 s. Then, substrates are annealed at 100 °C for 1 h in a nitrogen-filled glove box.

For the preparation of $(MA_xOA_{1-x})PbBr_3$ films, all the vials are cleaned with anhydrous DMF (99.8%, Sigma Aldrich) and dried in a vacuum oven overnight. Firstly, 1 M of $PbBr_2$ and 3.5 M of MABr are dissolved in DMF separately, and stirred at 80°C with 150 rpm for 60 min and 15 min, respectively. Octylamine is also kept at 80°C. Secondly, the solutions are mixed in a molar ratio of 1 ($PbBr_2$) : 0.8 (MABr) : 0.2 (OA) for 2D perovskite, and 1 ($PbBr_2$) :1 (MABr) for 3D perovskite, respectively. The final solution is stirred for 45 min.

The hot perovskite solution is spin-casted at 3000 rpm for 200 s on the pre-heated (100°C) mesoporous titanium dioxide substrates. Sequentially, the samples are placed on a hotplate at 100°C for 10 min for the final perovskite crystallization.

4.2.5 Solar cell fabrication

In this section, the standard procedure of dye-sensitized solar cells (DSSCs) is firstly introduced before fabricating procedures of perovskite solar cells (PSCs) based on MAPbI3 and $(MA_xOA_{1-x})PbBr_3$ are discussed. The parameters for the imprinting step are mentioned in section 4.2.3.

DSSCs fabrication

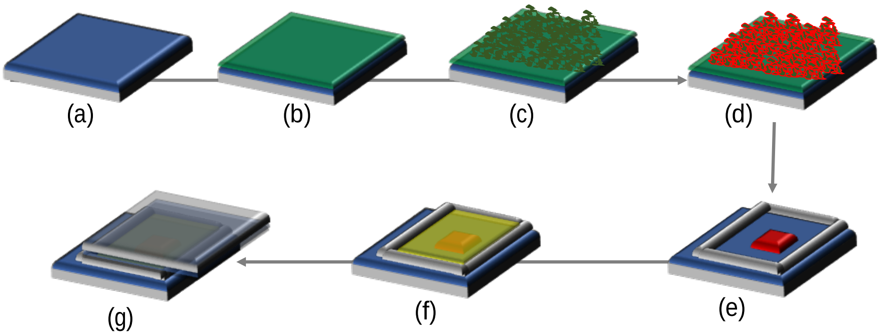

Figure 4.10 *Sketch of standard procedures for fabrication of electrolyte dye-sensitized solar cells: a) precleaned FTO glass; b) spin coat with a compact titania layer; c) blade coat with mesoporous titania layer; d) soak into dye solution; e) the active layer is scratched off, leaving behind only a small area, and teflon spacer is attached with grease; f) the electrolyte is filled within the spacer; g) the platinum counter electrode is mounted on top.*

The sketch of the necessary steps in Figure 4.10 shows the standard process for DSSCs assembly. For imprint samples, wet-imprinting starts after blading the commercial titania paste. The details about wet-imprinting are explained in section 4.2.3.

Substrate cleaning: Fluorine-doped tin oxide glass (FTO, NSG Tec 7, Pilkington, 80% - 82% of visible transmittance, 6 - 8 Ω/□) is used as transparent conductive substrates, and cut into sizes of 2.5 by 5 cm^2. The substrates are cleaned with five sequential ultrasonic baths for 10 min each: the solvents used for each individual bath are as follows: Alconox detergent with a concentration of 16 g/L, DI water, ethanol, acetone and isopropanol. The bath and rinse sequences are as follows: 1) Alconox bath and DI water rinse; 2) DI water bath and DI water rinse; 3) ethanol rinse and ethanol bath; 4) ethanol rinse and acetone rinse; 5) acetone bath and acetone rinse; 5) isopropanol rinse and isopropanol bath; 6) isopropanol rinse. After drying with nitrogen, the substrates are treated with oxygen plasma (240 W, 0.4 mbar, 10 min) to remove all organic residues, resulting in the improvement of hydrophilicity of the FTO surface.

Plasma treatment: The samples are cleaned by O_2 plasma to remove any remaining organic residues and free radicals. The substrates are placed in a petri dish, then transferred to the plasma chamber (Nano plasma asher, Diener). The oxygen gas is injected after 0.1 mbar has been reached. After adjusting the flux of oxygen gas, the pressure in the chamber is stabilized at 0.4 mbar. Then, a power of 250 W is applied for 10 min.

After plasma treatment, the surface of the FTO glass becomes more hydrophilic. The following layer is deposited sequentially within 5 min.

Compact titania layer: A compact titania layer acts as a hole-blocking layer to prevent the hole transfer material from infiltrating through the mesostructured metal oxide layer and directly making contact with the FTO electrode. The hole blocking layer is prepared as described in Yu's paper.[135] Solution A contains 2.625 ml of ethanol, 0.85ml of tetrabutyl titania (titanium (IV) n-butoxide, TNBT, $C_{16}H_{36}O_4Ti$), and solution B contains 1.25 ml of ethanol and 0.045ml of DI water. After stirring solution A for 60 min, solution B is added dropwise to solution A. The final solution is stirred for 24 h before spin coating. The precleaned FTO substrates are covered with scotch tape on both long edges to protect it from the compact layer. This protected area is used for contacting FTO in *J-V* measurement. Then the solution for compact titania layer is spin-coated at 2000 rpm for 60 s without acceleration time. After spin-coating, the tape is removed from the samples then the samples are calcinated at 450 °C for 2 h after heating at a ramp of 6.25 °C/min. The thickness of the compact titania layer is around 140 nm.

$TiCl_4$ treatment: Two consecutive $TiCl_4$ treatments are performed for DSSCs fabrication, one before and one following the blading of the mesoporous titania layers. The initial $TiCl_4$ treatment enhances the bonding strength between compact and mesoporous titania layer, and also prevents the charge recombination between FTO and I_3^-.[136] The second $TiCl_4$ treatment enhances the surface roughness and necking of TiO_2 particles, which can augment dye adsorption and result in a higher photocurrent.[137] The 3 M stock solution of $TiCl_4$ in DI water is prepared in a salted ice bath below 0 °C. The low temperature, which can reduce the reaction rate of $TiCl_4$ with H_2O, is crucial to obtain a clear solution without titania clusters, and with the desired concentration of $TiCl_4$. 0.4 ml of $TiCl_4$ stock solution is added into 29.6 ml of DI water while stirring at room temperature. After stirring for 15 min, the $TiCl_4$ bath is heated up to 70 °C. The samples are covered with tape in the previously tape-covered areas, then immersed into $TiCl_4$ bath for 30 min. Afterwards, the samples are taken out and rinsed with DI water and ethanol. The samples are calcinated at 500 °C for 30 min after heating at a ramp of 25 °C/min.

Mesoporous titania layer: In section 4.2.2, the blade coating of mesoporous titania layer is described. Thus, in this part, only a few procedures after blade-coating are introduced. The samples are kept in room environment for 30 min after blade-coating, then placed on the hotplate at 125 °C for 5 min. Afterwards, the samples are calcinated with a ramp, which shows in Figure 4.11. Then $TiCl_4$ treatment and calcination steps are needed as mentioned above.

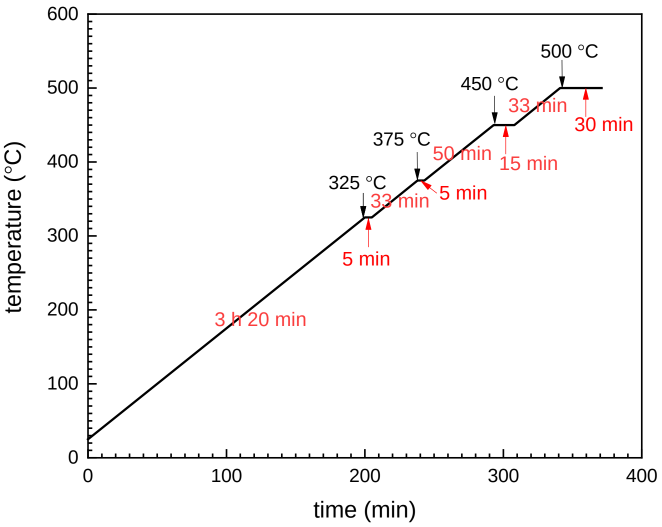

Figure 4.11 *A ramp for the calcination step of 18NRT commercial paste.*

Dye and electrolyte: The dye is dissolved in a solution of 1:1 volume ratio of acetonitrile and tert-butanol with a concentration of 0.5 mM. It is stirred for 24 hours and stored at room temperature with an aluminum shield. After heating the samples at 80 ºC for 10 min, the samples are sequentially put into D149 dye solution for 1 hour. Afterwards, the samples are rinsed with acetonitrile to remove superfluous dye solution, then dried with nitrogen. A teflon spacer (25 x 20 x 0.1 mm^3) with a hole (18 x 12 mm^2) is used as the reservoir for loading the electrolyte solution. To prevent the leakage of the electrolyte, a grease is applied on both sides of the teflon spacer. An organic solvent-based electrolyte solution is loaded drop by drop on the active area. This solution consists of 50 mM iodine (Sigma-Aldrich), 0.1 M lithium iodide (Sigma-Aldrich), and 0.6 M 1,2-dimethyl-3-propylimidazelium iodide (Solaronix), in methoxypropionitrile (Sigma-Aldrich). It is loaded drop by drop on the active area.

Counter electrode: Two strips of scotch tape are fixed on the two sides of the precleaned FTO glass. The platinum paste (PT-1, Dyesol) is bladed, followed by drying at 60 ºC for 2 hours, and calcination at 400 ºC for 15 min. After loading the electrolyte, the FTO glass with a counter electrode is placed on top of teflon spacer. Mauly paper clips are used to stabilize the DSSC device.

PSCs fabrication

The procedures of PSCs based on $MAPbI_3$ and $(OA)_2MA_{n-1}Pb_nBr_{3n+1}$ are summarized in Figure 4.11 and Figure 4.12, respectively. The substrate cleaning and plasma treatment steps are the same as DSSCs fabrication.

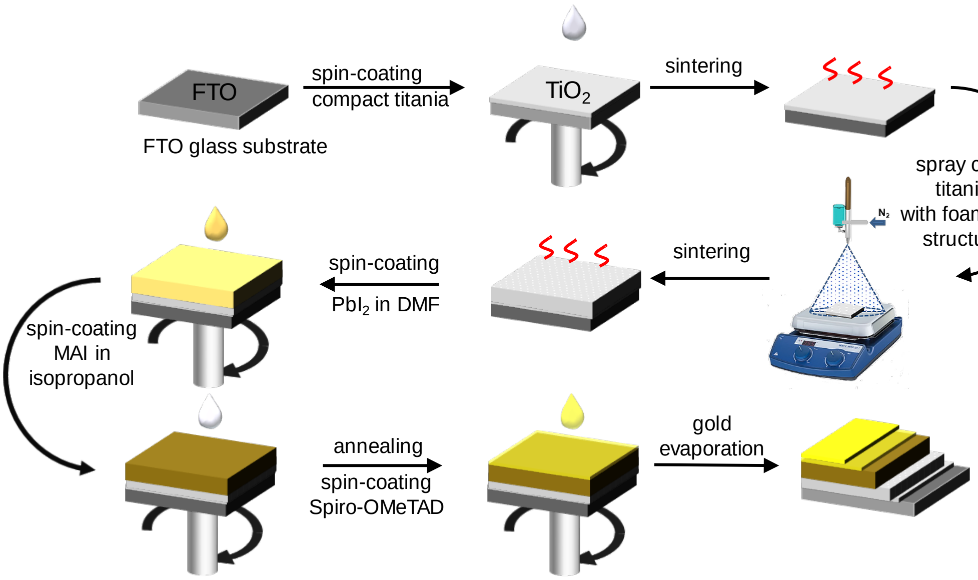

***Figure 4.12** Sketch of fabrication steps for PSCs based on $MAPbI_3$ as a perovskite layer.*

Compact titania layer: A compact layer fabrication for PSCs is adapted from Leguy and coworkers.[138] 2.5 mL of anhydrous isopropanol is added into two vials, respectively. In the first vial, 35 µL of 2M HCl, which is diluted by anhydrous isopropanol, is added and shaken for 10 min. In the second vial, 369 µL of titanium isopropoxide is added while stirring and then stirred for 10 min. Afterwards, the solution in the first vial is added into the second vial dropwise under heavy stirring. After stirring for 1 hour, 200 µL of the solution is spin-coated dynamically on the FTO substrate at 2000 rpm for 45 s. The samples are placed on the hotplate at 150 °C for 10 min. Finally, the samples are transferred into a furnace, and heated to 500 °C for 45 min with a ramp of 500 °C/h.

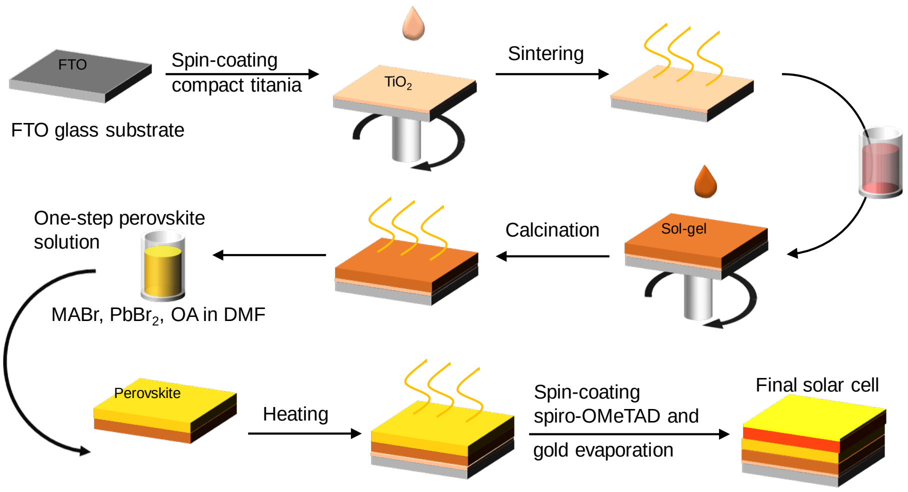

***Figure 4.13** Sketch of fabrication steps for PSCs based on $(OA)_2MA_{n-1}Pb_nBr_{3n+1}$ as a perovskite layer.*

Mesoporous titania layer: The copolymer assisted sol-gel recipe is used. The block copolymer named polystyrene-*block*-polyethylene oxide (PS-*b*-PEO) is obtained from Polymer Source Inc., Canada, with a polydispersity index of M_w/M_n = 1.02. The average molecular weight is 20.5 kg/mol with f_{PS} of 0.72. After dissolving it in 1,4-dioxane (≥99.5%, extra pure, Carl Roth), polytetrafluoroethylene filters (PTFE, Carl Roth GmbH) with 0.2 µm pore size are used for removing large particles. An appropriate amount of titanium(IV) isopropoxide (97% TTIP, Sigma Aldrich) and hydrochloric acid (37% HCl, extra pure, Carl Roth) are diluted by 1,4-dioxane, then injected into the copolymer solution by a speed of 0.25 ml/min. The concentration of the copolymer is 16.09 mg/ml in the final solution, and the weight ratios of 1,4-dioxane, TTIP, and HCl are 0.92, 0.07 and 0.01, respectively. Moreover, the microfluidic method is used for mixing during the sol-gel synthesis with an injection rate of 0.25 mL/min, which controls the reaction speed when adding hydrochloric acid (HCl) and titanium tetraisopropoxide (TTIP).[139] The final solution is stirred for 45 min before use. All the materials are used as received without further purification.

For PSCs based on $MAPbI_3$ as a perovskite layer, the film is deposited via spray coating. The Grafo T3 (Harder & Steenbeck) spray setup is operated with a nozzle size of 0.4 mm. The sample-to-nozzle distance is 16 cm and the pressure of the N_2 carrier gas is 1 bar. Spray shots of 2 s are followed by a 5 s wait time in one so-called spray cycle. In total 10 of such spray cycles were done. For the PSCs based on $(OA)_2MA_{n-1}Pb_nBr_{3n+1}$ layer, 200 µL of the final solution is spin-coated at the samples at 2000 rpm for 1 min. Multiple spin-coating is applied to achieve the desired film thickness.

Finally, the samples are calcinated at 500 °C for 45 min after heating at a ramp of 500 °C/h. $TiCl_4$ treatment follows, which is done to improve the interface between titania layer and $(OA)_2MA_{n-1}Pb_nBr_{3n+1}$ layer.

Perovskite layer: For the $MAPbI_3$ layer, the PbI_2 (99.9985%, Alfa Aesar) is dissolved in DMF (1 M) for 1 hour under 100 °C. MAI (methylammonium iodide, Solaronix) is dissolved in 2-propanol with a concentration of 40 mg/mL for 1 hour at 70 °C. After filtration with a 0.45 µm diameter filter, the solution is cool down to room temperature. The PbI_2 solution is spin coated at 3000 rpm for 30 s and afterwards kept at room temperature for 10 min. Next, the MAI solution is spin coated at 3000 rpm for 20 s. The substrates are annealed at 100 °C for 1 hour in a nitrogen-filled glove box.

For the $(OA)_2MA_{n-1}Pb_nBr_{3n+1}$ layer, 1M of $PbBr_2$ is dissolved in DMF at 80 °C for 1 hour. After 45 min, 3.5 M of MABr is dissolved in DMF for 15 min at 80 °C. Meanwhile, octylamine is also heated at 80 °C. Afterwards, the solutions are mixed in a molar ratio of 1:0.8:0.2 for $PbBr_2$, MABr and OA, respectively. After stirring for 45 min, the hot spin coating proceeds. The samples are preheated at 100 °C, then immediately transferred to the sample holder. The hot perovskite solution is spin-coated at 3000 rpm for 200 s. Afterwards, the samples are placed on a hotplate at 100°C for 10 min.

Hole transfer layer: After the perovskite annealing, a spiro-OMeTAD solution (70 mM in chlorobenzene) is spin coated at 4000 rpm for 30 s. The spiro-OMeTAD solution is doped with bis (trifluoromethylsulfonyl) imide lithium salt (Li-TFSI, Sigma-Aldrich), tris(2-(1H-pyrazol-1-yl)-4-tert-butylpyridine)-cobalt(III)tris(bis(trifluoromethylsulfonyl) imide) (FK209 Co(III) TFSI salt, Dyesol) and 4-tert-butylpyridine (TBP, Sigma-Aldrich). The molar ratios of additives for spiro-OMeTAD were: 0.5, 0.03 and 3.3 for Li-TFSI, FK209 and TBP, respectively.

Counter electrode: The gold counter electrode is deposited by thermal deposition, using a shadow mask. 190 mg of gold is evaporated within 2 min till the chamber pressure reaches 2×10^{-5} mbar.

5. COMBINATION OF SOL-GEL WITH SPRAY COATING METHOD

Parts of this chapter have been published in the article: Pore size control of block copolymer-templated sol–gel-synthesized titania films deposited via spray coating[38] (B. Su, V. Körstgens, Y. Yao, D. Magerl, L. Song, E. Metwalli, S. Bernstorff, P. Müller-Buschbaum, J. Sol-Gel Sci. Technol., 81, 346-354, 2017, DOI: 10.1007/s10971-016-4134-9)

Titania is widely used in different applications as a low-cost and 'high-efficiency' material. For example, Burschka *et al* reported solid-state dye-sensitized solar cells with a record power conversion efficiency of 7.2%[140]. High efficiency perovskite solar cells with champion power conversion efficiencies of 20.8% are reported by Bi *et al.* [141]. Both types of solar cells are using mesoporous titania. In general, for a successful commercialization of titania films, a coating of large-scale sample surfaces would be very beneficial. In this respect, the use of spray coating is very interesting but only rarely investigated today. Spray coating is a solution-based deposition method [133], which can be easily scaled-up and which enables the coating of films on complex substrate geometries. Moreover, it allows for a layer-by-layer deposition, involving a highly dynamic size distribution of the droplets atomized by a carrier gas. In this method, the spray solution can be organic solutions, polymers with poor solubility, as well as hybrid materials, such as colloidal nanoparticles and wet powder suspensions. Due to these advantages, spray coating has been applied in many different research areas. For example, in the field of solar energy harvesting, spray coating is used for depositing the active blend layer of organic solar cells [127, 134, 142-144], the active layer of dye-sensitized solar cells [145] as well as the hole blocking layer of perovskite solar cells [8, 146].

In general, due to the large surface-area-to-volume ratio, mesoporous titania structures are widely used in catalysis [43, 147], sensors [45, 148], fuel cells [149], and especially in photovoltaics [150-153]. Three-dimensional (3D) titania nanostructures can be achieved through a broad range of chemical and physical methods, such as chemical vapor deposition [154, 155], electrostatic spray deposition [156], spin coating titania particles [157], magnetron sputtering [158-160], growth driven by catalysis [161], and sol-gel chemistry deposition of titania [162-166]. In solar energy harvesting, 3D titania nanostructures with a large surface to volume area play an important role in boosting the solar cell power conversion efficiencies. However, for photovoltaic applications, the random sintering of nanoparticles to form a mesoporous titania network has drawbacks, including the lack of control over the pore size distribution, which can cause inefficient electron diffusion through the random mesoporous structures [15-18]. One way to overcome this challenge is to apply copolymers as a structure-directing template in the sol-gel route [19]. 3D bicontinuous network pore structures, where the titania scaffold and pores are interlinked via two continuous networks, can be obtained via a microphase separation and micelle formation process of the block copolymer with a titania precursor in solution [114]. So far, the majority of investigations making use of such block copolymer assisted sol-gel chemistry routes have used the spin-coating for the film deposition. Spray coating is only rarely applied so far [167, 168] and one cannot expect that routes developed for spin coating can be copied step-by-step to spray coating used for film deposition. For example, Ray *et al*. dissolved titanyl 2,4-pentanedionate directly in ethanol and sprayed such ink to get titania films [167].

Thus, the focus of the present investigation is on optimizing the spray process as well as the route of the sol-gel solution used as ink in the spray coating. As known from investigations using spin coating, a calcination step follows the film deposition to ensure the crystallinity of the resulting metal oxide film after spray coating. During the calcination, the polymer matrix is removed and the crystalline metal oxide can be formed. To probe the inner film structures down to the nanometer scale, grazing incidence small-angle X-ray scattering (GISAXS) is used [101, 169], which complements the observations of the surface morphology obtained from real space imaging techniques, such as optical microscopy and scanning electron microscopy (SEM). The inner film morphology is essential for potential applications such as photovoltaic devices because it strongly influences the charge carrier separation. Therefore, the characterization of the film's inner morphology is an important piece of information for potential applications [170, 171].

5.1 Tuning of titania films thickness

Concerning the control of film thickness, spray coating shows a great advantage compared to spin coating, especially for the film prepared via the sol-gel route. For spin coating, there are several ways to control the film thickness, such as rotation speed, viscosity of the solution, and gas atmosphere in the spin-coating chamber. In this study, the sol-gel solution consists of the following independent components: copolymer, precursor, good solvent and bad solvent. For example, the higher concentration of the copolymer can increase the film thickness. However, the amount of rest compositions also need to be modified, where excessive experiments are needed to achieve the same morphology as a thinner film. Another way to control the film thickness is multiple spin-coating. After the multiple spin-coatings, thickness shows a linear relation to spin-coating steps. Due to using the same solution for each spin-coating step, the fresh solution will dissolve the pre-deposited films, which shows a limitation in the control of film thickness. Meanwhile, the film roughness also increases with more spin-coating steps.

In this section, all the samples are prepared in the sol-gel route with a weight ratio of 0.94 (1,4-dioxane) : 0.05 (TTIP) : 0.01 (HCl). The spray parameters are set at N_2 carrier gas pressure of 2 bar, a nozzle-to-sample distance of 16 cm, a heating temperature of 80 °C, and a spray speed of 127.16 µL. For each spray cycle, it consists of 10 s spray time and 10 s heating interval. The samples are deposited by 1, 3, 5, 10, 15 cycles, respectively. The film thickness of all samples is probed by Dektak before calcination. Five different surface positions are chosen randomly in each sample during Dektak measurement. Figure 5.1 shows that the film thickness increases linearly with increasing spray cycles, ranging from 250 nm to 6.5 µm. A large deviation of average thickness is observed in more spray cycles. It indicates the film has less homogeneity when more spray cycles are applied. The data is fitted by a linear fit function, which is shown by the red line in Figure 5.1.

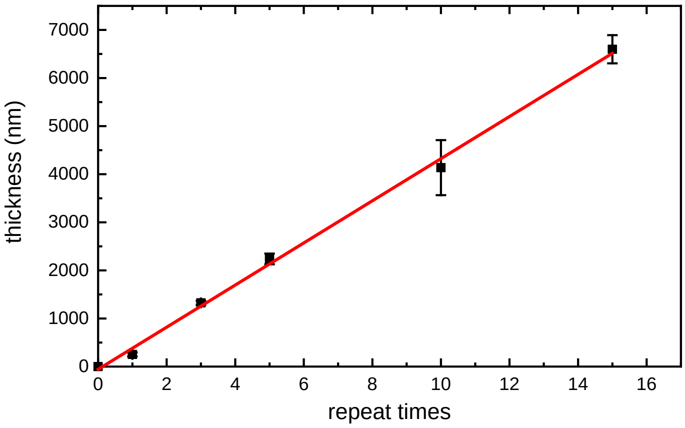

Figure 5.1 *Plot of the thickness of hybrid sol-gel prepared films spray cycles of 1, 3, 5 10 and 15. A linear fit is applied to the data, shown by red line with a slope of (438 ± 10) nm.*

The optical microscope images of hybrid titania films, which are prepared by 1, 3, 5 10 and 15 spray cycles, are shown in Figure 5.2. Cracks are observed after 3 spray cycles. Furthermore, the films prepared by more than 3 spray cycles exhibit a less homogeneous surface than the film prepared by 1 spray cycle. The top surface of the spayed films shows isolate island in Figure 5.2 d and e, which means the smoothness of the hybrid titania film severely decreases with more spray cycles. It is typically attributed to different surface tensions on the droplet and air interface during the evaporation step.

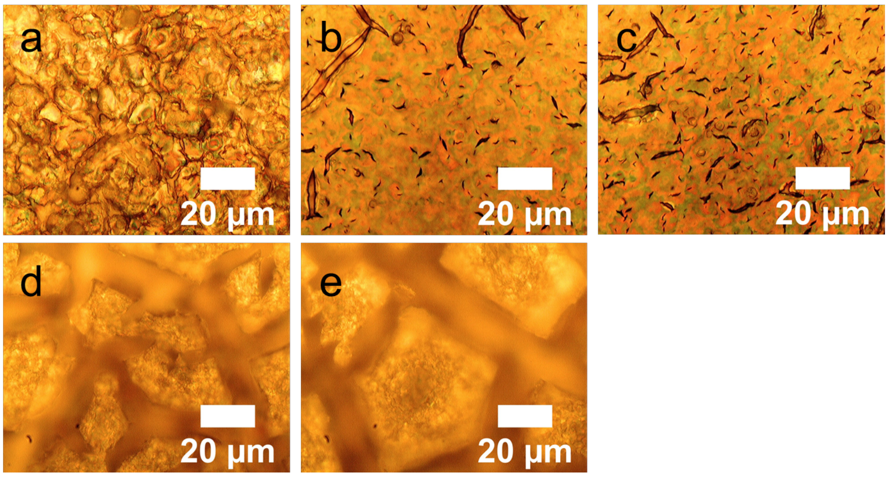

Figure 5.2 *Optical microscopy images of hybrid titania films prepared by a) 1, b) 3, c) 5, d) 10 and e) 15 spray cycles.*

5.2 Tuning of titania films via sol-gel recipe

The diblock copolymer polystyrene-*block*-polyethylene oxide (PS-*b*-PEO) is used as obtained from Polymer Source Inc., Canada, with a polydispersity index M_w/M_n = 1.07. Its number average molecular weight is 30 kg/mol with a PS fraction of f_{PS} = 0.77. After dissolving PS-b-PEO in 1,4-dioxane (≥99,5%, extra pure, Carl Roth), the appropriate amount of hydrochloric acid (37% HCl, extra pure, Carl Roth) and 97% titanium(IV) isopropoxide (97% TTIP, Sigma-Aldrich) are added dropwise. All the solvents and acid are used as received without further purification. A diblock copolymer concentration of 16.09 mg/ml is fixed in the present study. In addition, the weight fraction of HCl is fixed at 0.01 to form the core-shell micelles with a PS core in the solution. In the first set of experiments, the weight fraction of TTIP is varied from 0.04 to 0.07 in steps of 0.01. In the second set of experiments related to the variation of the spray parameters, the weight ratios of TTIP and HCl are kept at weight fractions of 0.07 and 0.01, respectively.

The sol-gel synthesis starts with dissolving the template polymer PS-*b*-PEO in 1,4-dioxane. The total amount of 1,4-dioxane is put into three vials: one for dissolving the block copolymer, one with HCl and one with TTIP. The solution with the block copolymer is stirred with a magnetic stirrer for 30 min, then filters with a 0.2 μm pore size polytetrafluoroethylene (PTFE, Carl Roth GmbH) filter. Afterwards, the TTIP and HCl solutions are injected drop-wise into the solution using the microfluidic method [139]. The injection speed is kept constant at 0.25 ml/min. The final solution is stirred for 45 min before use.

Both, glass (microscope slides, Carl Roth) and silicon substrates (Si 100, n-type, Silchem), are cut into 2 x 2 cm^2 pieces, followed by immersion in an acid bath (200 mL of H_2SO_4 95%, 70 mL of H_2O_2 30%, and 130 mL of deionized water (DI)) at 80 °C for 15 min [172]. 95% H_2SO_4 and 30% H_2O_2 are purchased from Carl Roth. Afterwards, the substrates are rinsed strongly with DI water and dried by N_2 gas.

In the experiments regarding the variation of the composition of the sprayed sol-gel solution, fixed spray conditions are used. The spray nozzle is a Grafo T3 with a nozzle size of 0.4 mm. The spray time is set to 10 s, the spraying speed to 127 mL/s, the temperature of the substrate heating plate to 50 °C, the pressure of the carrier gas to 2 bar and the sample to nozzle distance to 16 cm. Through extensive experiments, these conditions are determined to be favorable for the desired morphology evolution. The samples are then placed into a furnace, heated to 450°C with a heating rate of 2 °C/min, and then kept at 450 °C for 30 min.

5.2.1 Morphology

The diblock copolymer PS-*b*-PEO acts as a structure-directing agent in the sol-gel process. Thus, we focus on a rather classical model system for diblock copolymer assisted sol-gel nanostructure generation, which is primarily used for spin coating and solution casting experiments so far.[117, 173, 174] To establish the ink for spray coating, 1,4-dioxane is used as a solvent for PS-*b*-PEO, which can dissolve both blocks. HCl is used as a selective solvent, since the PEO block is hydrophilic and PS block is hydrophobic. Moreover, the acid prevents TTIP precipitation by charging the originally formed nuclei of $Ti(OH)_4$. After adding a small amount of HCl, micelles are formed to minimize the interfacial energy. TTIP is mainly incorporated into the PEO domains with coordination bonds. Furthermore, the Ti-O bonds are linked with adjacent titania species to form the continuous structure [117]. In the sol-gel preparation step, the microfluidic method is used, which has been established by Rawolle et. al. [19, 139, 175]. Hybrid films are obtained after spray coating of these inks. During the calcination step, the block copolymer component is removed and the amorphous titania parts crystallize. Afterwards, bicontinuous network morphologies of the titania films are formed. The thickness of the films is (152 ± 10) nm after calcination as measured by Dektak (DektakXT Stylus Profiler, Bruker).

The film morphology is probed with GISAXS [101, 169]. The corresponding sketch is shown in Figure 5.3. The scattered intensities are probed with exit angle α_f in q_z direction and with out-of-plane angle ψ in q_y direction. Thus, GISAXS probes mainly lateral structures and correlations along the surface normal. Because the chosen incident angle α_i of 0.48° is well above the critical angle of titania (α_c = 0.28°), the X-ray beam can fully penetrate the entire titania films and inner film structures are accessible. Instead of analyzing the full 2D intensity distribution, selected line cuts can be used in the data analysis. To get the lateral structure information, a horizontal line cut from the 2D GISAXS data is performed at the Yoneda peak position of the titania material, which resembles the maximum of the diffuse scattering in q_z direction.

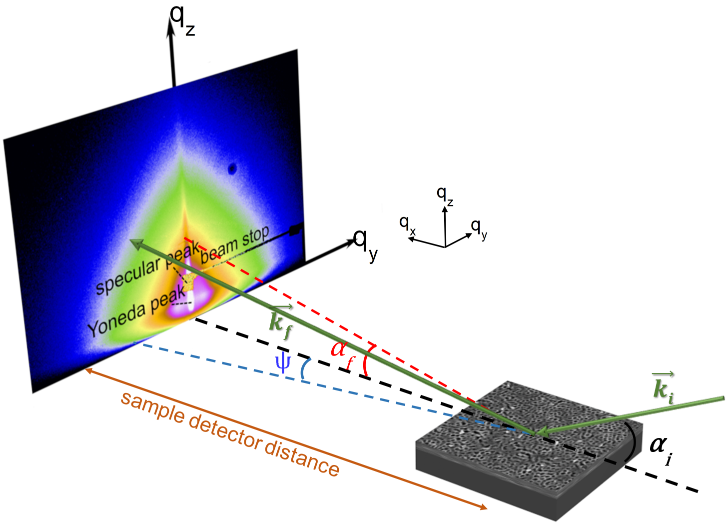

Figure 5.3 *Schematic view of the GISAXS geometry. The incident angle of incoming X-ray beam (denoted ki) is ai and the exit angle of scattered X-ray beam (denoted kf) in the scattering plane is af. A beam stop is placed at the specular beam position. The Yoneda peak is located at the position of the critical angle of the film. Adapted by permission from reference[38]: Springer, Journal of Sol-Gel Science and Technology, COPYRIGHT 2017.*

Such horizontal line cuts are further analyzed based on the first order perturbation theory named distorted wave Born approximation (DWBA) [100]. We make use of the effective interface approximation (EIA) and the local monodisperse approximation (LMA) [19, 101] to model our scattering data. A cylindrical shape is used to model the shape of scattering objects. The horizontal line cuts of the 2D GISAXS data together with their corresponding fits are seen in Figure 5.4a for samples with different TTIP weight fractions.

As indicated in Figure 5.4a, a broad shoulder-like peak in the intensity shifts towards larger q_y values with increasing the TTIP content, corresponding to decreasing object sizes. In more detail, the cylinder radii decrease from 11.5 to 5.7 nm (see Figure 5.4b). The shoulders originate from the structure factor of lateral porous structures in the titania films, which is used to calculate the pore size and the edge-to-edge distance (the distance between two neighboring pores, which also means the size of bicontinuous titania skeletal structure.) (Figure 5.4c) [176]. The form factor presents the pore size, and edge-to-edge distance is calculated by:

$$\text{edge-to-edge distance} = \text{structure factor} - \text{form factor}$$

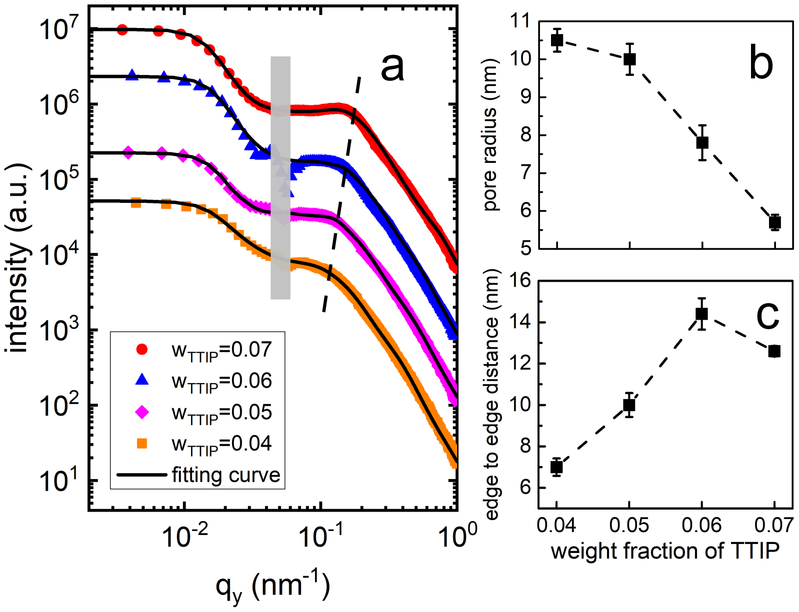

Figure 5.4 *a) Horizontal line cuts of the 2D GISAXS data (points) taken at the critical angle of* TiO_2 *and fits (lines) for calcined titania samples with different TTIP weight fraction (*W_{TTIP}*). The dashed line indicates the trend of the prominent shoulder position. The curves are shifted along the y-axis for clarity. The position of the beamstop edge is shown with the gray rectangle. b) Pore radii extracted from the fits and c) edge-to-edge distances determined as a function of the TTIP weight fraction. Adapted by permission from reference*[38]*: Springer, Journal of Sol-Gel Science and Technology, COPYRIGHT 2017.*

As the weight ratio of TTIP increases, the surface free energy of the PS blocks is increased, which induces a decrease in pore size. A maximum width of the bicontinuous titania network is found at a TTIP weight fraction of 0.06 with a wide structure size distribution. It shows that the Ti-O- covalent bonds attach the PEO domains partially at a low weight ratio of TTIP in the sol-gel solution to form the large spacing between the titania structures. The error bars in Figure 5.4b and Figure 5.4c indicate the distribution widths of the determined structure information. A small distribution width, such as for the sample with a TTIP weight fraction of 0.07 indicates that the foam-like structure has a relatively higher uniformity as compared to the other compositions.

In addition to the GISAXS analysis, the mesoporous structures are also visualized by scanning electron microscopy (SEM). Rather isolated titania nanostructures are observed in Figure 5.5a, which originates from the low weight fraction of TTIP of 0.04 used for this sample. With increasing amount of TTIP, the titania surface structures become bicontinuous, and the pore size decreases slightly. The successive addition of TTIP gradually decreases the pore size, indicating that the TTIP forms an increasing number of Ti-O- bonds in the hydrophilic PEO domains. At a TTIP weight fraction of 0.07, the foam-like structure becomes more ordered.

Although with SEM only the surface structures are seen, we find an agreement with the quantitative results from the GISAXS analysis.

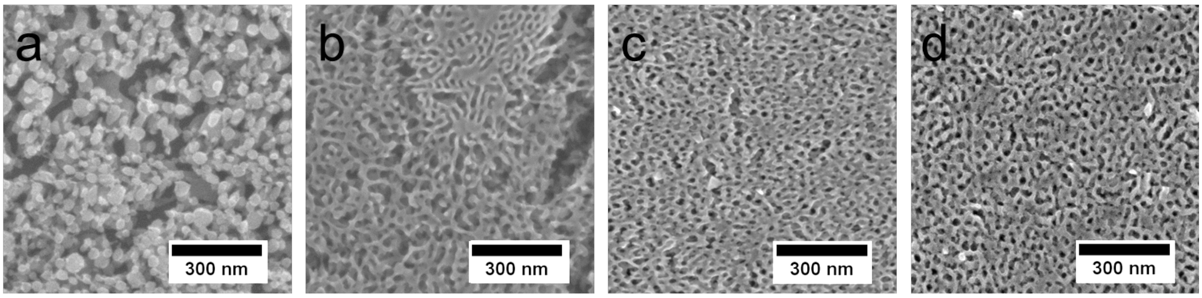

Figure 5.5 *SEM images of the titania films after calcination with different weight fractions of TTIP: a) 0.04, b) 0.05, c) 0.06, d) 0.07. Adapted by permission from reference[38]: Springer, Journal of Sol-Gel Science and Technology, COPYRIGHT 2017.*

In an earlier study, Cheng *et al*. reported that the porous titania structure is affected by the TTIP content in the case when spin coating is used for film deposition [117]. In the present study, we observe the same phenomenon for spray coated titania films. Hence, within the limits of the solution viscosity of the ink allowing for spray deposition, tuning of pore sizes can be performed by varying the amount of TTIP. Moreover, it confirms that the sol-gel process is an attractive approach to get a porous titania structure in the nanoscale by self-assembly, and is also attractive for using spray coating as a deposition technique.

5.2.2 Optoelectrical properties

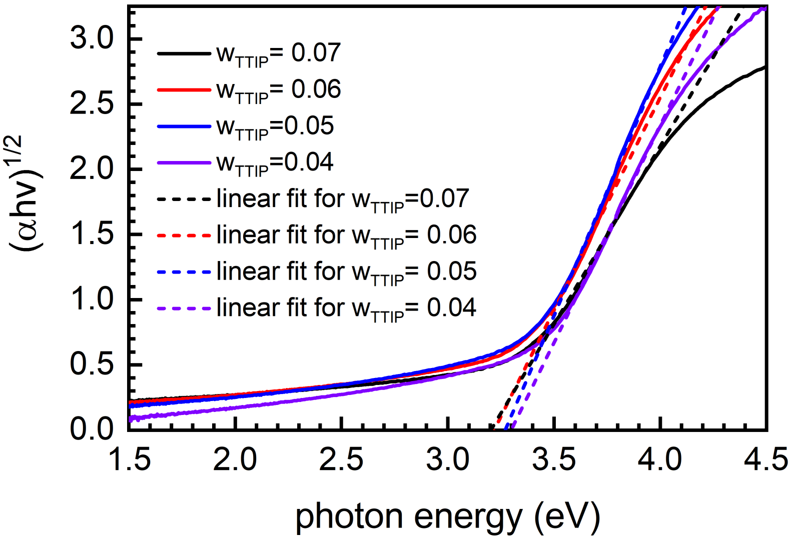

Figure 5.6 *Indirect optical band gap transitions* $(\alpha hv)^{1/2}$ *as a function of photon energy of anatase titania films obtained by changing the TTIP weight ratio in the sol-gel solution. Adapted by permission from reference[38]: Springer, Journal of Sol-Gel Science and Technology, COPYRIGHT 2017.*

The band gap of crystalline titania films is characterized by UV-Vis analysis. The indirect band gap of anatase phase is determined by Tauc's equation:

$$\alpha h\nu = A(h\nu - E_g)^n \qquad (5.1)$$

Where A is a constant, hv is the photon energy, E_g is the allowed band gap, and n=2 for the indirect transition. At ambient conditions, anatase and rutile are the two main crystalline phases of titania, with band energies of 3.2 eV and 3.0 eV, respectively. Figure 5.6 shows the data by plotting $(\alpha h\nu)^{1/2}$ as a function of the photon energy with a linear fit in the absorption edge. Although all samples have a comparable absorbance, decreasing of the TTIP content causes a change in the bandgap from 3.2 eV to 3.3 eV. Jian *et al*. reported the bandgap of facets satisfy the order (101) ≈ (010) > (001),[177] which indicates that the (101) facet is more favorable for low TTIP content samples.

5.3 Tuning of titania films via spray parameters

Considering the above results, the spray protocol has been varied for the most promising composition with a TTIP weight fraction of 0.07. The selected spray steps are 1 × 10 s, 2 × 5 s and 5 × 2 s. Whereas the total spray time is fixed to 10 s (which ensures that the same amount of material is deposited), different spray protocols have been realized by varying the spray steps used for the deposition, while keeping all other spray parameters fixed (nozzle to sample distance, sample temperature, spray speed, carrier gas pressure). These different spray protocols are shown in Figure 5.7. In between two subsequent spray steps, an interval wait time of 10 s is chosen. After spray deposition, all samples are calcined at 450 °C for 30 minutes.

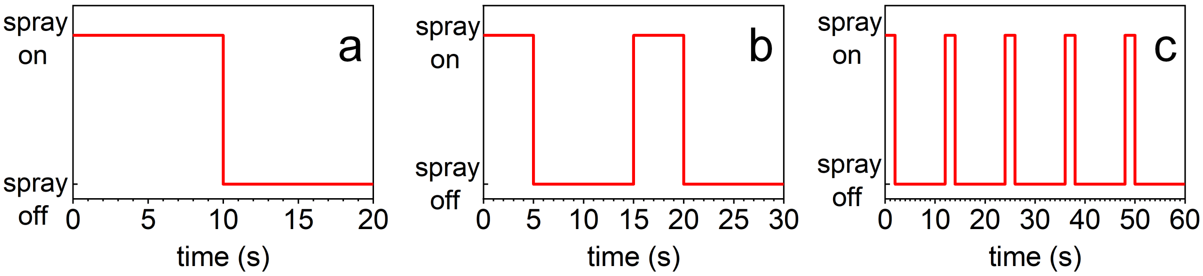

Figure 5.7 *The spray protocols used in this study: a) Continuous spray for 10 s followed by 10 s wait time at 50 °C (abbreviated as 1 x 10 s), b) 2 spray steps with 5 s spray deposition followed by 10 s wait time at 50 °C (abbreviated as 2 x 5 s), and c) 5 spray steps with 2 s spray deposition followed by 10 s wait time at 50 °C (abbreviated as 5 x 2 s). Adapted by permission from reference[38]: Springer, Journal of Sol-Gel Science and Technology, COPYRIGHT 2017.*

5.3.1 Morphology

Figure 5.8a shows the horizontal line cuts of the 2D GISAXS data exhibit similarities with those from the composition investigation of Figure 5.4a. Marked shoulders in the intensities are seen in these line cuts. The data analysis uses the same model as described above. The pore radius increases slightly if the spray time is divided into several steps (Figure 5.8b), and the titania structure size decreases with increasing number of spray steps (Figure 5.8c). Thus, different spray times can tune the titania network structure size and also pore size slightly in the nano-scale, but have a minor effect as compared to the composition for the tested conditions.

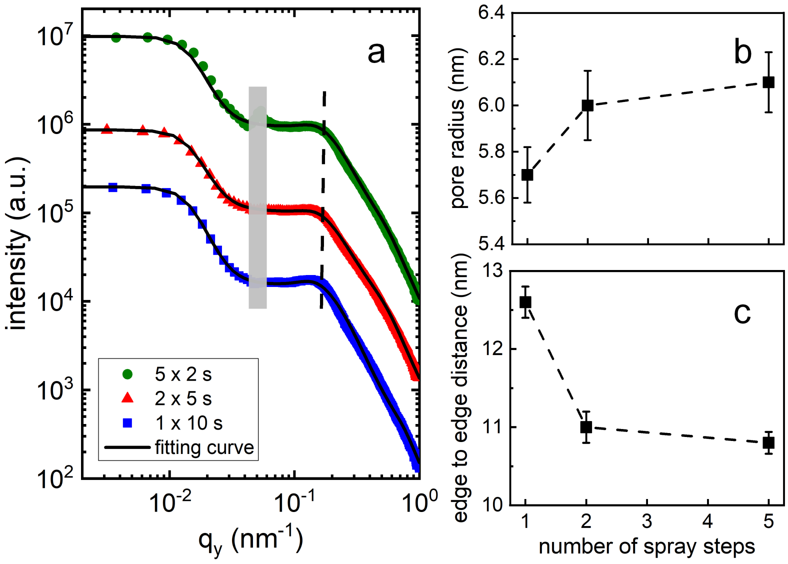

Figure 5.8 *a) Horizontal line cuts of the 2D GISAXS data (points) taken at the critical angle of* TiO_2 *and fits (lines) for calcined titania samples. The dashed line indicates the trend of the prominent shoulder position. The curves are shifted along the y-axis for clarity. The position of the beamstop edge is shown with the gray rectangle. b) Pore radii extracted from the fits and c) edge-to-edge distances determined as a function of the number of spray steps used during the spray deposition. Adapted by permission from reference[38]: Springer, Journal of Sol-Gel Science and Technology, COPYRIGHT 2017.*

SEM images of the titania films produced with different spray protocols are shown in Figure 5.9 for films after calcination. The surface morphology of the films is shown in high magnification in Figure 5.9a to Figure 5.9c, and in low magnification in Figure 5.9d for comparison. With a higher number of spray steps, the pore structure is affected and the pore size increases. On a larger scale, the film uniformity is enhanced with more spray steps (Figure 5.9d), which is very important for applications. During the interval wait time introduced between two subsequent spray steps, the organic solvents evaporate from the films. Moreover, a smaller amount of the sol-gel solution arrives on the surface during one spray step. As a consequence, the more time the sprayed films have to achieve a dry state, the more spray steps are implemented in the spray protocol. Therefore, the most ordered structures have been obtained with the spray protocol divided into 5 spray steps. Further increases in the number of spray steps, e.g. to 10 spray steps, is not successful due to the spray nozzle clogging when the operating spray time is only 1s.

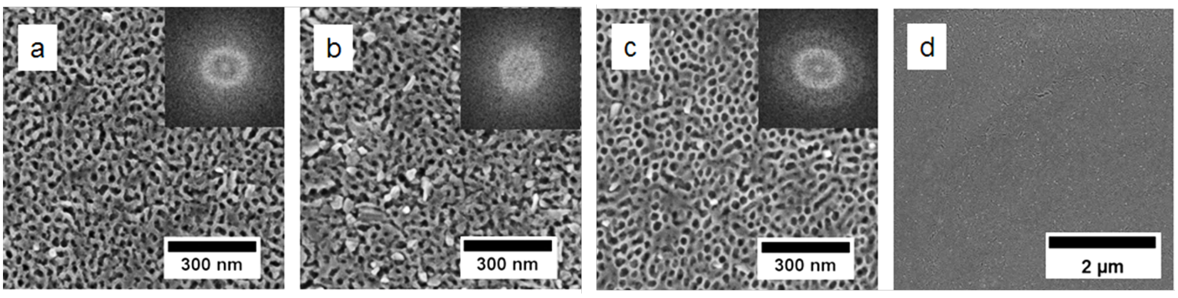

Figure 5.9 *SEM images and FFT patterns (insets) of the titania films after calcination deposited with different spray procedures. a) 1 ´ 10 s, b) 2 ´ 5 s, c) 5 ´ 2 s, d) 5 ´ 2 s image at a low magnification. Adapted by permission from reference[38]: Springer, Journal of Sol-Gel Science and Technology, COPYRIGHT 2017.*

5.3.2 Optical characterization

In order to evaluate the optical bandgap of titania films, which are prepared by different spray protocols, Tauc's equation is used for the calculation of the optical bandgap after UV-vis measurement. A constant bandgap of 3.2 eV is seen in the study with varying spray protocols, which shows that the bandgap is independent of the applied spray protocols concerning the number of spray steps. Thus, the number of spray steps can be used to tune the film homogeneity.

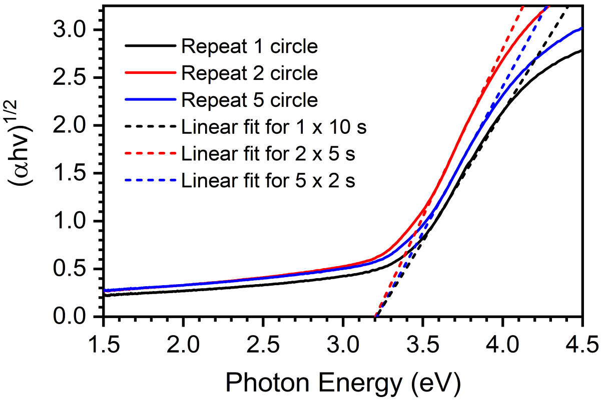

Figure 5.10 *Indirect optical band gap transitions (αhv)1/2 as a function of photon energy of anatase titania films obtained by changing the spray protocols. Adapted by permission from reference[38]: Springer, Journal of Sol-Gel Science and Technology, COPYRIGHT 2017.*

5.4 Crystallinity tuning via calcination temperature

Titania has three major crystal phases: rutile, anatase and brookite. Rutile and anatase are the thermodynamically stable bulk phases. Additionally, the anatase phase shows a higher photocatalytic activity, making it widely used in photocatalytic and photovoltaic applications. In general, the crystallinity depends on the calcination temperature and the resulting crystal size is important for photovoltaic applications [178].

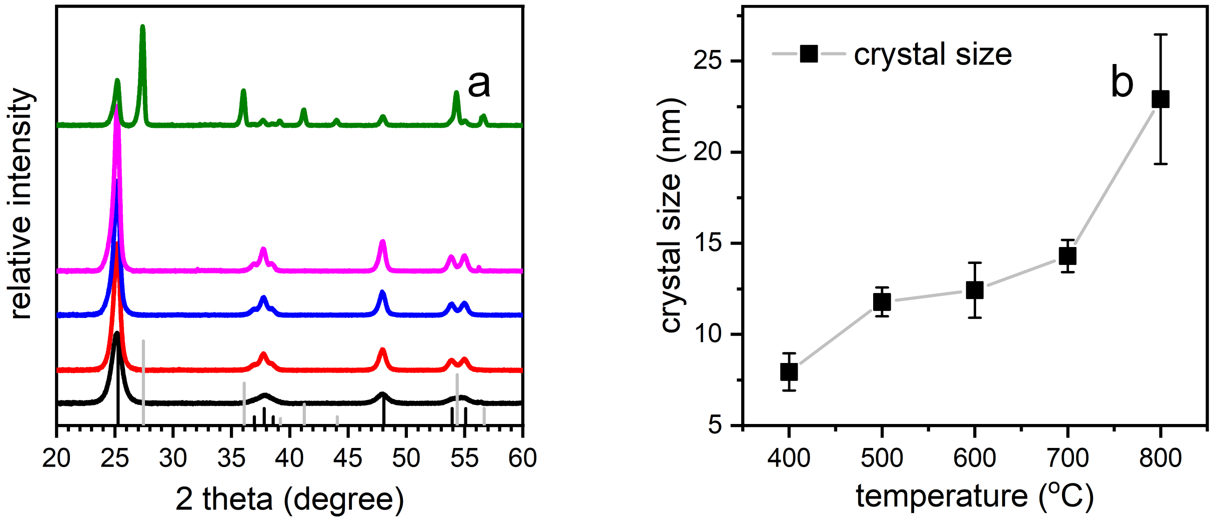

***Figure 5.11** a) X-ray diffraction (XRD) data of titania films after calcination at 400 °C, 500 °C, 600 °C, 700 °C and 800 °C (from bottom to top), shown together with JCPDS #21-1272 reference data for anatase phase (black lines) and JCPDS #21-1276 reference data for rutile phase (gray lines); b) calculated crystallite size for different sintering temperatures. Adapted by permission from reference[38]: Springer, Journal of Sol-Gel Science and Technology, COPYRIGHT 2017*

Hybrid samples are fabricated from the block copolymer assisted sol-gel route via spray coating as detailed in the experimental section. Different sintering temperatures are investigated with respect to their impact on the crystal phase of the titania films. Figure 5.11a shows the X-ray diffraction patterns of titania films after calcination at 400 °C, 500 °C, 600 °C, 700 °C and 800 °C. The anatase phase is identified from 400 °C to 700 °C, whereas the rutile phase is found for sintering at 800 °C, based on the reference data (anatase: JCPDS #21-1272, black lines in the bottom of Figure 5.11a; rutile: JCPDS #21-1276, grey lines in the bottom of Figure 5.11a from International Center for Diffraction Data (ICDD)). Thus, the spray coated titania films based on the block copolymer assisted sol-gel route behave very similar to porous titania films prepared via other recipes. Figure 5.11b shows the crystallite sizes, calculated by using the Scherer equation for the (101) anatase peaks and for the (110) rutile peaks. From 400 °C to 700 °C, the crystallite size increases from 7.9 nm to 14.3 nm. However, a further increase of the sintering temperature to 800 °C induces the anatase to rutile phase transition, and the crystallite size increases dramatically to 22.9 nm. As a consequence, for the given preparation conditions, calcination at 700 °C can give the best conditions needed for e.g. photovoltaic applications.

5.5 Summary

By combining the block copolymer assisted sol-gel process with a spray deposition, controllable foam-like structures of the titania network in the nanoscale are formed, which is crucial for potential photovoltaic applications. We find that the pore size of the titania networks can be well controlled via different compositions of the sol-gel solution whereas different spray parameters have only a minor influence. Thus, spray deposition is a robust technique for future industrial applications as the detailed spray parameters are less important for controlling the morphology of the titania network. Moreover, UV/Vis measurements also show that the bandgap is increasing with reducing TTIP content, due to (101) facets becoming more favorable for low TTIP content samples. Therefore, the composition of the sprayed sol is of fundamental importance. From the XRD data of different sintering temperatures, we found that the titania anatase phase changed to the rutile phase at 800 °C. While anatase titania films with the largest crystallites are obtained at 700 °C, well crystallized films are already achievable at 450 °C, thus allowing for more efficient energy consumption during film fabrication.

6. MORPHOLOGY EVOLUTION DURING SPRAY COATING

Parts of this chapter have been published in the article: Macroscale and nanoscale morphology evolution during in situ spray coating of titania films for perovskite solar cells[39] (B. Su, H. A. Caller-Guzman, V. Körstgens, Y. Rui, Y. Yao, N. Saxena, G. Santoro, S. V. Roth, P. Müller-Buschbaum, ACS Appl. Mater. Interfaces, 9, 43724-43732, 2017, DOI: 10.1021/acsami.7b14850)

Mesoporous titania is a low-cost and widely used material for photovoltaic applications. To enable a large-scale fabrication and a controllable pore size, we combine a block copolymer assisted sol-gel route with spray coating to fabricate titania films, in which the block copolymer polystyrene-block-polyethylene oxide (PS-*b*-PEO) is used as a structure-directing template.

Organic-inorganic perovskite solar cells (PSCs) have shown a tremendous power conversion efficiency improvement from 3.8% to 21.1% to date.[10, 179] PSCs are commonly classified into two categories depending on whether the electron transfer layer is exhibiting a planar[9] or a mesoporous structure[141]. In general, the latter includes a mesoscopic metal oxide scaffold (pore size of 2-50 nm) functioning as the electron transfer layer, for example, mesoporous titanium dioxide. The perovskite crystals form depending on the used titania scaffold, and its structural parameters, such as for example thickness,[180, 181] porosity and order.[182] They are crucial for the photovoltaic performance, since for example, the randomly oriented pores result in defects at the grain boundaries of the perovskite crystallites.[8, 94, 183] Additionally, titania scaffolds can retard charge recombination and elongate the optical light path in the devices.[14, 92] It is well established that the growth and the formation of the perovskite films are governed by the precursor composition of the perovskite material and the substrate or the morphology of the electron transfer layer.[184-186] Furthermore, the well-defined crystallinity, the feature size of perovskites, and the charge mobility also benefit from the presence of ordered porous structures.[8, 12, 90, 93-95]

A promising approach of obtaining ordered mesoporous titania films with pores on the nanometer scale is based on templating with block copolymers.[19] Such wet chemical process was used e.g. by Wiesner and coworkers to control the characteristic length scale of metal oxides that have mesoporous structures. This control was done by using a diblock copolymer.[115]

Diblock copolymers comprise two chemically distinct segments linked by a covalent bond, which are incompatible with each other. The functional inorganic precursor selectively interacts with one of the polymer blocks via hydrogen bonding. Driven by entropic and enthalpic interactions between both blocks, the desired morphologies of the metal oxide are formed inside the diblock copolymer. Nanostructured hybrid films are achieved through a microphase separation process.[117, 163, 187-189] Via microphase separation, diblock copolymers can form characteristic morphologies, such as spheres, cylinders, lamellae and bicontinuous structures. The hybrid films are exposed to further treatments, for example, a high temperature calcination to remove the polymer matrix and achieve the final metal oxide films.[190] Therefore, diblock copolymers offer a vast potential for designing nanostructured electron transport layers for photovoltaic applications.[191, 192] For dye-sensitized solar cells (DSSCs), Grätzel and coworkers demonstrated that regularly distributed anatase nanocrystals enhance power conversion efficiencies by 50% as compared to randomly distributed titania films.[193] Therefore, mesoporous titania structures with a controllable pore size synthesized via sol-gel processes are widely used in DSSCs, solid-state DSSCs and PSCs to enhance the power conversion efficiency.[194-198]

So far, most studies used the spin-coating for thin film preparation including the deposition of the mesoporous titania films. However, with respect to large-scale applications spin coating is only of limited value. Alternative deposition techniques such as spray coating are more promising.[199] Reports making use of spray coating for preparing mesoporous titania films are rather rare. In chapter 5, it is demonstrated that spray coating can be applied in large-scale production, because the pore size of the spray-coated titania films can be fully controlled by the composition of the sprayed solution whereas the spray parameters have only a minor influence. For example, the weight fraction of the titanium precursor such as titanium tetraisopropoxide (TTIP) controls the pore size. Moreover, it was reported that (101) facets were more favorable for low TTIP content, causing a shift of the bandgap of the titania films.[38]

To gain deeper insights, it is crucial to further study the hybrid titania films' structure evolution during the spray process. Such fundamental understanding of the spray deposition process will enable full control, which is of utmost importance for photovoltaics. The titania film morphology needs to be understood on the macro- and micro-scale, since spray coating can produce also macroscopic structures besides the microscopic structures introduced by the block copolymer assisted sol-gel chemistry.

In this chapter, firstly, the structural evolution of the titania films is probed with *in situ* grazing incidence small-angle X-ray scattering (GISAXS) during the spray process. It shows that changes of the PS domain size are not only dependent on micellization, but also on solvent evaporation during the spray coating. Secondly, the kinetics and thermodynamics of the spray depositions processes are simulated on a macro-scale. The results are I line with the large-scale morphology of the spray-coated films obtained in practice. Eventually, 3D perovskite solar cells are fabricated, which proves that spray-coated titania films are more suitable for the solar device compared with comical titania paste. Based on spray-coated titania layers, devices with power conversion efficiencies of 10% are manufactured, which shows a strong improvement as compared to PSCs based on a commercial TiO_2 paste (efficiencies of 8.3% for the same device architecture).

6.1 *In situ* spray coating GISAXS measurement

In this section, the samples are spin-coated with compact titania films firstly on the acid-cleaned silicon substrates following Hua's description (in the section referring to DSSCs fabrication). [135] For the mesoporous titania film, the weight ratio of 1,4-dioxane, TTIP, and HCl in the sol-gel solution is 0.92, 0.07 and 0.01, respectively. Spray deposition has evolved as a very versatile approach to achieve nanostructured films. However, the kinetics of spray process are not easy to monitor. A semi-automatized spray set up is custom-designed for this present research.

6.1.1 Morphology evolution during spray coating

The *in situ* GISAXS technique is combined with a spray setup. The *in situ* scattering experiments are performed at a synchrotron to enable a subsecond time resolution, providing excellent statistics for the scattering signals (Figure 6.1). By modeling line cuts from the 2D GISAXS data, the key structural parameters such as film density, structure sizes and spacing of adjacent particles can be extracted at the micro-scale.[145, 200] Figure 6.2(a) shows a schematic view of the used GISAXS geometry. The sample is placed on the heating stage at 50 ℃ to achieve dry films. The spray ink consists of 94 wt% 1,4-dioxane, 1 wt% HCl, 5 wt% TTIP, and 16.1 mg/ml PS-*b*-PEO. The PS-*b*-PEO acts as structure guide, while TTIP acts as the titania precursor. HCl is a selective solvent, which induces the microphase separation due to the increased surface energy of the PS blocks. A spray shot of 2 s is triggered by a software-controlled spray gun, using N_2 gas as the carrier gas under 1 bar. The first spray shot is started at time *t*=0 s. The spray protocol is pictured in Figure 6.2(b).

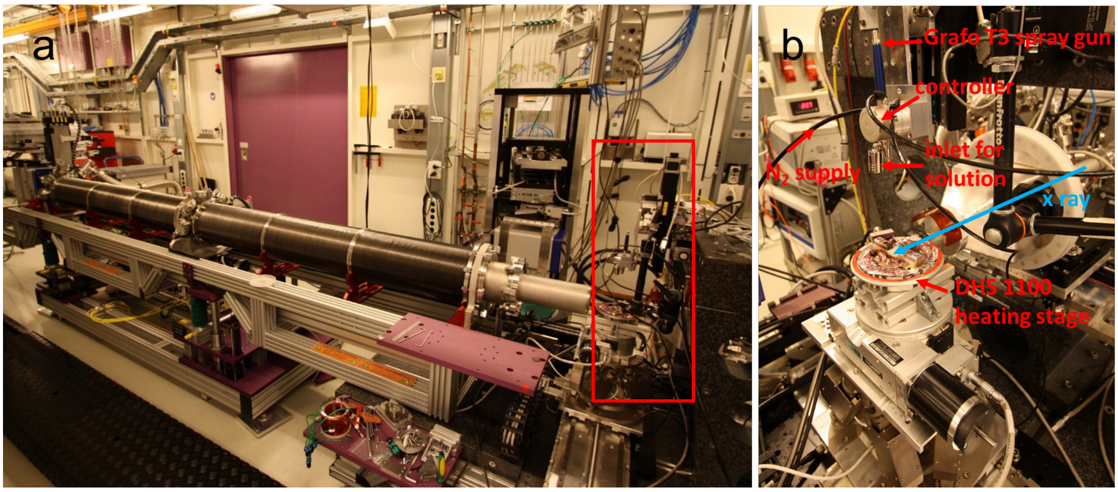

Figure 6.1 *Photographs of a) in situ spray GISAXS setup at beamline P03, and b) the zoom-in of the red rectangle, where the x-ray is represented in blue color.*

The *in situ* GISAXS spray experiment is carried out at the PETRAIII P03 MiNaXS beamline at DESY with a photon energy of 13 keV, which corresponds to the wavelength of 0.957 Å. The Grafo T3 spray setup (Harder & Steenbeck), with a nozzle size of 0.4 mm, is implemented in combination with GISAXS. The sample-to-nozzle distance is 16 cm and the pressure of the N_2 carrier gas is 1 bar. A Pilatus 300k is used as a 2D detector to record the scattering data probed at an incidence angle of 0.245°, which is chosen to be well above the critical angles of PS (0.09°), PEO (0.10°) and TiO_2 (0.18°). To avoid beam damage of the hybrid films, the sample stage is scanned along the y-direction (perpendicular to the X-ray beam direction) during the experiment, over a length of 6 mm in 0.05 mm steps. The data acquisition time for each frame is 0.1 s. 2 s of spray are followed by a 5 s wait time in one so-called spray cycle. In total 10 of such spray cycles are done.

The experiment is carried out under ambient conditions on the substrate, which has deposited compact titania film on top. The sample, which is perpendicular to the spray nozzle, is placed on a heating stage (DHS 1100, Anton Paar) at a constant temperature of 50 °C (Figure 6.1b). The heating stage can operate between the temperature range of 25 °C and 1100°C, and is calibrated using a blank silicon wafer before the experiment. An exposure time of 0.1 s is chosen for each frame, which is to ensure a high time resolution in the *in situ* GISAXS experiments. Figure 6.3 shows the selected 2D GISAXS data for different times of the spray deposition, starting from -10 s and followed by 8 s, 26 s, 44 s, 62 s and 74 s. The most prominent feature, which is around $q_y = 0.21\ \mathrm{nm}^{-1}$, emerges after first spray shot. Also, the increase of the scattering intensity is observed with a longer spray time, which corresponds to an increase in film thickness as more material is deposited on the film. These modulations from the 2D GISAXS data give a basic understanding of film formation during the spray process with a qualitative nature.

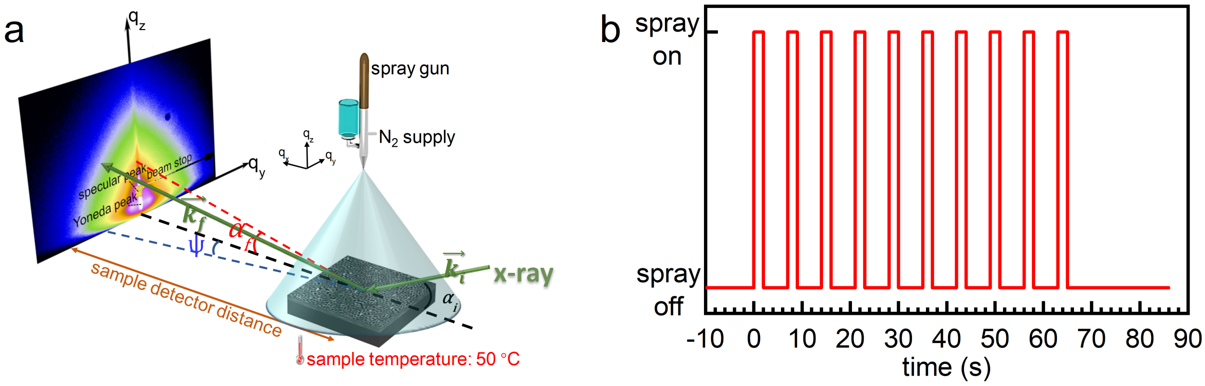

Figure 6.2 *a) Schematic view of the GISAXS geometry. The incident angle of incoming X-ray beam (denoted k_i) is a_i and the exit angle of scattered x-ray beam (denoted k_f) in the scattering plane is a_f. A beam stop is placed at the specular beam position. The Yoneda peak is located at the position of the critical angle of the film. b) The spray protocol used in the in situ GISAXS experiment, which consists of spray cycles of 2 s of spray followed by 5 s of heating at 50 °C. The cycle is repeated 10 times in the in situ GISAXS measurement, which ended after a long wait time after 86 s. Adapted with permission from reference.[39] Copyright 2017 American Chemical Society.*

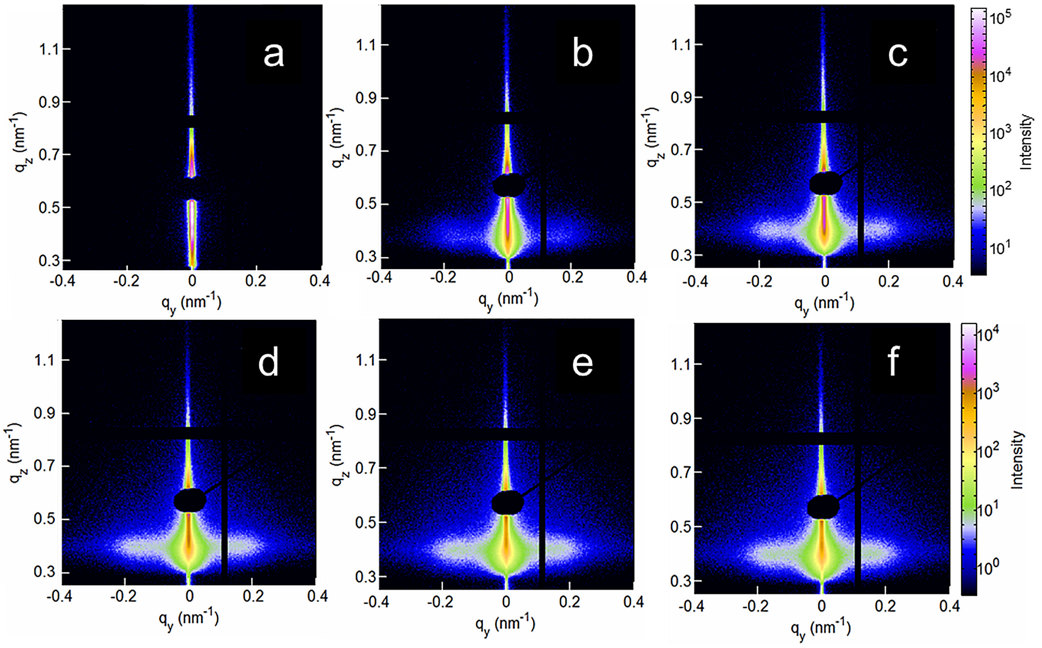

Figure 6.3 *Selected 2D GISAXS data from in situ spray experiment, each measured for 0.1 s at a) -10 s, b) 8 s, c) 26 s, d) 44 s, e) 62 s and f) 74 s. Adapted with permission from reference.[39] Copyright 2017 American Chemical Society.*

Lateral structure information is extracted from horizontal line cuts of the 2D GISAXS data taken at the Yoneda peak of PS-*b*-PEO. These horizontal line cuts at different times of the spray deposition are mapped in Figure 6.4. In the initial 10 s (before the first spray step, which means before t= 0 s), only the compact titania layer is observed. When the spray deposition starts (t=0 s), the intensity distribution in the horizontal direction changes immediately. A peak of around $q_y = 0.21$ nm^{-1} (emphasized by the red solid rectangle in Figure 6.4a appears. This peak is attributed to the distances between neighboring PS domains since micelles with PS cores form in a PEO matrix containing TTIP. Meanwhile, we have good contrast between PEO containing TTIP (d= 3.09 × 10^{-05}) and PS (d= 9.13 × 10^{-06}). Its intensity increases with spray time, indicating that a hybrid film with such features increases in thickness on the substrate. This micro-scale structure is formed by a solidification process. Figure 6.4b shows selected horizontal line cuts. The bottom-most curve in Figure 6.4b resembles the structure information of the initial compact titania layer before the spray deposition. The peak is seen at around q_y = 0.21 nm^{-1} from the second curve on, i.e. with the onset of the spray deposition. It slightly shifts to larger q_y values, corresponding to a decrease in the PS domain distance.

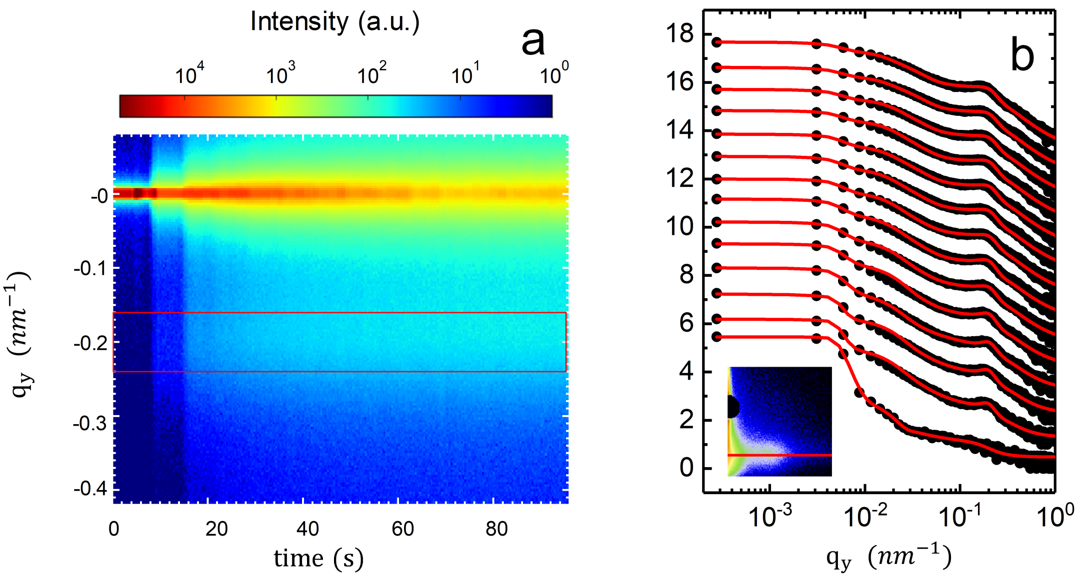

Figure 6.4 *a) Mapping of horizontal line cuts from the in situ 2D GISAXS data cut at q_z = 0.35 nm^{-1}. The first 10 s probe the bare compact titania layer before the spray deposition. Spray deposition starts at t= 0 s. The red rectangle emphasizes that the peak around q_y = 0.21 nm^{-1} becomes more pronounced with time. b) Selected horizontal line cuts (solid dots) and fits (red solid lines). The curves are shifted along the y-axis for clarity. The plots from the bottom to the top show data measured at -8 s, 2 s, 8 s, 14 s, 20 s, 26 s, 32 s, 38 s, 44 s, 50 s, 56 s, 62 s, 68 s, and 86 s, respectively. Each curve is obtained by integrating 10 frames. The insect in Figure 6.4b shows the horizontal line cut position indicated by the red line. Adapted with permission from reference.*[39] *Copyright 2017 American Chemical Society.*

We integrate 10 frames of 0.1 s exposure time to have horizontal line cuts with good statistics for the modeling of the data. The horizontal line cuts are analyzed within the framework of the distorted-wave Born approximation (DWBA), using the effective interface approximation (EIA) and the local monodisperse approximation (LMA).[19, 100, 101] Form factor (domain radius) and structure factor (domain center-to-center distance) are extracted from the analysis. We assume a cylindrical shape of the domains. To describe the data two populations of objects with different distances are required. The small objects are PS domains in the PEO matrix with TTIP and the large objects are resembling clusters. The resulting parameters are plotted in Figure 6.5.

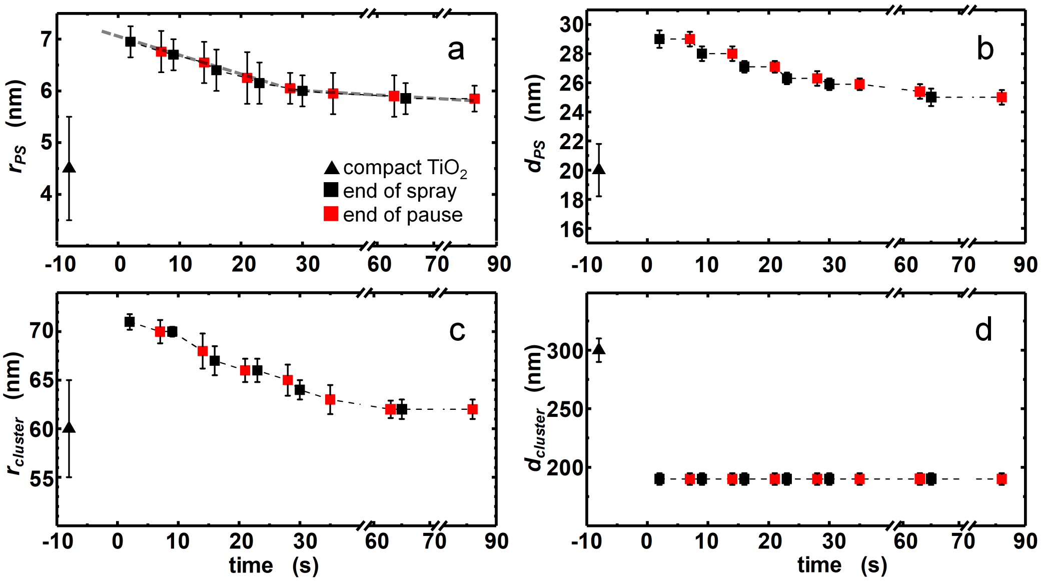

Figure 6.5 *Structure information determined from fitting the in situ GISAXS line cuts: a) Radii of PS domains* r_{PS}*, b) center-to-center distances of PS domains* d_{PS}*, c) radii of clusters* $r_{cluster}$ *and d) center-to-center distance clusters* $d_{cluster}$*. The structure before spray deposition is shown with a black triangle. The data during the spray steps are shown with black squares and data during the drying steps are shown with red squares. Adapted with permission from reference.*[39] *Copyright 2018 American Chemical Society.*

During the spray process, the morphology of the hybrid films is mainly governed by micelle deposition and solvent evaporation. The initial form factor (radius of PS domains r_{PS}) and structure factor (distance between PS domains d_{PS}) are 6.9 nm and 29 nm, respectively. During the first waiting period, residual solvent from the deposited film evaporates and the PS domain size decreases (r_{PS} = 6.6 nm). The structure factor remains unchanged during solvent evaporation. In the second spray step, the structure factor of PS domains decreases, because sol-gel droplets dissolve the already deposited film and stack, which compacts the film and ensures bicontinuous titania films are obtained after calcination. Also, the form factor of the PS domains decreases slightly. For each spray cycle, the same trend is observed. PS domain distances decrease with each spraying step (to 25 nm after 65 s) and the PS domain sizes continuously decrease (to 5.9 nm after 65 s). After 10 spay cycles, the characteristic structures stay constant within the error bars. For the larger size clusters, only the form factor decreases during the spray cycles, whereas the structure factor of the clusters stays constant throughout the whole spray coating process. After the last spray step, the form factor and structure factor are also constant, which implies that the morphology of the dry film has equilibrated. The final dry films exhibit more compact structures as compared with the initial deposited wet material. For the selected conditions, it needs 10 spray cycles to achieve equilibrated structures.

6.1.2 Molding of film growth during spray coating

Based on the information retrieved from the GISAXS data analysis, Figure 6.6 shows a sketch of the film formation on the micro-scale during the applied spray protocol. The macro-scale spray droplets contain a micro-scale substructure caused by the micellar type of ink used for the spray coating. Morphology transition towards equilibrium and evaporation of the solvent 1,4-dioxane cause a shrinkage of the micro-scale structure related to the individual packing of the PS core and PEO/TTIP shell micelles. The domain distance keeps constant during the interval heating step, due to the shrinking of the 2D domains caused by solvent evaporation. Thus, the temporal evolution of the micro-scale morphology in the hybrid films is different from previous reports on ZnO nanostructure formation out of zinc acetate dehydrate sprayed out of N, Ndimethylformamide. Sarkar *et al*. observed with *in situ* GISAXS studies that an initially deposited large ZnO cluster structure is filled with small ZnO nanoparticles until a homogenous film is achieved.[145]

The dark grey layer represents the compact titania films, and the light blue and dark blue cylinders present the PS domains with and without 1,4-dioxane, respectively. PEO block with amorphous titania material is shown with green color in Figure 6.6. After the first spray step, the fresh droplets with 1,4-dioxane are deposited on the sample, which have a larger structure size (Figure 6.6a). The structure size is decreased after the heating interval time, due to the evaporation of the solvent (Figure 6.6b). When the concentration of diblock copolymer reaches the point of over-saturation, the condensation process occurs spontaneously. Amorphous titania particles form the Ti-O bond with adjacent titania particles, which ensure continuous titania network structures are obtained. After the second spray step, the fresh droplets partially dissolve the pre-deposited material, and the films become more compact (Figure 6.6c). Finally, the dry hybrid films are achieved after the spray deposition process. The changes of structure features imply the films transfer from non-equilibrium state to an equilibrium state.

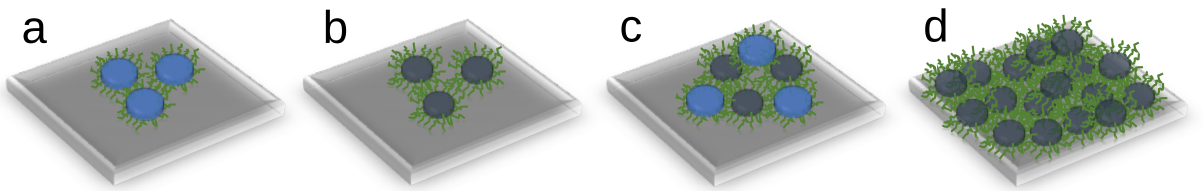

Figure 6.6 *Illustration of film evolution during spray deposition. The compact titania films are shown in dark grey color. Light and dark blue cylinders represent PS domains with and without solvent. Green cylinder represents PEO domains with titania nanoparticles. Characteristic stages are shown for a) the first 2 s spray cycle, b) the following 5 s heating interval, c) the second 2 s spray cycle and d) the whole spray protocol. Adapted with permission from reference.[39] Copyright 2017 American Chemical Society.*

6.1.3 Morphology and crystallinity after calcination

To investigate the final film morphology in real space after finishing the spray protocol, SEM measurements are performed. Figure 6.7a shows a representative SEM image of the sample after spray coating. The PS domains, which have low conductivity as compared to the PEO domains containing titania nanoparticles, appear as dark areas in the SEM image. The average PS domain size is (5.8 ± 0.2) nm, which is in agreement with the GISAXS results. Large-sized structures called clusters in the GISAXS data fitting are highlighted with white circles in Figure 6.7a and resemble clusters in the micro-scale structure, due to the local arrangement of the hybrid films during solvent evaporation.

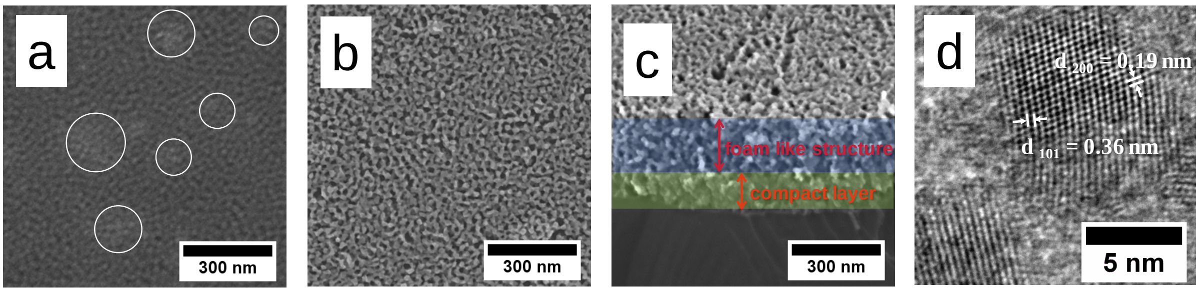

Figure 6.7 *SEM and TEM images of the titania films after the in situ spray experiment: a) Top view SEM of the hybrid film as deposited, b) top view SEM of the film after calcination, c) cross-section SEM of the film after calcination and d) TEM image of films after calcination. Adapted with permission from reference.[39] Copyright 2017 American Chemical Society.*

To remove the diblock copolymer and crystalize the titania in the films, the sample is calcined at 450 °C for 30 minutes with a ramp of 2 °C/min (Figure 6.7b). A porous and bicontinuous titania nanostructure is formed. From cross-sectional SEM images (Figure 6.7c) the average film thicknesses of the mesoporous and compact titania layers are extracted, which are 185 nm and 96 nm, respectively. Furthermore, the pore sizes are equal in the vertical direction, which shows a difference compared to porous titania films prepared by block copolymer assisted sol-gel method via spin coating. Titania films deposited with spin coating have a more ordered surface part as compared to the mesoporous structure inside the films.[188] The spray coated titania films (tetragonal; space group, 141/*amd*; *a*=3.785, *b*=3.785, *c*=9.514) are also investigated by transmission electron microscopy (TEM) to have a higher real space resolution (Figure 6.7d). TEM data analysis indicates that the spray coated films are polycrystalline and two kinds of crystalline planes of anatase titania phase, i.e. (101) and (200), are observed. The sample is measured by XRD with a Bruker D8 diffractometer at an X-ray wavelength of 1.54 Å (copper anode at 40 KV). The software, named DIFFRAC.SUITE, was used to collect the data. A 2θ range of 20° to 60° was scanned with a step size of 0.01° using a counting time of 0.1 s. The reference peaks for TiO_2 were taken from the Joint Committee on Powder Diffraction Standards (JCPDS). It shows the theoretical and measured peak positions match well. (Figure 6.8).

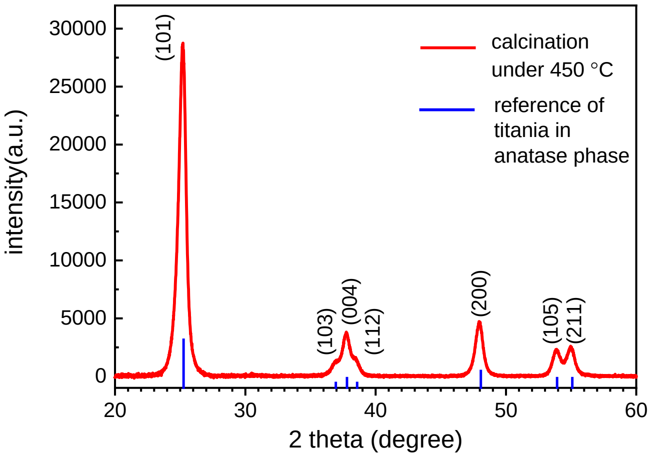

Figure 6.8 *X-ray Diffraction (XRD) data of titania films after calcination at 450 °C. Data are shown together with PDF#21-1272 reference taken from the Joint Committee on Powder Diffraction Standards (JCPDS). Adapted with permission from reference.*[39] *Copyright 2017 American Chemical Society.*

6.2 Simulation of spray process

To study the evolution of the morphology on the macro-scale, a simulation of the spray coating process is performed. We investigate the evolution of the hybrid film morphology during spray coating, based on the theory provided by Filipovic and coworkers.[201] This work is done with my master student Herbert A. Caller-Guzman.

6.2.1 Mathematic model

Figure 6.9 shows the sketch of the spray set up, which consists of an airbrush, a heating plate and a solution container. The control parameters are the nozzle-to-sample distance, the spray angle, and the temperature of the heating stage. Due to the difference of the pressure inside and outside of the spray gun, the spray solution is splitting into small droplets with the carrier gas by the nozzle. Then the droplets emerge from the nozzle orifice with different sizes and velocities, which mainly depend on the nozzle type (nozzle size and geometry), spray angle, pressure of the carrier gas, spray speed, and spray solution. The simulation is programmed with the parameters used in the *in situ* spray experiment, such as 16 cm of nozzle-to-substrate distance, 50 °C of the heating stage, 1 bar of N_2 carrier gas pressure, and 10º for the spray angle with respect to the vertical direction.

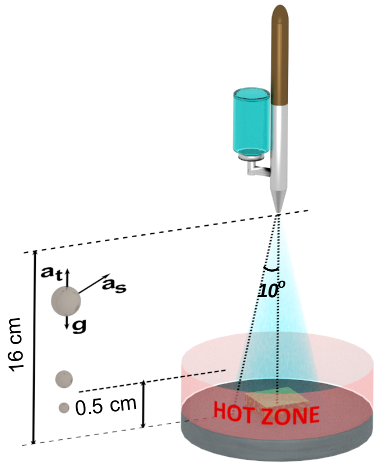

Figure 6.9 *Schematic drawing of the simulation conditions of the spray coating process. Adapted with permission from reference.*[39] *Copyright 2017 American Chemical Society.*

The total number of the simulated droplet is 9×10^6, which is determined by the total volume of sprayed solution. We assume the speed of the droplets inside the nozzle is $V_{in} = 0$, and the pressure outside the nozzle (P_{out}) is rather small compared to the applied nitrogen carrier gas pressure, so we set $P_{out} = 0$. From Bernoulli's equation, the absolute value of the speed of initial droplets (V_{out}) is expressed as

$$V_{out} = \sqrt{\frac{2P_{in}}{r_d}} \tag{6.1}$$

It is easy to control the initial particle size by changing the nozzle size and pressure of the carrier gas. However, the pressure of the carrier gas significantly influences the drying behavior of droplets. The initial size distribution of the droplets can be expressed with

$$r=\left[\frac{1}{\varepsilon\left(r_{\max}^{-\frac{1}{3}}-r_{\min}^{-\frac{1}{3}}\right)+r_{\min}^{-\frac{1}{3}}}\right]^{3} \tag{6.2}$$

where the minimum initial droplet size $r_{\min}$ = 25 µm, the maximum size $r_{\max}$ = 28 µm and ε is a random number in the range of 0 to 1. [202-204] Gravity is the vertical driving force for the droplet transport towards the substrate, which is taken into account in the whole process.

The aerodynamic force (Stokes force) is a retarding force, which has a lift component and a component parallel to the substrate, which is caused by the friction between the droplet and the air molecules. According to Strokes law, we can calculate the strength of this force as a function of the droplet velocity and size, which is expressed as

$$F_s=6\pi\eta_a r\cdot(v_d-v_a)\left(1+\frac{3}{8}\mathrm{R}_e\right) \tag{6.3}$$

where *r* is the radius of the droplet, the air viscosity is η_a = 1.86 × 10^{-5} Pa·s , ν_d and ν_a are the velocities of the droplet and air, respectively. $\mathrm{R_e}$ is the Reynolds number, and for spherical particles, it is expressed as

$$R_e=\frac{2r\left(v_d-v_a\right)\rho_a}{\eta_a} \tag{6.4}$$

where ρ_a = 1.1839 *kg/m*^{3} is the air density. The acceleration due to this force for spherical liquid particles is given by

$$a_s=\frac{9\eta_a}{2\rho r^2}v_d \tag{6.5}$$

The thermophoretic force is also taken into account, which results in the creation of the thermal gradient by the heated substrate. The thermophoretic force is written as

$$F_T=\frac{3\pi\eta_a^2 r}{\rho_a}\times\frac{3k_a}{2k_a^2+k_d}\times\frac{\nabla T_a}{T_a} \tag{6.6}$$

where k_a = 0.024 W/m·K and k_d = 0.159 W/m·K are the thermal conductivities of the air and the droplet, respectively. This equation is only valid in the case that the radius of the droplet is larger than the mean free path of the air molecules. The acceleration of the droplet due to thermophoretic force is given by

$$a_T = \frac{27\eta_a^2 \kappa_a \nabla T_a}{4\rho_a \rho_d T\left(2\kappa_a^2 + \kappa_d\right) r^2} \tag{6.7}$$

and ρ_d = 1.03 × 103 kg/m^3 is the density of the droplet, which corresponds to 1,4-dioxane. These three forces, mentioned above, are taken into account in our model. We divide the regime from the nozzle to the sample stage into three zones, where different forces affect the simulation results. The temperature in zone I, starting from 0 cm to 5 cm with respect to the nozzle position, is 25 °C, and gravity and stoke force are inferred in this regime. The temperature changes linearly from 25 °C to 50 °C in zone II, starting from 5 cm to 15.5 cm, and gravity, Stokes force and thermophoretic force are included. Gravity and Stokes force are involved in zone III, starting from 15.5 cm to 16 cm, and the temperature is kept constant at 50 °C. To track the trajectory of the droplet, the motion along the vertical direction is needed, and is given by

$$\frac{d^2H}{dt^2} = g - a_T + s\frac{dH}{dt} \tag{6.8}$$

where $H(t)$ is the vertical displacement, g is gravity acceleration and s is a constant related to the Stokes force $a_s = s\nu_d(t)$. The vertical velocity can be calculated from equation 6.8, which is expressed as

$$v_H\left(t\right) = \frac{g - a_T}{s} + \left(v_{H_0} - \frac{g - a_T}{s}\right)e^{-st} \tag{6.9}$$

Another replacement is the radial component, and the motion equation is given by

$$\frac{d^2R}{dt^2} = s\frac{dR}{dt} \tag{6.10}$$

and the radial velocity and radial displacement are given by

$$v_R\left(t\right) = v_{R_0}e^{-st} \tag{6.11}$$

$$R\left(t\right) = \frac{v_{R_0}}{s}\left(1 - e^{-st}\right) \tag{6.12}$$

where ν_{R_0} is the radial component of the initial velocity ν_0. The size of a droplet decreases due to the evaporation in zone II and III, where the evaporation mainly affects the small radius of the droplet. It is given by

$$\frac{dr}{dt} = -\frac{MD}{r\rho_d R_G T_s} \cdot \Delta p \left(1 + 0.276 R_e^{\frac{1}{2}} S_c^{\frac{1}{3}}\right) \tag{6.13}$$

$$R_e = \frac{2\rho_a v r}{\eta_a} \tag{6.14}$$

$$S_c = \frac{\eta_a}{\rho_a D} \tag{6.15}$$

$$D = \frac{RT_s}{N_A} \times \frac{1}{6\pi\eta_a r} \tag{6.16}$$

$$\Delta p = 67 \times (T - T_a) \tag{6.17}$$

where M is the molecular weight of the solvent, T_s is the temperature of the substrate, and D is the diffusion coefficient given by the Stokes-Einstein relation. Δp is the pressure difference between the vapor pressure near the droplet and ambient pressure. T is the temperature which depends on the position and T_a is the environment temperature. R_G is the gas constant.

6.2.2 Comparison of simulation data with optical images

The motion equations are coupled to the diffusion equation to obtain the evolution of the droplet size, using a finite difference scheme to solve the motion equations. In this method, we use small time step of 5×10^{-7} s to solve the equation. The size of the droplet in the simulation is influenced by the hot zone regime (more details are shown in supplementary information). Figure 6.10 shows the simulation results compared with optical microscopy images taken for spray coated films. A characteristic patchy film surface is found, which originates from the superposition of individual droplets during the spray coating. In images from the simulation, we set a transparency of 0.3 for each droplet, to show the otherwise obscured structure of droplets. The color intensity provides information about the height of the layered film. The darker the color, the more overlap of droplets at that position in the simulation. In the simulated images, the size distribution matches very well with the observations of the optical microscopy images. On the macro scale, the spray-coated film is almost uniform over the entire surface. Zooming-in, the individual droplets become visible.

The characteristic droplet structure of the spray coated hybrid film results from a layer-by-layer deposition. After the first spray deposition step, the initial droplets partially cover the substrate in a dry state due to the applied parameters (spray parameters and substrate heating). Fresh droplets arriving on the sample during the following spray cycles dissolve the pre-deposited film due to the residual solvent in these droplets. In the hybrid film, the polymer network with its precursor loading rearranges due to the solvent-induced mobility. During the wait time between two subsequent spray steps, the solvent evaporates and the film arrests. After several spray cycles, a fully covered substrate can be obtained due to the random deposition of the droplets.

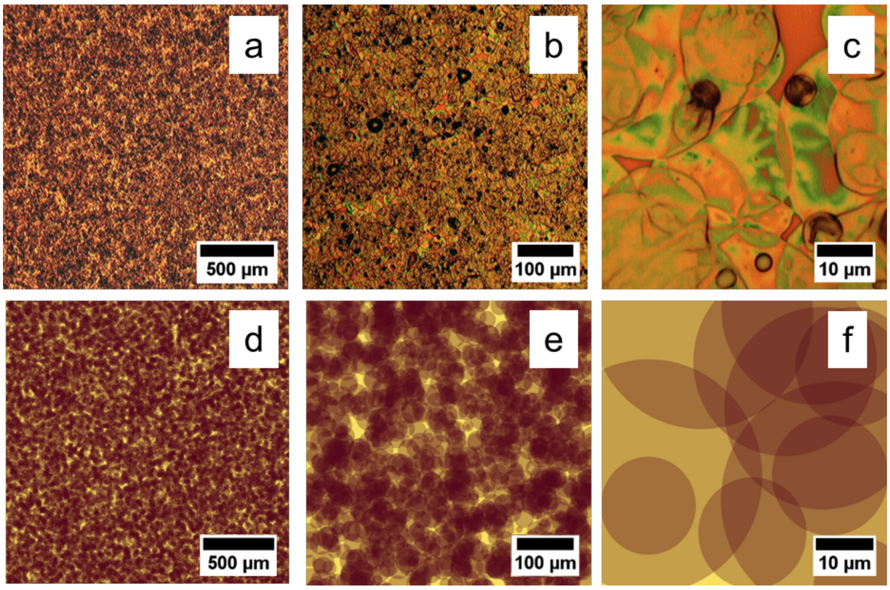

Figure 6.10 *a-c) Optical microscopy images of the films after spray coating taken with different magnifications. d-f) Simulated structures of same scales shown, as explained in the text. Adapted with permission from reference.*[39] *Copyright 2017 American Chemical Society.*

Concerning application in solar cells, the randomly distributed round shape textures introduced by the spray coating process can enhance the light scattering properties, due to an increase of the optical path length of the active material. In literature, a light scattering layer of TiO_2 with a thickness of a few micrometer was successfully applied in DSSCs.[29, 31] However, such thick layer would not be suitable for the architecture of thin film PSCs. Therefore, alternative approaches were found, for example, a moth-eye TiO_2 layer, for which the optical absorption is significantly enhanced at the interface between the TiO_2 layer and the perovskite layer.[205] In our study, an alternative route arises from the macroscale spray morphology, which is simply installed due to the used deposition method without the need of additional fabrication steps.

6.3 Perovskite solar cell based on meso-titania

Fluorine-doped tin oxide(FTO) glass substrates were etched with zinc powder and hydrochloric acid in the desired pattern. Then, the substrates were cleaned by Alconox solution, ethanol, acetone and 2-propanol under sonication, respectively. After 10 min of plasma treatment, a compact titania layer was dynamically spin-coated on the FTO substrate.[138] The mesoporous titania films were prepared under the same conditions as the one from the *in situ* spray GISAXS experiment. For comparison, the commercial titania paste (Dyesol 18NRT) was diluted in ethanol with the weight ratio of 2:7 to achieve the same thickness of sprayed samples. They were spin coated on the precleaned FTO substrates with 5000 rpm for 30 s. Subsequently, the substrates were dried at 125 °C for 15 min. Both sprayed and spin-coated samples were calcined at 450°C for 30 min.

The PbI_2 was dissolved in DMF (1 M) for 1 hour under 100°C. MAI was dissolved in 2-propanol with a concentration of 40 mg/ml for 1 hour at 70°C. After filtration with a 0.45 µm filter, the solution was cooled down to room temperature. The PbI_2 solution was spin coated at 3000 rpm for 30 s and afterwards kept at room temperature for 10 min. Next, the MAI solution was spin coated at 3000 rpm for 20 s. The substrates were annealed at 100°C for 1 hour in a nitrogen-filled glove box.

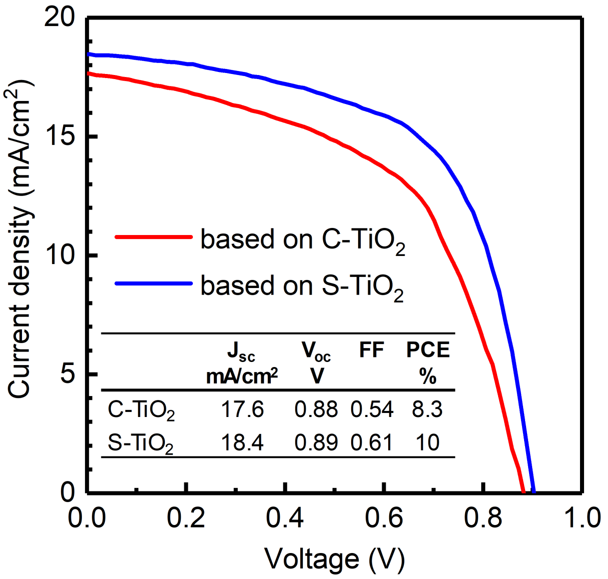

	J_{sc} mA/cm^2	V_{oc} V	FF	PCE %
C-TiO_2	17.6	0.88	0.54	8.3
S-TiO_2	18.4	0.89	0.61	10

Figure 6.11 *Current density vs. voltage curve under AM1.5G illumination of the PSC. C-TiO_2 and S-TiO_2 represent the IV curves of PSC based on commercial TiO_2 paste and sol-gel prepared TiO_2, respectively. Adapted with permission from reference.[39] Copyright 2017 American Chemical Society.*

After the perovskite annealing, a spiro-OMeTAD solution (70 mM in chlorobenzene) was spin coated at 4000 rpm for 30 s. The spiro-OMeTAD solution was doped with FK209 Co(III) TFSI salt and TBP, and the molar ratios of additives for spiro-OMeTAD were: 0.5, 0.03 and 3.3 for Li-TFSI, FK209 and TBP respectively. The gold counter electrode was deposited by thermal deposition under high vacuum.

Solar cells based on a spray-coated titania film via sol-gel route obtain PCE of about 10%, which is slightly larger than the PCE values reached for the devices based on the commercial titania paste (8.3%). It should be noted that the PSCs are not optimized towards reaching champion efficiencies. However, the improvement in PCE appears promising for further studies. It demonstrates that the morphology of the titania films influences the performance of the PSCs. We assume that the increase in PCE originates from the optical absorption, crystal orientation and crystal size of the perovskite.

6.4 Summary

We investigated the structure evolution of hybrid films during spray coating on the macro- and on the micro-scale. In the macro-scale, the applied spray coating protocol results in overlapping droplets. Our simulation of the spray process on the macro-scale matches well with the optical microscopy images. It implies that the present hot zone regime not only dries the films, but also influences the droplet size. The micro-scale structure is revealed with *in situ* GISAXS. Micelle deposition, evaporation of the solvent and transformation of the morphology towards equilibrium influence the structure features on the micro-scale. An equal distribution of the pore size in the vertical film direction is seen. Thus, the micro-scale morphology of sprayed films differs from the morphology reported for spin-coated films, which demonstrates the strong impact of the selected film deposition method on the final micro-scale morphology. The PSC results reinforce the importance of controlling the pore size of the TiO_2 layer, and motivate the use of the spray coating method to deposit mesoporous titania films with a controllable pore size.

7. SUPERSTRUCTURING OF TITANIA FILMS

Nanopatterning has received tremendous attention as a means of improving the PCE of photovoltaics and energy storage devices.[21, 206, 207] It provides a renowned method for constructing photonic nanostructures. In low-cost photovoltaics, such as mesoscopic sensitized solar cells and perovskite solar cells, charge collection and light harvesting properties of nano metal oxide (typically titania) play an important role in the determination of the overall PCE.[20, 22, 208] Structural engineering of titania films provides a brand new way to enhance the charge collection and optical absorption, such as incorporation of light scattering materials,[7, 29, 209, 210] photonic crystals,[211-213] and plasmon resonance induced by metallic nano-architectures.[32, 35, 37, 214, 215]

In this thesis, the superstructure is obtained by wet imprinting and nano-imprint lithography(NIL). For wet imprinting, the stamp is applied on wet films with a certain pressure, and the structure is formed during the drying process. After removing the stamp, the superstructure remains on the film surface. It provides a simple and low-cost way to structure a film. In this method, poly(dimethylsiloxane) (PDMS) is used for the flexible polymer stamps, due to its intrinsic anti-sticking property, flexibility and low cost. A CD disk is used as a master to obtain the parallel line structure. In regards to the film preparation, solution casting, spin coating, and blade coating are suitable for the wet imprinting. In previous work, M. A. Niedermeier used wet-imprinting method to fabricate the mesoporous titania films with a hierarchical structure.[23] However, due to the use of solution casting to deposit sol-gel prepared titania films, the film thickness is hard to control and the film’s drying step normally needs 48 hours . Furthermore, the strong thickness loss is occurred during calcination step, which results the more than 50% decrease of feature height, since the presence of PS-*b*-PEO in sol-gel prepared titania films is removed during calcination. Here we applied wet-imprinting method on the blade-coated titania films, and the film thickness is well controlled during the blade-coating. The whole imprinting process only can be done in less than one hour. Thus, this method is suitable for dye-sensitized solar cells (DSSCs). DSSCs based on super-structured titania films are fabricated, and the enhanced performance is attributed to this light-trapping structure. For NIL method, concerning the hardness, only polymer-based films can be structured. Therefore, a hybrid polymer film with titania seeds is prepared by sol-gel wet chemistry method. The OrmoStamp is replicated from the Si master with a desired structure depth, which is fabricated via photolithography processes. Since the replicated stamp has a nano-scale structure and the limitation from the imprinting technique, several requirements have to be fulfilled. For example, the roughness of the film should be small, which means that only spin-coated films are suitable. During the imprinting process, vacuum, heating and high pressure (~55 bar) is applied. The structured films are characterized by atomic force microscopy (AFM) and scanning electron microscopy (SEM).

Part of this work is done with the cooperation of Robin Nagel in Prof. Dr. Paolo Lugli group (Technische Universität München, Garching).

7.1 Wet imprinting

Blade-coated titania films are used for the wet imprinting process. In this section, the fabrication routine is described first. The morphology of the titania films is characterized by SEM and AFM, respectively. DSSCs based on superstructed titania films are fabricated, and the PCE is compared to the DSSCs without superstructure.

7.1.1 Fabrication routine

Blank compact discs (Platinum 700 MB, 4M Systems SA) are used for wet the imprinting process. The disc structure consists of a bisphenol-A polycarbonate as a substrate, followed by a thin layer of a light-sensitive dye, a reflecting layer of aluminum and a sealing paint. Figure 7.1 shows an illustration of the wet imprinting process, and the stack schematic of the CD blanks is shown in the dotted rectangle in the center.

In order to obtain the pure mold out of the CD, the CD blank is cut into 4 pieces. Then the paint label and reflective layer are removed with adhesive tape (Figure 7.1b). Afterwards, the residual cyanine dye layer is removed by an ultrasonic bath of 2-propanol (Figure 7.1c). A further 2-propanol bath of 24 h is needed, which ensures the thorough removal of the dye layer. The structure on the CD disk is a trapezoidal shape with a width of 900 nm and a spacing of 600 nm. An aluminum frame is placed on top of CD mold. Then the PDMS stamps are produced by casting PDMS solution into an aluminum frame with a size of 30 x 30 mm^2 (Figure 7.1d). After annealing in a vacuum chamber at 80°C overnight, the transparent PDMS stamps are obtained.

The mesoporous titania layer is prepared by the doctor blade method. The commercial titania paste Dyesol 18NRT is used for blade coating. To achieve a thickness of 15 µm for the mesoporous titania layer, two strips of scotch tape are used during blade coating (Figure 7.1e). After blade-coating of the titania films, the samples are placed into an oven at 60 °C for 10 min. Then the PDMS stamp is placed on top of the sample with a metal block of 1 kg at 60°C for 30 min (Figure 7.1f). Finally, the PDMS stamp is peeled carefully, and the samples are calcinated at 450 °C for 30 min (Figure 7.1g).

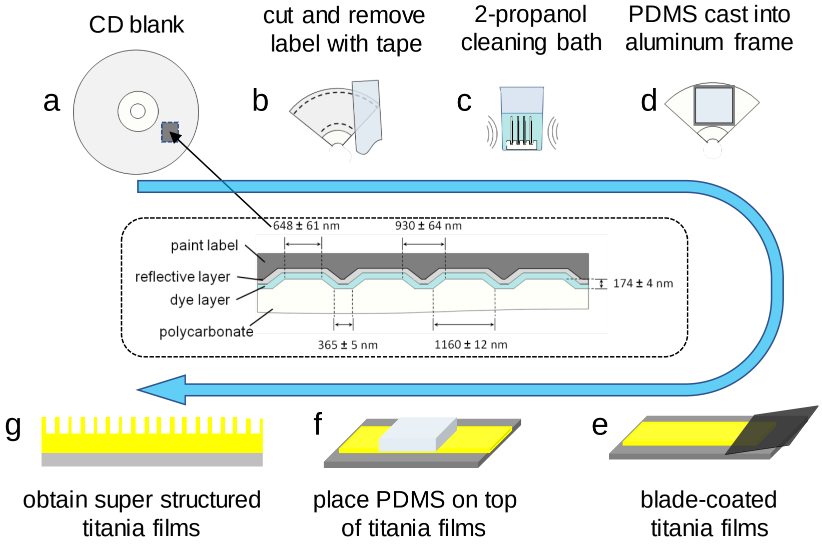

Figure 7.1 *Schematic illustration of wet imprinting routine applied to blade-coated titania films: a) blank compact disc as a structure master; b) cutting of the CD disk and removal of the label; c) removal of the dye layer by 2-propanol ultrasonic cleaning; d) casting of the PDMS mold and annealing; e) blade-coating titania films; f) embossing the titania films by PDMS mold; g) removal of the PDMS mold and obtaining the structured titania films. The dotted rectangle shows the multilayer stack of a blank compact disc.*

7.1.2 Morphology

The wet imprinted titania films are investigated by scanning electron microscopy. In Figure 7.2, a top surface of wet-imprinted titania films after calcination is shown. The bright region represents the stage structure with a width of 650 nm, and the dark region represents the channel structure with a width of 360 nm (as shown in Figure 7.2a). The feature size of the structure matches well with the structure on the CD blank, which indicates the structure is successfully transferred to the titania film via wet imprinting method. Furthermore, no cracks are observed on the titania films. Remarkably, the foam structure remains inside the periodical channel structures (as shown in Figure 7.2b). Wet imprinting provides an alternative way to fabricate the hierarchical structured titania.

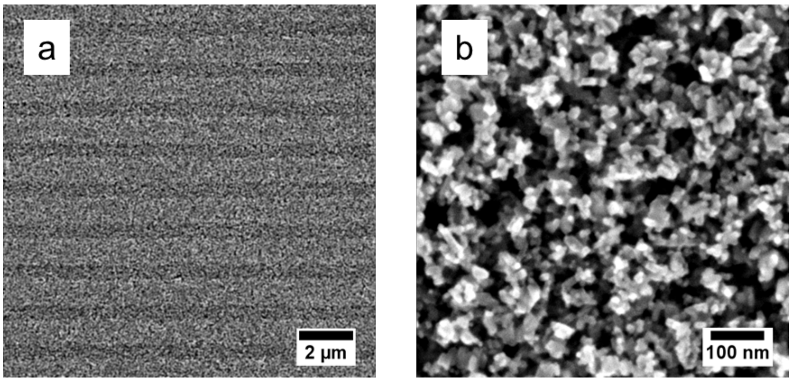

Figure 7.2 *SEM images showing the top surface of wet-imprinted titania films after calcination in a) low magnification and b) high magnification.*

In order to obtain more quantitative information from wet imprinted titania films, samples are also probed by atomic force microscope. Figure 7.3a shows topography images of wet-imprinted films. The periodic structure is visible as a prominent feature compared to SEM images. The height profile of the area, which is marked by a red rectangle in Figure 7.3a, is shown in Figure 7.3b. It reveals the stage structure with a width of 650 nm and channel structure with a width of 360 nm on average. It indicates that the lateral structure feature of titania superstructure is well transferred from the CD blank. However, the height of the structure is determined to be around 100 nm, which shows a less than 45% decrease compared to the structure on the CD blank. The loss in structure height is expected and mainly attributed to the evaporation of cellulose, which is a component in the commercial paste, during calcination. Solvent evaporation also influences the loss of the structure height. The same height-shrink behavior has been reported by Niedermeier *et al.*.[23, 24] It concludes that the collapse of the structure during calcination is rather constant, and this height loss can be taken into account when designing new master structures to overcome it. [23] However, the structure on the CD blank is not suitable for this demand. A further structure master made by photolithography is needed.

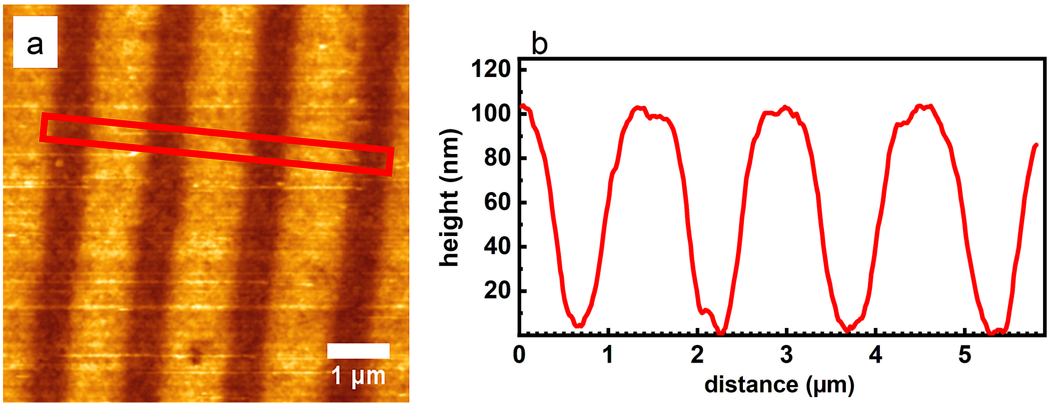

Figure 7.3 *a) AFM topography image of wet-imprinted titania film, b) the corresponding height profile of the rectangular region, which is indicated in a).*

7.1.3 Characterization of DSSCs based on structured titania

Two batches of DSSCs are fabricated in this section via blade-coated titania film with and without superstructure. The wet imprinting process is applied for structured DSSCs, which has been discussed in detail in the previous section. The organic dye D149 as an absorber and the corresponding recipe for liquid electrolyte are used. Both recipes are described in more detail in chapter 4.2.5. The results of the J-V curves based on DSSCs are plotted in Figure 7.4.

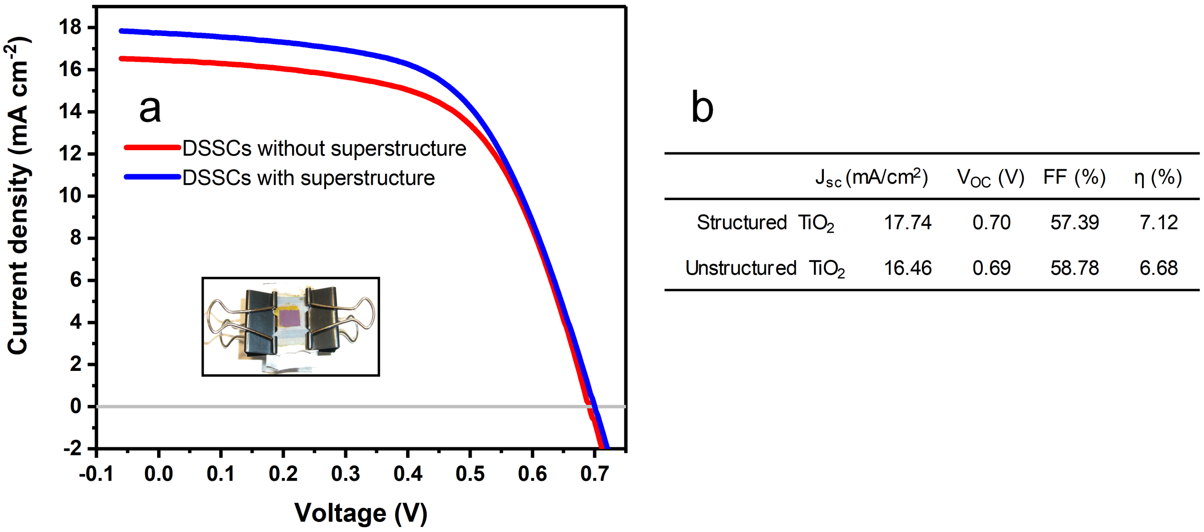

	J_{sc} (mA/cm^2)	V_{OC} (V)	FF (%)	η (%)
Structured TiO_2	17.74	0.70	57.39	7.12
Unstructured TiO_2	16.46	0.69	58.78	6.68

Figure 7.4 *a) J-V curves of the liquid electrolyte-based DSSCs obtained from the blade-coated titania films with /without superstructure. The measurements are performed under AM1.5 simulated solar spectrum (1000 W/m^2) conditions. The insets show the photograph of final DSSC device. b) the table shows the parameters, which are obtained from analyzing the J-V curves.*

Cell parameters determined from the J-V curve are shown in the inset of Figure 7.4. It reveals that the open-circuit voltage (V_{OC}) and fill factor (FF) are nearly identical, which is expected due to the same material and parameters used for deposition of each layer. The current density (J_{SC}) of DSSCs with superstructure shows a higher value comparing the one without superstructure. It mainly results in a higher PCE of 7.12% for structured DSSCs, which is approximately 6.6% greater than that without superstructure. The improvement is attributed to the fact that superstructure, which acts as the light trapping layer, can be elongated the optical path length. The parallel interface refraction effect is used for the structured DSSCs,[216] in which incoming light will scatter preferentially into the channel structures and acquire an angular spread in the titania films. Moreover, when the angle of scattered light is beyond the critical angle for reflection, the light remains trapped in the titania structures. It effectively increases the absorption efficiency of the dye molecules.

Although light trapping structure has been achieved in organic photovoltaics,[217, 218] it rarely reported for DSSCs, which is due to the difficulty in patterning the inorganic titania layer.[219] Here, we followed the wet-imprinting method from Niedermeier,[219] and adapted it to structure the commercial titania paste for DSSCs application. We provide an alternative way to pattern the titania film via wet-imprinting method for DSSCs, and an enhancement of PCE is shown in the performance of DSSCs.

7.2 Nanoimprinting

In this section, the nanoimprinting prepared titania films are studied. Due to a film hardness requirement for the nanoimprinting, the sol-gel prepared titania film, which consists amorphous titania and diblock copolymer (PS-*b*-PEO), is desirable for this method. To overcome the height loss during the calcination step, the Si master is designed by a photolithography process. The corresponding imprinting stamps are prepared. An optical microscope, SEM and AFM are used to characterize the structural features.

7.2.1 Fabrication routine

Silicon substrates are used to fabricate the Si structure master. After acid cleaning, the substrates are heated, followed by evaporation of an adhesion-promoting layer of HMDS. Then, positive photoresist (S1818, Microposit) is spin coated, followed by soft-bake, UV exposure step, development by 351 developer, and hard-bake. Finally, the samples are etched by reactive ion plasma, and cleaned by acetone bath to remove the photoresist remains.

In order to fabricate the OrmoStamps for the imprinting, the silicon master is treated by a monolayer of PFOTS. After plasma treatment for the silicon master and glass slice, the OrmoPrime is spin coated onto the glass slice, followed by thermal heating at 150 °C for 5 min. The OrmoStamp solution is cast onto the silicon master, then covered by pre-coated glass slice on top. After UV light treatment, the OrmoStamp samples are fabricated.

For the preparation of titania films, a compact titania film is firstly spin coated.[138] Then, the sol-gel solution with a weight ratio of $W_{1,4\text{-dioxane}} : W_{HCl} : W_{TTIP} = 0.92: 0.01: 0.07$ is prepared as explained in chapter 4.2.3. To achieve the desired thickness of titania films, spin-coating (at 2000 rpm for 60 s with the fastest acceleration) is applied three times. The thicknesses of hybrid titania films prepared by spin coating 1, 2, and 3 times are (132 ± 10) nm, (285 ± 10) nm, and (453 ± 10) nm, respectively. After spin-coating of the hybrid titania films, the samples are imprinted by NIL-2.5 at 130 °C, under a pressure of 55 bar for 30 min.

7.2.2 Morphology

A photo mask is designed in a parallel line grating structure, with the structured area of 2 x 2 cm^2. Figure 7.5 shows the optical microscope images of selected samples after development. It indicates longer development time results in more photoresists being dissolved by the developer solution (Figure 7.5b). Figure 7.5c shows longer exposure time results in disordered line structure of the photoresist. It is attributed to insufficiently dissipated nitrogen, which is generated by a reaction during UV exposure step. The adhesion between photoresist and Si substrate becomes weaker when more nitrogen gas is generated. The photoresist layer partially disattaches from the substrate during development. A proper exposure and development time are crucial in the photolithography process.

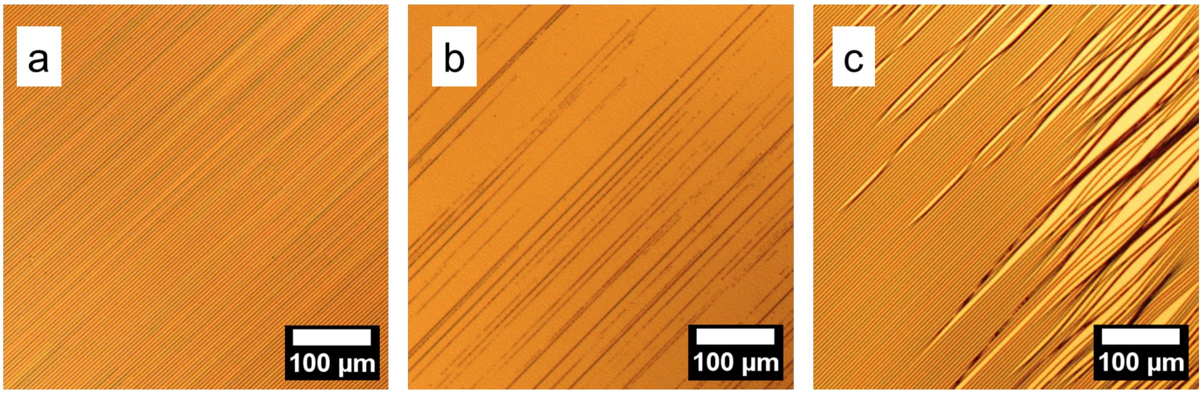

Figure 7.5 *Selected optical microscope images of samples after dipping into developer solution with varying different exposure and developing time. a) an exposure time of 7 s and development time of 6 s; b) an exposure time of 7 s and development time of 30 s; c) 20 s and developing time of 6 s;*

After hard bake, the samples are measured by Dektak profilometer, and it reveals the photoresist film has a thickness of 2 µm. Reactive ion etching is performed to transfer the structure to the silicon master. The structure depth is controlled by the etching time. To calculate the etching rate of silicon, 7 samples are tested with different etching time (shown in Figure 7.6). The thin layer of defined SiO_2 forms on the top surface of silicon samples, which is shown in the grey region in Figure 7.6. A linear fitting is performed based on the data points. It reveals the etching rate for silicon is (4.6 ± 0.2) nm/s. After calcination, a film thickness of around 230 nm for mesoporous titania is desired. Considering the height loss during the calcination, a thickness of around 450 nm for the hybrid films is needed after spin-coating. Therefore, the etching time for RIE is set to 104 s, which results in a structure depth of (400 ± 10) nm.

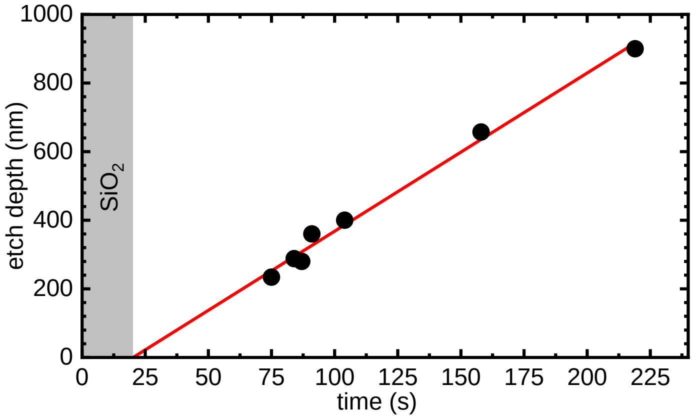

Figure 7.6 *A plot of etching depth as a function of time during RIE etching. Silicon wafer with defined silicon dioxide layer on top, which is shown in the grey region. The red line shows the linear fitting based on the data points.*

The compact titania layer, which reduces the charge recombination losses in the PSCs, is spin coated on top of the silicon substrates. Figure 7.7a shows the SEM images of compact titania films after calcination. The top surface of compact titania films is uniform and smooth, and a thickness of (77 ± 3) nm is observed from the cross-sectional SEM image, which is shown in the inset of Figure 7.7a. The mesoporous titania film is prepared by spin-coating three times. The homogeneous mesoporous titania film after calcination is shown in Figure 7.7b. A thickness of (230 ±10) nm is obtained via three times spin-coating.

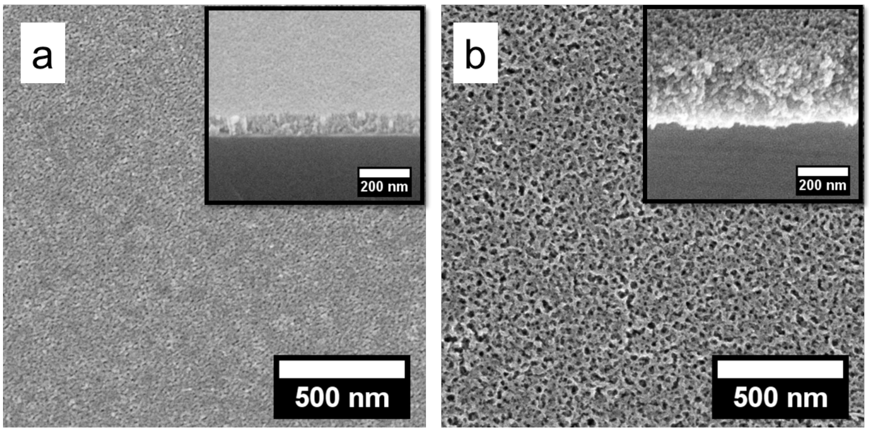

Figure 7.7 *SEM images of a) compact titania films and b) mesoporous titania films. In the insects, the cross-sectional views of compact and mesoporous titania films are shown respectively.*

To get quantitative information of the structure height profile, the silicon structure master, OrmoStamp and structured titania films (after calcination) are characterized by AFM. The photographs of the silicon structure master, OrmoStamps and structured titania films are shown in Figure 7.8 a, d and g, respectively. Due to the periodical line structure, which acts as a line grating, a colorful diffraction pattern is visible over the structured area. The plots of the height profile are taken across the red rectangular regions in AFM results. For the silicon master, the parallel line grating with a periodicity of 4 µm is shown in Figure 7.8 b and c. The line grating exhibits a height of 400 nm. The flat stage and valley have lengths of 2.1 µm and 1.9 µm, respectively. For the OrmoStamp, the replicated inverted structure is observed without height loss. The shrunken line grating structure is observed with a height profile of (85 ± 4) nm by AFM (Figure 7.8 h and i). It is attributed to the evaporation of the copolymer matrix. The height loss compared to the sample before calcination is 71%, which is expected before designing the silicon structure master.

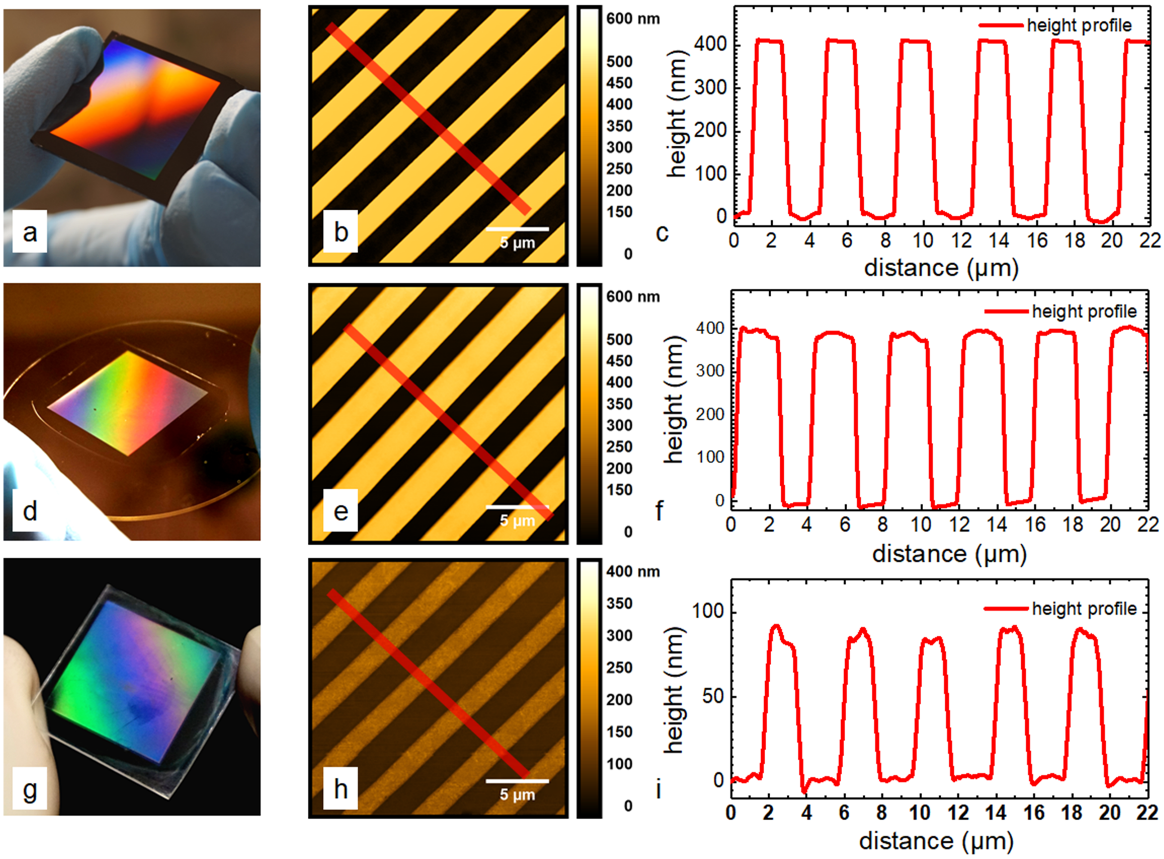

Figure 7.8 *Photographs of a) the silicon structure master, d) OrmoStamp and g) structured titania films after calcination. The corresponding AFM images are shown in b), e) and h), respectively. The corresponding height profile are shown in c), f), and i), respectively. The height profiles are taken across the red rectangular regions in their corresponding AFM images.*

7.3 Summary

Mesoporous titania films with superstructure are successfully fabricated via wet-imprinting and nano-imprinting methods. In the wet-imprinting routine, CD blanks are used as structure master, and PDMS is used as structure transfer stamp. Finally, the blade-coated titania films are structured. Remarkably, the foam structure remains inside the periodical channel structures. The DSSCs based hierarchical structured titania films are manufactured. It shows a PCE of 7.12% for structured DSSCs, which is approximately 6.6% greater than that without superstructure. It provides an alternative way to pattern the titania film via wet-imprinting method, and enhancement of PCE is shown in the performance of DSSCs. In the nano-imprinting routine, the silicon structure master is prepared by photolithography, and OrmoStamps are replicated from the silicon structure master. Due to the small roughness demands for nano-imprinting, the titania films are prepared by spin-coating three times. A height loss of 71%, compared to the films before calcination, is observed. The height loss has been already taken into account before fabrication of the silicon structure master.

8. 2D PEROVSKITE FILM WITH PLASMONIC GOLD NANOPARTICLES

Two-dimensional (2D) Ruddlesden-Popper perovskites (RPPs) often form nanoplatelets and due to the confinement in one crystal direction exhibit properties of quantum wells (QW). It can be described as $(RNH_3)_2A_{n-1}B_nX_{3n+1}$, where RNH_3 = octylamine cation, A = methylammonium cation (MA), *B* = Pb, *X* = Br, and *n* represents the number of lead bromide ($[PbBr_6]^{4-}$) layers along *c*-axis of the crystal. Due to the excellent environmental stability of 2D perovskites, it becomes one of the most important materials for photovoltaic devices.

Recently, Grancini *et al*. claimed to successfully achieve one-year stable 2D/3D perovskite solar cells with PCE of 14.6%, via engineering of the 2D/3D perovskite interface.[87] Furthermore, solar modules with the working area of 10 × 10 cm^2 deliver, over 10000 hours through a printing process, and a PCE of 11.2% with almost no loss in PCE. The huge enhancement of the PSCs' stability is attributed to the interaction between 2D and 3D perovskite, which can expand the band gap of 3D perovskite in the interface region. The 2D perovskite layer acts as a barrier layer to prevent the electron recombination, due to a lower conduction band for 2D compared to 3D phase. 3D perovskite is still sensitive to moisture or a water environment, since the perovskite structure tends to hydrolyze.[138] For example, in case of moisture, the 3D lead iodide perovskite tends to hydrolyze in a partly reversible process, following the stoichiometric equation:

$$\begin{aligned}&4(CH_3NH_3)PbI_3+4H_2O \rightleftharpoons 4[CH_3NH_3PbI_3\cdot H_2O]\\&\rightleftharpoons (CH_3NH_3)_4PbI_6\cdot 2H_2O+3PbI_2+2H_2O\end{aligned}$$

In case of a longer exposure time to water vapor, more dihydrate instead of monohydrate is formed. In direct contact with water, an irreversible process is started following the stoichiometric equation

$$(CH_3NH_3)_4PbI_6\cdot 2H_2O(s) \xrightarrow{H_2O(l)} 4CH_3NH_3I\,(aq)+PbI_6\,(s)+2H_2O\,(l)$$

Through this decomposition process, the performance of PSCs is dramatically decreased. Furthermore, this irreversible process can be accelerated by the decomposition of the organic cations due to the ultraviolet light, thermal heating and the applied of electric field. [220-222]

Although metallic nanostructures are proposed as a way to enhance the performance of the PSCs, the origin of the enhancement remains unknown.[35, 99, 214, 223] Initial studies concluded that the presence of materials, such as Au@TiO_2 and Ag@SiO_2 core-shell nanoparticles, increase the photocurrent in solar devices based on methylammonium lead iodide. However, it cannot be attributed to an enhancement in light harvesting.[214, 224] Later experimental evidence indicates that the core-shell nanoparticles may improve the nonradiative photocarrier generation, separation, transport or collection.[35, 36, 225, 226]

In this chapter, plasmonic nanoparticles are loaded on the super-structured titania films, and a lead bromide perovskite layer is sequentially spin-coated on top. The samples are measured by SEM and AFM. The optical properties of the perovskite films based on structured titania film with nanoparticles are measured by UV-vis and photoluminescence spectroscopy. To identify the exact crystal phase (dimensionality) and orientation of the quasi-2D perovskite, the samples are also characterized by XRD and GIWAXS. The GIWAXS results show no prominent changes in the 2D perovskite crystallites. However, the photoluminescence results indicate the lifetime of photon-excited species is prolonged in the presence of Au@TiO_2.

The solar cells are fabricated based on the combination of 2D and 3D perovskites crystallites. An enhancement in the performance is observed. Finally, an in-operando degradation study of 2D/3D lead bromide perovskite solar cell is carried out via GIWAXS. A small area Xenon lamp is used to emulate the solar spectrum, and the solar cell is operated in a chamber with a controllable humidity during GIWAXS measurement.

This work is done with my master student Markus Trunk, and part of it is in cooperation with Rui Wang from Dr. Henrich Frielinghaus group (Jülich Centre for Neutron science at the FRMII, Garching) and Yu Tong, Florian Ehrat from Prof. Dr. Jochen Feldmann group (Ludwig-Maximilians-Universität München, München).

8.1 Plasmonic nanoparticles on structured titania template

The gold nanoparticles are spray coated on the super-structured mesoporous titania films. After a description of the fabrication routine of Au@TiO_2 based on the structured mesoporous titania films, the top surface morphology of the films is characterized by SEM. Then the optical properties of the films are measured by UV-vis spectroscopy. Afterwards, the volume structure features and crystal structure of the films are probed by GISAXS and GIWAXS, respectively.

8.1.1 Fabrication routine

After structuring the mesoporous titania films, the gold nanoparticles with a diameter of 80 nm (purchased from Sigma Aldrich), which are dispersed in a citrate buffer solvent with a concentration of 7.8×10^9 particles/ml, are spray coated by a spray gun (Infinity CR, Harder & Steenbeck, a nozzle size of 0.15 mm) with a sequential spray protocol of 5 s and 10 s for spray and internal waiting time, respectively. To obtain the dense layer of gold particles, this protocol is repeated 25 times. The parameters for the spray-coating of the gold nanoparticles are listed as follows: nozzle-to-substrate distance of 16 cm, N_2 gas pressure of 2 bars, the heating temperature of 120 °C for the substrates, and spray rate of 1.37 ml/min. Then, the samples are placed on the hotplate at 150 °C for 30 min to dry the films. In order to obtain the core-shell structure of $Au@TiO_2$, the samples are followed by a $TiCl_4$ bath treatment, then calcinated at 500 °C for 30 min after heating at a ramp of 500°C/h.

8.1.2 Morphology

Gold particles are sprayed onto mesoporous titania films with and without super-structure. The core-shell structure is formed after the $TiCl_4$ treatment. Figure 8.1a shows that Au @TiO_2 particles with a diameter of 82 nm are randomly distributed on the mesoporous titania films. It indicates that 2.6% of the titania surface is covered by $Au@TiO_2$ particles. The fast Fourier transform and zoom-in image are shown in the bottom left and top right, respectively.

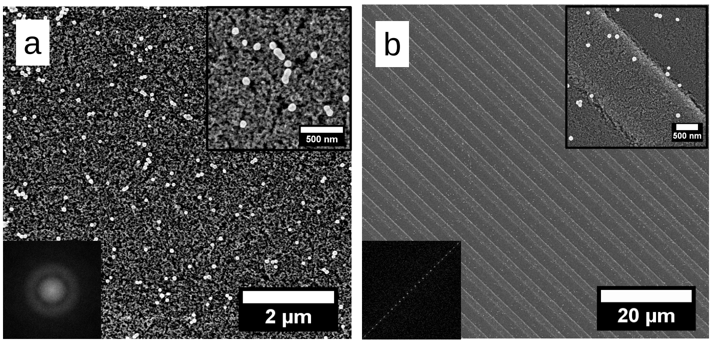

Figure 8.1 *SEM images of* $Au@TiO_2$ *based on the a) mesoporous titania films and b) mesoporous titania films with parallel line structure. The patterns, after fast Fourier transformation, are shown separately at the bottom left corner in each SEM image. Zoomed-in images are shown as insets at the top right corner of each SEM images.*

Aggregates of $Au@TiO_2$ nanoparticles are observed, which is due to the diffusion of $Au@TiO_2$ particles during the calcination step. The localized surface plasmons are dramatically decreased by this aggregation. To minimize the aggregation rate, the imprinted mesoporous titania films are used. The parallel line structure provides a barrier border to constrain the diffusion during calcination. Moreover, the particle density appears to be larger for the probed area. The particle density is calculated from Figure 8.1b by the software ImageJ. It reveals that 4.2% of the titania surface is covered by Au@TiO_2 particles, while the coverage of Au@TiO_2 particles is improved by 62% compared to the one without imprinted structure. The absorption is also benefited by the imprinted structure, which is discussed in section 8.2.2.

8.1.3 Optical properties

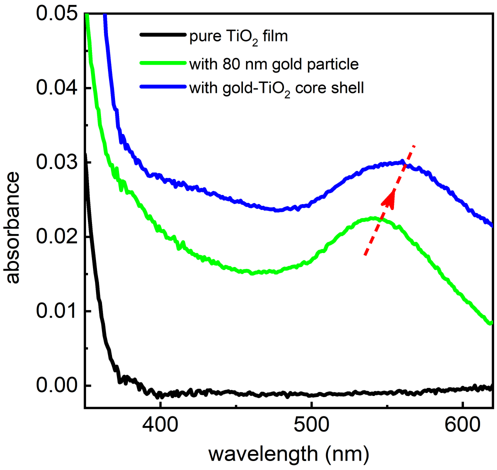

Figure 8.2 *UV-vis absorbance spectra of pure mesoporous titania film (black curve), mesoporous titania film with 80 nm Au particles (green curve), and mesoporous titania film with Au@TiO_2 core-shell particles (blue curve).*

The mesoporous titania films without imprinted structure are used for the UV-vis spectroscopy measurements. An additional calcination step is carried out for mesoporous titania film sample with Au@TiO_2 core-shell nanoparticles(NPs), to crystallize the titania shell structure. Figure 8.2 shows the UV-vis absorbance spectra of pure mesoporous titania film (black curve), mesoporous titania film with 80 nm Au particles (green curve), and mesoporous titania film with Au@TiO_2 core-shell particles (blue curve). The pure mesoporous titania film shows no absorption in the wavelength range from 400 nm to 600 nm. With Au NPs, a peak is formed at 540.5 nm with FWHM of 98 nm, due to a plasmonic resonance of 80 nm gold NPs which enhances the light absorption in the range from 500 nm to 600 nm. The broadening of the absorbance signal is attributed to a polydispersity of gold NPs. The peak position of the absorbance shifts to 552 nm in case of the core-shell Au NPs using (Figure 8.2). This redshift can be attributed to the formation of the Au@TiO_2 core-shell structure. Due to additional calcination, FWHM of this peak is broadened to 105 nm, which is caused by the aggregation of NPs during calcination, as shown in Figure 8.1a.

8.1.4 X-ray characterization

GISAXS and GIWAXS experiments are performed at the P03 MINAXS beamline (PETRA III, DESY, Hamburg) with a beam energy about 13 keV. The finely focused X-ray with a size of 30 × 30 μm^2 impinges on the samples at an incident angle of 0.4°. The footprint of the incoming X-ray beam is 4.3 mm in beam direction. The sample-to-detector distances are 4600 mm and 140 mm for the GISAXS and GIWAXS measurement, respectively. For the samples with imprinted line structures, horizontal alignment parallel to the beam direction is needed. The samples are placed on the sample stage as-close-to-parallel direction as possible. Then the holder is rotated in a range of -0.8° to 0.8° with a step size of 0.002°. The 2D GISAXS data are shown in Figure 8.3. Additional scattering patterns at the specular beam position are observed, named grating truncation rot (GTR).[105, 106, 227, 228] At a highly misaligned angle, as shown Figure 8.3a and Figure 8.3e, the isolated GTRs are observed near the Yoneda region. When the line grating structures are well aligned parallel to the X-ray as shown in Figure 8.3c, GTR does not influence the scattering signal in q_y direction in small q range, due to the micrometer range of the periodical structure. More details about GTR are discussed in section 2.4.

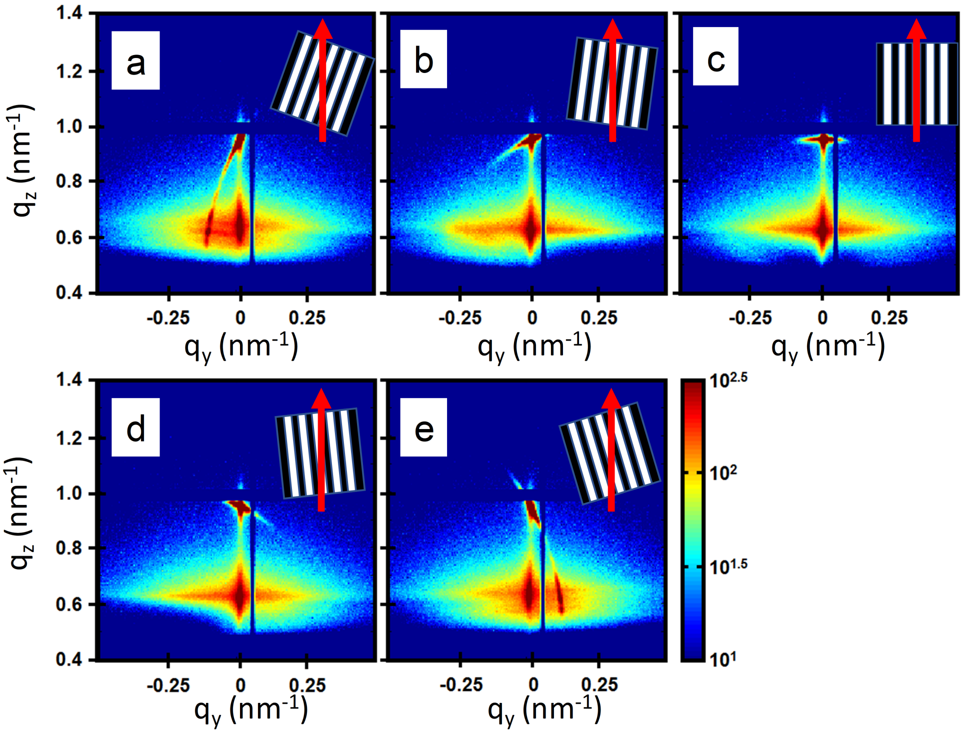

Figure 8.3 2D GISAXS data obtained from alignment for the samples with imprinted parallel line structure. The insets in each image visualize, in an exaggerated way, the rotation of the sample between X-ray (red line with arrow) and line structure (black and white lines) direction. The rotation angles shown are a) -0.8°, b) -0.2°, c) 0°, d) 0.2°, e) 0.8°.

After rotational alignment, the X-ray scattering pattern of the samples, which are compact titania films (named sample A, Figure 8.4a), compact titania / mesoporous titania films (named sample B, Figure 8.4b), and compact titania / structured mesoporous titania / Au@TiO$_2$ NPs (named sample C, Figure 8.4c), are recorded with an exposure time of 1 s. The position of the specular beam is covered by a beamstop for non-structured samples, whereas the beamstop is moved away from the specular position for the structured samples to see GTRs.

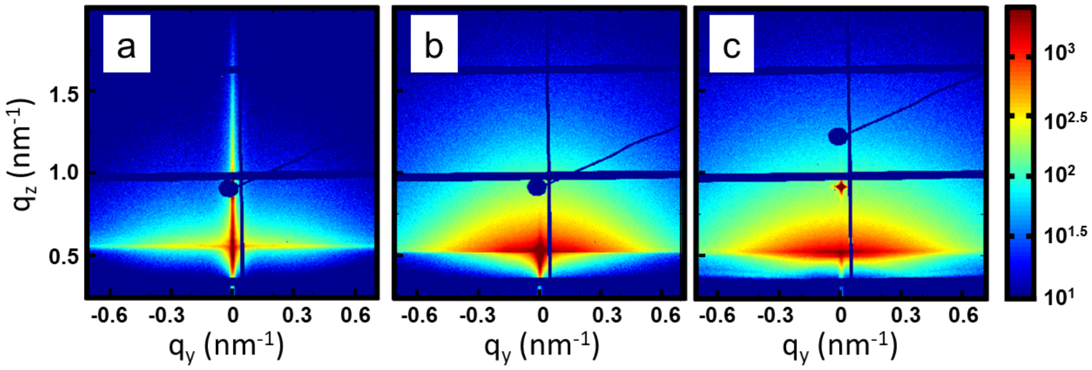

Figure 8.4 *2D GISAXS data of a) compact titania films, b) compact titania film with a mesoporous titania layer on top, c) compact titania / structured mesoporous titania / Au@TiO$_2$ NPs.*

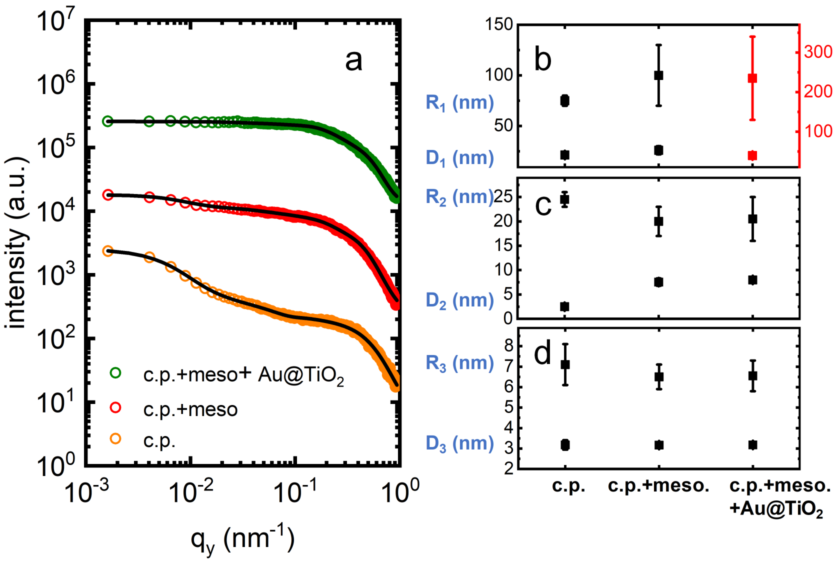

Figure 8.5 *a) Horizontal line cuts, from the Yoneda peak position of titania material with fits (black curve) for compact titania films (orange circle), compact titania/ mesoporous titania films (red circle), and compact titania/ mesoporous titania films/ Au@TiO$_2$ NPs (red circle). The curves are shifted along the y-axis for clarity. b) - d) Values of pore radii $R_{1,2,3}$ and distances $D_{1,2,3}$ extracted from modelling the data.*

The horizontal line cuts are performed at the Yoneda peak position of titania (q_z = 0.66 nm^{-1}) with a width of 5 pixels (Figure 8.5a). The horizontal cuts are shifted along the y-axis for clarity and fitted by a model with three form factors (two for cylinders and one for sphere), which are represented by the black curves in Figure 8.5a. The three different form factors (R_i) and structure factors (D_i) are represented in Figure 8.5b, c, and d, respectively. The D_1 and R_1 of each sample, which are correspond to the form factor of a sphere, represent the structure features of large clusters for the samples without Au@TiO_2 NPs, and the structure features of titania shell structure (R = 41 nm) for the sample with Au@TiO_2 NPs. Figure 8.5c indicates the larger pore size is obtained from the mesoporous titania films, while the structure features from sample B and C are nearly identical. For example, sample A has an average pore radius of (2.5 ±0.1) nm (R_2) and a center-to-center distance of (25 ± 2) nm (D_2), and Sample B has a larger average pore radius of (7.6 ± 0.8) nm (R_2) and a center-to-center distance of (20 ± 3) nm (D_2). All the samples show a similar small structure feature, as shown in Figure 8.5d, which is caused by compact nano crystals of titania films in each sample.

To characterize the crystalline information of the films, the three samples are measured by GIWAXS. The exact sample-to-detector distance for GIWAXS measurements is recalculated by comparison of GIWAXS data and XRD result. Figure 8.6a, b, and c show the 2D scattering patterns for sample a, b, and c, respectively. The Bragg signals of anatase titania are indicated in white, while the one of gold in yellow. The artificial rectangular shaped background in Figure 8.6a, and b are caused by the Kapton window and a lead shield from the setup. The higher intensity in Figure 8.6b, compared to Figure 8.6a, is attributed to the additional titania in the mesoporous layer in sample B. The powder-like crystallites of anatase titania and gold are shown by the Debye-Scherrer rings in Figure 8.6.

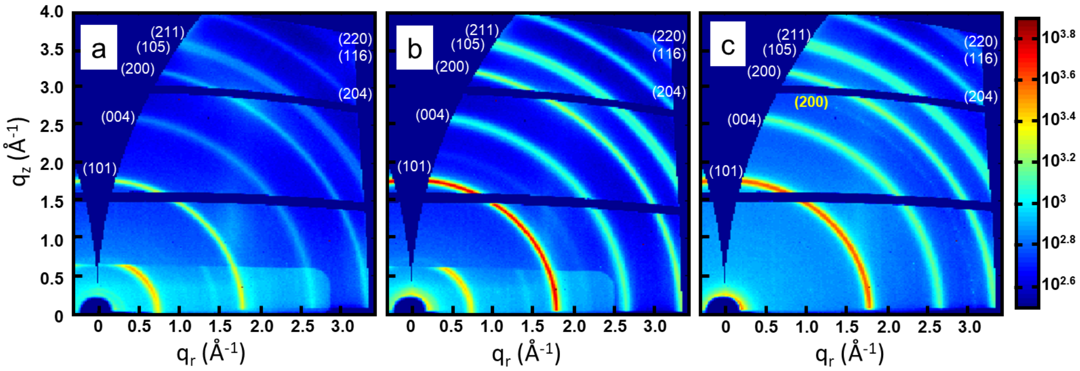

Figure 8.6 *2D GIWAXS data of a) compact titania films, b) compact titania film with a mesoporous titania layer on top, c) compact titania / structured mesoporous titania / Au@TiO_2 NPs. The partial Bragg rings are labeled in white and yellow for titania and gold, respectively.*

The 2D scattering data are integrated over all angles, then plotted in Figure 8.7. For better clarity, the curves are shifted along the y-axis. All the theoretical peak positions are marked in black and yellow for anatase titania and gold, respectively. The peaks, marked by the black rectangle in Figure 8.7a, are fitted by three Gaussian peaks as shown in Figure 8.7b. It indicates that each peak consists of reflexes originating from (103), (004) and (112) planes. The calculated q values of anatase titania match well with theoretical values, as shown in Table 8.1. In conclusion, the titania films are crystallized in the anatase phase. The peaks at 3.07 Å^{-1} and 4.34 Å^{-1} in the green curve in Figure 8.7a are assigned to gold crystallite of (200) and (220), respectively. The sizes of (101) crystallites of anatase titania are calculated based on the Debye-Scherrer equation, in which the shape factor (K) is 0.9. It reveals that the crystal sizes are 11.2 nm, 12.2 nm and 8.5 nm for compact titania film, mesoporous titania films, and structured titania films, respectively. Due to high pressure being applied during the imprint process, the crystal size is slightly reduced and the crystal lattice transforms into a higher symmetry structure.[229]

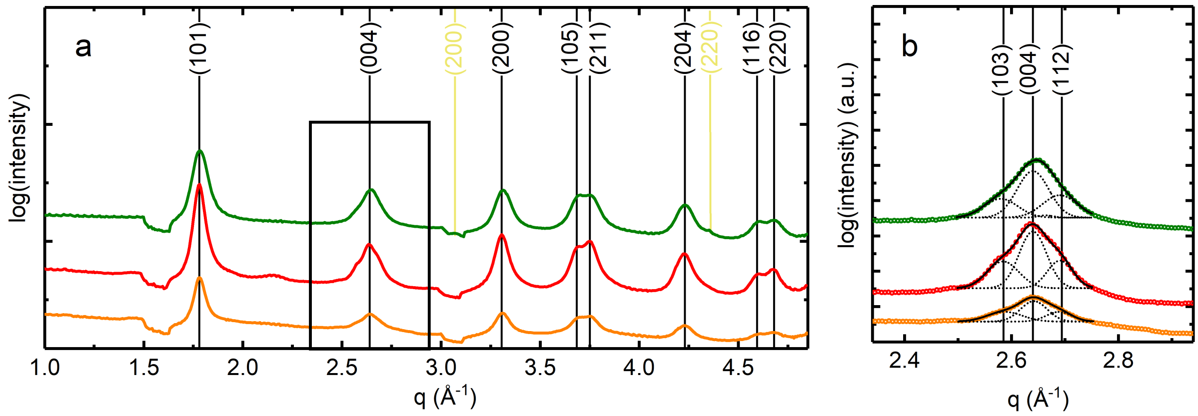

Figure 8.7 *a) One-dimensional scattering curves of compact titania films (orange), compact titania film with a mesoporous titania layer on top (red), and compact titania / structured mesoporous titania / Au@TiO$_2$ NPs (green). b) Zoom-in of the black rectangular region with fits (dotted-black curves). The peak positions are labeled in black and yellow for titania and gold, respectively.*

crystal plane	(101)	(103)	(004)	(112)	(220)	(105)	(211)	(204)	(116)	(220)
experimental q (Å^{-1})	1.78	2.58	2.64	2.69	3.31	3.70	3.75	4.23	4.61	4.68
reference q (Å^{-1})	1.79	2.59	2.64	2.69	3.32	3.70	3.77	4.26	4.64	4.71

Table 8.1 *Crystal information, calculated from GIWAXS data, compared to the JCPDS #21-1272 reference data for anatase titania phase.*

8.2 2D lead bromide films with plasmonic structure

In this section, the 2D and 3D lead bromide films are compared from the morphological view, crystallinity, and optoelectrical properties. A longer lifetime of photon-excited species in 2D perovskite is observed via time-resolved photoluminescence measurements.

8.2.1 2D/3D lead bromide layer

2D and 3D lead bromide layers are spin-coated on the mesoporous titania films via the one-step method as discussed in chapter 4.2.4. Figure 8.8 shows the top surface view of 3D and 2D bromide perovskite films. Micrometer-sized $MAPbBr_3$ crystallites are observed. The interconnection of cuboids is not continuous, therefore a large amount of titania films remains uncovered. The isolated cuboids create high surface roughness and the formation of pinholes in the perovskite solar devices. The power conversion efficiency reduces dramatically, due to the bad interface of $MAPbBr_3$ and titania films and electrical shunt paths. The poor coverage is affected by the one-step coasting method, in which the film shrinkage would occur during the crystallization process due to solvent evaporation.[230] Small crystallite seeds are shown in the Figure 8.8b. In contrast, smooth surface and perfect coverage of 2D $MAPbBr_3$ are observed in Figure 8.8c, d. Well-packed nanoplatelets are visible in the SEM images. Since 2D $MAPbBr_3$ is sensitive to the electron beam, artificial cracks are created during SEM measurement (shown in Figure 8.8c).[231, 232] The cracks are attributed to the long exposure time under the electron beam. It indicates that the roughness and well-packed nanoplatelets are formed when the $C_8H_{17}NH_2$ (OA) is added as an additive. The octahedra crystal structure of $PbBr_6$ is intercalated with several Lead bromide layers of 2D nanoplatelets by OA molecules.

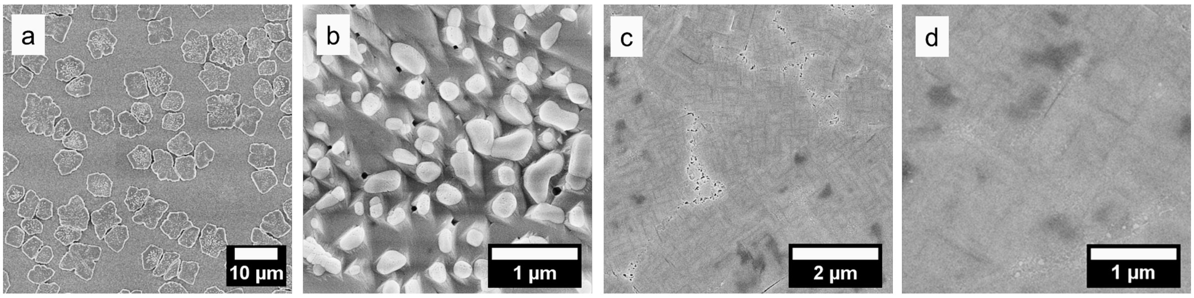

Figure 8.8 *SEM images of a) 3D lead bromide films, b) zoom-in of 3D lead bromide films, c) 2D lead bromide films, and e) zoom-in of 2D lead bromide films.*

Figure 8.9 shows the XRD data of 2D and 3D perovskite films in black and orange curves, respectively. All the Bragg reflection peaks in the orange curve indicate that 3D $MAPbBr_3$ is present in the cubic Pm-3m space group with a lattice constant of 5.94 Å.[233, 234] The black curve is shifted vertically for better clarity. Due to the polycrystalline and random orientation, the 3D perovskite film shows more crystal planes, such as (011), (012), (112), (022), (222) and (023). In contrast, only (00l) crystal system is observed from quasi-2D $MAPbBr_3$ film, which indicates that the nanoplatelets show a parallel orientation to the substrate surface. Besides that, the rest peaks in the black curve are attributed to the different number of 2D nanoplatelet layers. [235, 236]

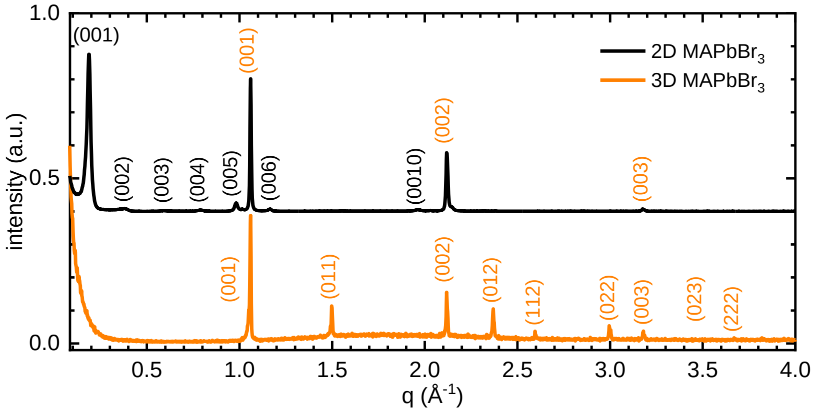

Figure 8.9 XRD data of 2D $MAPbBr_3$ (black curve) and 3D $MAPbBr_3$ (orange curve). The black curve is shifted along y-axis for better clarity. The crystal information is labeled in black and orange for 2D and 3D crystallites, respectively.

The samples are probed by UV-vis and photoluminescence spectroscopy to characterize the optical properties of 2D and 3D $MAPbBr_3$ films as shown in Figure 8.10. A bandgap of (2.27 ± 0.09) eV for 3D $MAPbBr_3$ is calculated from the orange curve near the optical absorption edge in a Tauc plot of Figure 8.10a. Due to the quantum confinement,[237, 238] quasi-2D $MAPbBr_3$ films show a bandgap of (2.31 ± 0.06) eV in a Tauc plot. Additional absorption peaks, which originates from the nanoplatelets with $n = 1, 4, 5$, and 6 lead bromide layers, are observed. Figure 8.10b shows the photoluminescence emission spectra of the quasi-2D (black curve) and 3D (orange curve) $MAPbBr_3$ films. The peak at 533 nm is assigned to the bulk structure ($n=\infty$) of $MAPbBr_3$, which shows that intensity of this peak for the quasi-2D perovskite films is 176 times stronger compared to the 3D perovskite films. Since excited electron-hole pairs can be transferred from a layered perovskite with small n to the one with large n, more peaks are visible in PL measurement, such as the peaks for $n = 2, 7$ lead bromide layers.[239] All UV-vis absorption and PL emission data are listed in Table 8.2, in comparison to values from reported references.[233, 235-237, 240] A Stokes shift of 1-6 nm in PL spectroscopy measurement is attributed to radiative emission from free excitons. [241, 242]

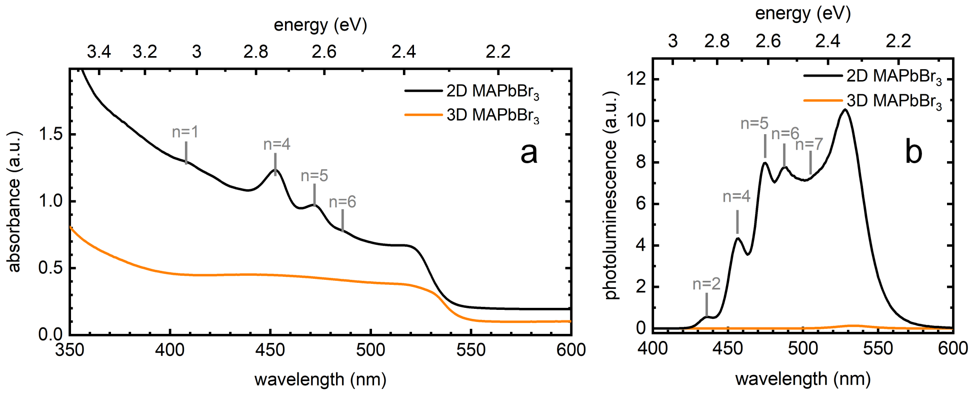

Figure 8.10 *a) UV-vis spectra of quasi-2D (black curve) and 3D (orange curve) MAPbBr$_3$ films. b) PL emission spectra of quasi-2D (black curve) and 3D (orange curve) MAPbBr$_3$ films. The layer information of 2D MAPbBr$_3$ is labeled in gray color.*

dimensionality	n=1	n=2	n=4	n=5	n=6	n=7	n=∞
reference absorption	396 nm	431 nm	451 nm	472 nm	490 nm	497 nm	525 nm
measured absorption	408 nm	-	454 nm	471 nm	486 nm	-	-
reference emission	427 nm	442 nm	456 nm	475 nm	490 nm	504 nm	530 nm
measured emission	-	436 nm	456 nm	475 nm	488 nm	505 nm	529 nm

Table 8.2 *The comparison of measured UV-vis and PL spectroscopy data with the reference data.*[233, 235-237, 240]

In addition, both quasi-2D and 3D MAPbBr$_3$ films are measured by time-resolved PL spectroscopy to study charge-transfer kinetics from the perovskite layer to the FTO/TiO$_2$ substrate (as shown in Figure 8.11). The reduction of an average lifetime from 55.2 ns ($n = \infty$) to 2.3 ns ($n = 1$) is attributed to the larger binding energy for thin nanoplatelets. In the case of the transition from 3D to 2D structure, the ideal binding energy is followed by $E_b^{2D} = 4´\ E_b^{3D}$.[84] Furthermore, the thinner nanoplatelets result in the enhanced Coulombic attraction between the electron and hole in the electron-hole pairs.[243] Therefore, it promotes the excitonic recombination by dimensional reduction. Figure 8.11b represents the exciton decays at the peak of n=∞ in 2D (l = 529 nm) and 3D (l = 533 nm) MAPbBr$_3$ films. The dramatic decrease of a lifetime from 55.2 ns (2D MAPbBr$_3$) to 1.4 ns (3D MAPbBr$_3$) can be ascribed to the isolated crystal seeds in the 3D perovskite crystal structure. This incoherent structure results that the excited electron-hole pairs cannot be transferred into the adjacent crystallites, and while a fast recombination is occurred. In contrast, electron-hole pairs in layered 2D perovskite are shown elongated the carrier lifetime, due to formation of continuous perovskite film via surface passivation and less defects at grain boundaries.

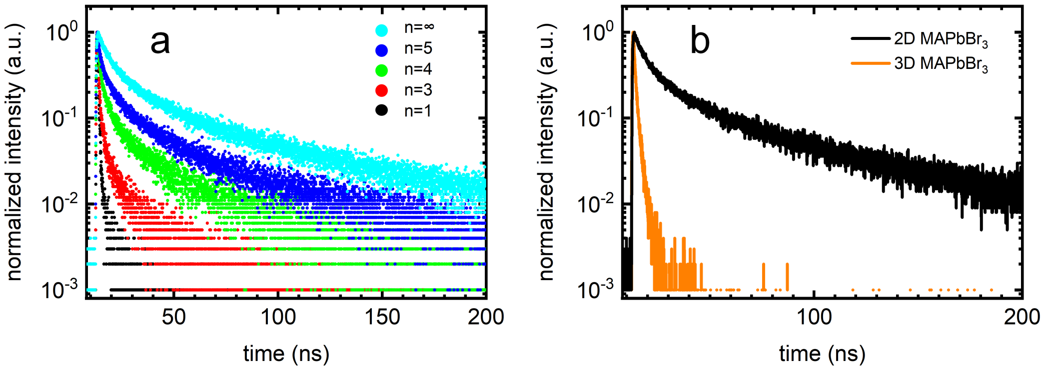

Figure 8.11 *PL decay profiles of quasi-2D and 3D MAPbBr$_3$ films. a) Exciton decay at the nanoplatelets with deferent dimensionality. b) Comparison of exciton decay for quasi-2D and 3D MAPbBr$_3$ films.*

8.2.2 Influences of plasmonic structure on 2D lead bromide layer

In this section, the line grating structure and Au@TiO$_2$ core-shell NPs are applied on the mesoporous titania films before deposition of quasi-2D MAPbBr$_3$ films. In order to simplify the sample names, sample D represents the sample with a structure of FTO/ compact titania/ mesoporous titania/ quasi-2D MAPbBr$_3$ films, sample E represents the sample with a structure of FTO/ compact titania/ imprinted mesoporous titania/ quasi-2D MAPbBr$_3$ films, sample G represents the sample with a structure of FTO/ compact titania/ quasi-2D MAPbBr$_3$ films, and sample F represents the sample with a structure of FTO/ compact titania/ imprinted mesoporous titania/ Au@TiO$_2$ NPs/ quasi-2D MAPbBr$_3$ films. Sample D, E, and F are probed via GISAXS with a rotation alignment. The exposure time for each frame is set to 1 s with an incident angle of 0.4°.

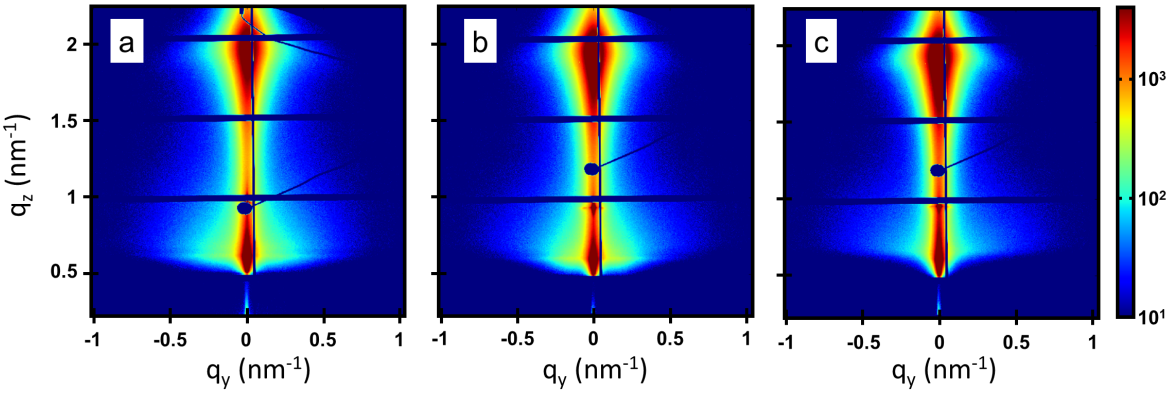

Figure 8.12 *2D GISAXS scattering patterns of a) quasi-2D MAPbBr$_3$ films based on the mesoporous titania (sample D), b) quasi-2D MAPbBr$_3$ films based on the imprinted mesoporous titania (sample E), c) quasi-2D MAPbBr$_3$ films based on the imprinted mesoporous titania with Au@TiO$_2$ NPs (sample F).*

Figure 8.12 shows the GISAXS scattering pattern for sample D, E and F. The d-spacing can be calculated by:

$$d = \frac{2p}{q} \tag{8.1}$$

Therefore, the prominent scatter signal at $q_z = 1.9$ nm^{-1}, which corresponds to a d-spacing of 32.7 Å, is caused by the 2D $MAPbBr_3$ crystallite with 4 layers of lead bromide layer.[244] To obtain the sizes of structure feature, the horizontal cuts are performed at the $MAPbBr_3$ Yoneda peak position of $q_z = 0.706$ nm^{-1} with a width of 5 pixels as shown in Figure 8.13. The data is modeled using from factors for cylinder with radii R_i, and different structure factors (D_i) as shown in Figure 8.13b. The structural features are nearly identical despite different samples. It indicates that in the probed length range the morphology of quasi-2D $MAPbBr_3$ films is not affected by the imprinted structure, nor by $Au@TiO_2$ NPs.

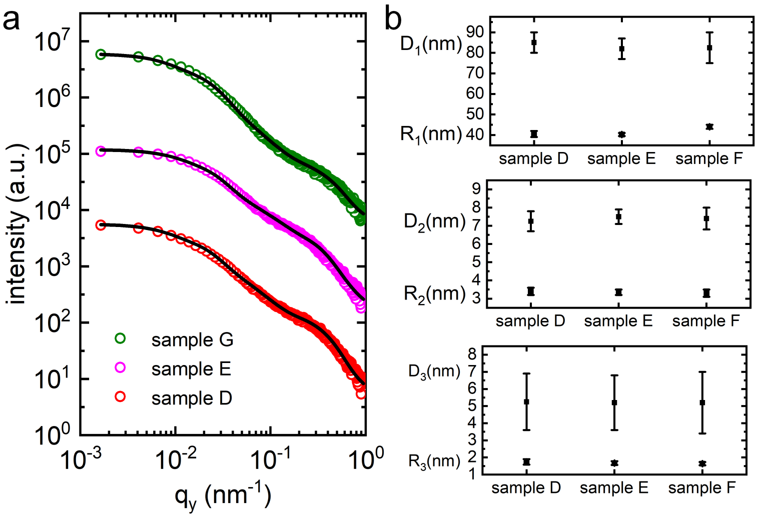

Figure 8.13 *a) Horizontal line cuts of sample D (red curve), sample E (pink curve), sample F (green curve) at the* $MAPbBr_3$ *Yoneda peak position* ($q_z = 0.706$ nm^{-1})*. For better clarity, the curves are shifted vertically, and the fitting curves are represented in black. b) The structure features extracted from the fits.*

In order to identify the influence of mesoporous titania layer to quasi-2D perovskite, the perovskite films are also deposited on the compact titania film (sample G). The crystal structure and orientation of samples D, E, F and G are measured via GIWAXS. The corresponding lattice planes are labeled on the GIWAXS images as shown in Figure 8.14. The presence of pronounced Bragg peaks along the q_z direction at $q_r > 1$ Å^{-1} reveals that highly oriented Pm-3m cubic crystal space group of 3D bulk crystals ($n = \infty$) in quasi-2D $MAPbBr_3$ film are distributed parallelly to the sample surface. Whereas, the Bragg peaks at $q_r < 1$ Å^{-1} are originated from layered 2D $MAPbBr_3$ nanoplatelets. The homogeneous Debye-Scherrer rings of anatase titania and $PbBr_2$ precursor without pronounced Bragg peaks are observed, which implies no preferential orientation of titania and $PbBr_2$ crystallites in the perovskite films. For the sample of the quasi-2D $MAPbBr_3$ based on the compact titania films (sample G), the broader Bragg peaks, compared to the one based on the mesoporous titania films, indicates porous structure enhances the crystal quality of perovskite films, which is also reported by others. [40, 184, 245]

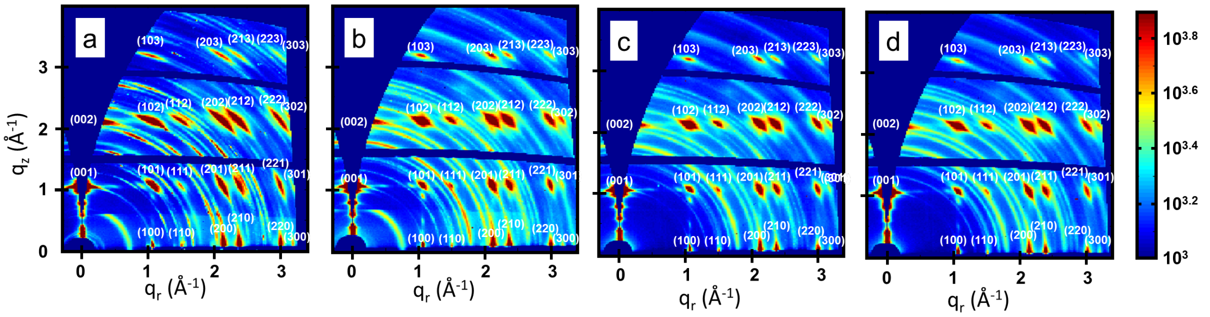

Figure 8.14 *2D GIWAXS pattern of the samples as a) sample G, b) sample D, c) sample E, d) sample F. The lattice planes are labeled in white color.*

Furthermore, GIWAXS data is quantitatively analyzed from the tube cut around (101), (102) and (201) Debye-Scherrer rings, and the comparison in (101) peak is shown in Figure 8.15a,b. In Figure 8.15c, the full width at half maxima (FWHM) of those peaks are plotted. The decrease of FWHM from 5.4° (sample G) to 2.9° (sample D) indicates the larger crystallites presents in the quasi-2D $MAPbBr_3$ films based on mesoporous titania films, as opposed to the one based on compact titania films. Nearly constant FWHM value of samples D, E and F are found. This reveals that crystalline order and orientation are not affected by imprinted titania structure, nor by Au@TiO_2 NPs.

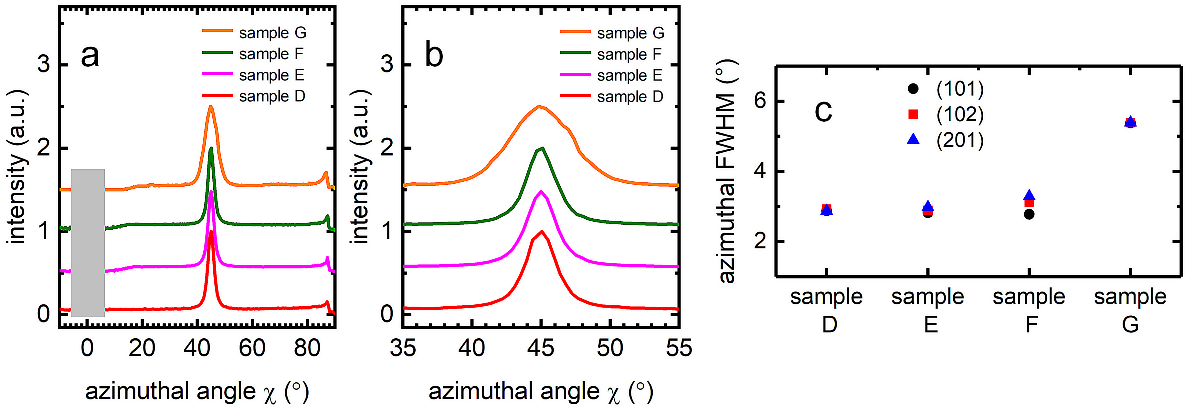

Figure 8.15 *a) Azimuthal cuts of sample D, E, F, and G around (101) Debye-Scherrer rings. The non-accessible data around $c = 0^{\circ}$ is represented as a gray rectangular. b) Zoom-in plot around peak 45°. c) Plot of FWHW based on (101), (102) and (201) peaks of sample D, E, F and G.*

The XRD patterns of quasi-2D perovskite films are recorded, as shown in Figure 8.16. The (00*l*) (*l* = 1 - 6) crystallite diffraction peaks with a d-spacing of $d_{(001)}$ = 32.7 Å are listed in Figure 8.17b. It indicates the nanoplatelets with an interlayer spacing of 32.7 Å is horizontally aligned in the perovskite films as shown in Figure 8.17a. The films mainly consist of nanoplatelets with n=4 lead bromide layers, considering layered octylamine-based quasi-2D perovskite with an interlayer spacing of 32.7 Å (15 Å + 3 × 5.9 Å).[236, 246] The peaks at q = 1.009 Å^{-1} and q = 2.024 Å^{-1} represent the (004) and (008) crystal planes of OABr remains. In the condition of 0.4° as an incident angle, the whole films are probed by GIWAXS. However, 2D nanoplatelets with four lead bromide layers mainly contribute to the GIWAXS data. It implies that the n = 1, 2, 5, 6,7 of lead bromide layers, which we are previously observed via UV-vis and PL spectroscopy measurement, take a small proportion of the whole perovskite films, compared to 2D nanoplatelets with n=4 lead bromide.

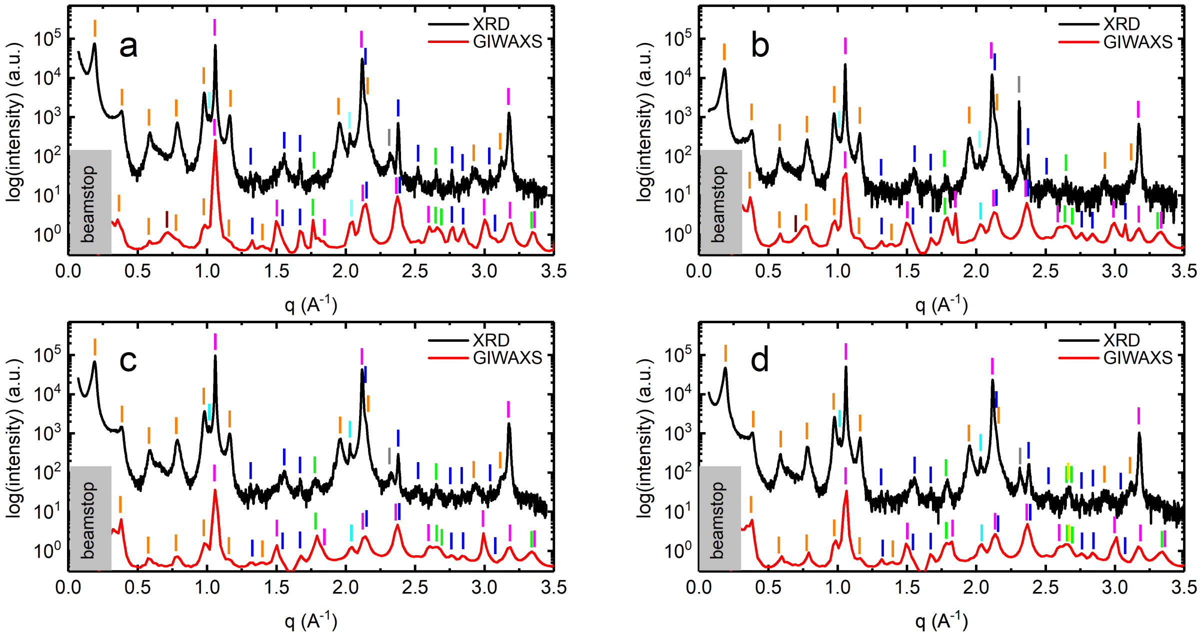

Figure 8.16 *Comparison of XRD patterns with corresponding integration over GIWAXS data. a) sample G, b) sample D, c) sample E, d) sample F. The XRD curves are shifted vertically for better clarity. The peaks for n = ∞ (3D) perovskite, n = 4 of 2D perovskite, OABr, $PbBr_2$, anatase titania, silicon, and gold are labeled as pink, orange, cyan, blue, green, gray and yellow, respectively. The peak from the Kapton window is labeled in brown.*

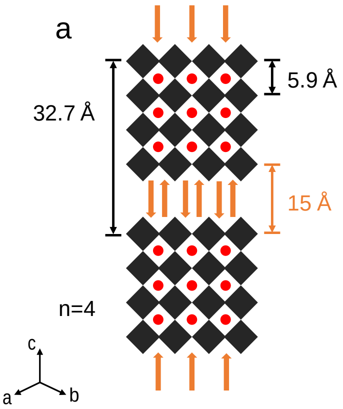

b

(hkl)	q_{theory} (Å^{-1})	q_{exp} (Å^{-1})	d_{exp} (Å)
(001)	0.194	0.183	34.31
(002)	0.389	0.382	16.44
(003)	0.583	0.581	10.81
(004)	0.777	0.781	8.04
(005)	0.972	0.973	6.45
(006)	1.166	1.160	5.41

Figure 8.17 *a) Schematic layered quasi-2D structures of perovskites (n=4). b) Calculated q and d values based on XRD data of sample D compared with theoretical q value.*

In an effort to characterize the optical properties of the same samples, angle-resolved UV-vis spectroscopy is employed, as shown in Figure 8.18. For sample D, four pronounced peaks at lower wavelengths than 500 nm are observed in the Figure 8.18a, b, c, corresponding to the nanoplatelets with 1, 4, 5, and 6 lead bromide layers, respectively. Each sample's absorbance determined as a function of angle is plotted in Figure 8.18b, and for better comparison the absorbance is normalized to the value of normal beam incidence and the integrated absorbance from 400 nm to the bulk perovskite bandgap position (2.31 eV, 537 nm). The samples are placed inside an integrating sphere for the UV-vis spectroscopy measurements to collect all scattered light from the samples. At a rotation angle of 0° (the incident beam is impinged on the sample surface perpendicularly), the measured absorbance of the samples is slightly overestimated. This is caused by a direct back-reflection out of the integrating sphere, which the instrument treats as part of the absorption of the samples, since it is not captured by the detector.

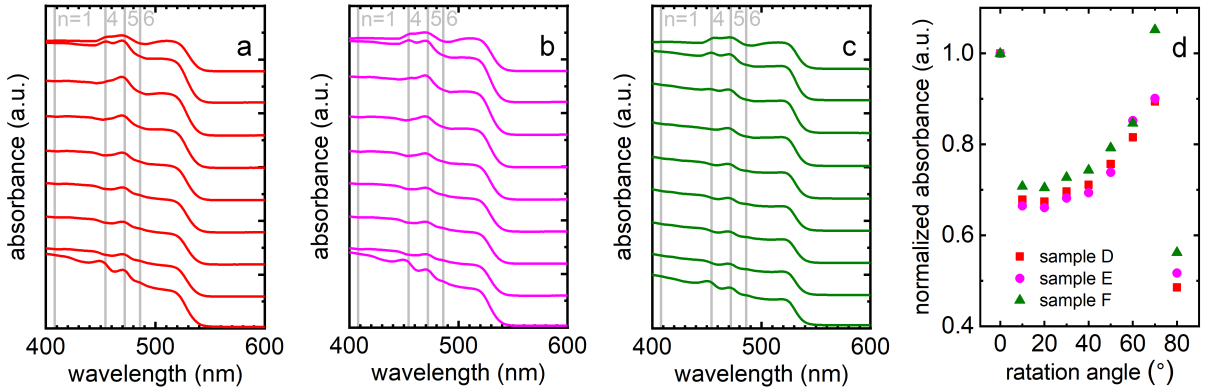

Figure 8.18 *Angle-resolved absorbance spectra with a normalized absorbance: a) sample D, b) sample E, c) sample F. The curves from bottom to top, which are shifted vertically for better clarity, represents the rotation angle from 0° to 80°, respectively. b) Normalized absorbance data integrated from 400 nm to 537 nm (bandgap of perovskite) for sample D, E, and F.*

Overall, the absorbance of the samples shows a gradually increasing tendency with increasing the rotation angles from 10° to 70°. This is expected, as the optical path length of incoming light is effectively increased within the sample with an increasing rotation angle. Most notably among these three samples, the absorbance of sample F (the imprinted mesoporous titania films with Au@TiO_2 NPs) is enhanced. This is attributed to additional light scattering created by the presence of Au@TiO_2 NPs. The incoming light is guided by the Au@TiO_2 NPs, then angularly spread into the perovskite layer. In particular, when light scatters at an angle beyond the critical angle for reflection, it will remain trapped in the perovskite layer.[247] Besides the guiding light effect, Au@TiO_2 NPs also act as a secondary light source, which increases the photon flux when the sample rotates to a certain angle with respect to incoming light. These two factors contribute to the enhancements of optical absorption. Due to the dimension of the incoming light spot, part of the incoming light does not impinge on the sample surface when the angle is rotated to 80°, which results in an extreme loss of the samples' absorbance.

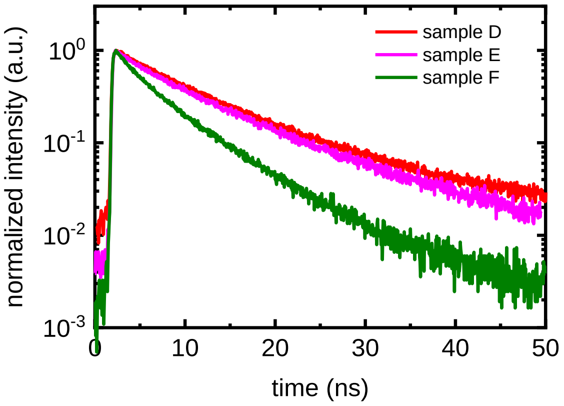

***Figure 8.19** Time-resolved photoluminescence data of samples: quasi-2D perovskite based on mesoporous titania (sample D), quasi-2D perovskite films on imprinted mesoporous titania films (sample E), quasi-2D perovskite films on imprinted mesoporous titania films with Au@TiO_2 NPs (sample F).*

Lifetimes of photon-excited species are calculated from the plots obtained from time-resolved photoluminescence measurement, as shown in Figure 8.19. The Au@TiO_2 NPs are excited by additional laser with (590 ± 10) nm. Since this wavelength is close to where localized surface plasmons can be excited at Au@TiO_2 NPs, sample F shows an exciton lifetime of 6.0 ns, compared to the exciton lifetimes of 10.5 ns and 10.2 of samples D and E, respectively. As we demonstrated previously, the morphology and crystallites of perovskite are not affected by the presence of imprinted microstructure and Au@TiO_2 NPs. Therefore, the enhancement of electric field, caused by localized surface plasmon resonance (LSPR), leads to a fast dissociation rate of electron-hole pairs at the interface of perovskite and titania layers, which results in the short lifetime of electron-hole pairs. Recently, it reported that the PCE of PSCs is enhanced by up to 44% by incorporating 80 nm sized Au@TiO_2 NPs, compared with the reference device without metal NPs.[36] Huang *et al.* assume the enhancement mechanism is explained by improved exciton generation rate, enhanced exciton dissociation probability, and more efficient carrier transfer and collection induced by the LSPR effect. However, the crystal changes of perovskite, such as lattice distortion, deep trap states and grain boundaries, can also influence the charge carrier lifetime,[248-250] which are not excluded in that research. Here, grazing incidence X-ray scattering and TRPL results directly prove that the enhancement is associated with efficient carrier dissociation rate by LSPR effect, and not affected by the perovskite layer.

8.3 Solar cell performance

8.3.1 Routine to improve the PCE of 2D PSCs

The routines to prepare 2D and 3D $MAPbBr_3$ films are discussed in the section 4.2.4. Additionally, the combination of 2D and 3D perovskite films are sequentially hot-spin-coated with quasi-2D perovskite followed by annealing at 100 °C for 10 min, then hot-spin-coated with 3D perovskite films. Finally, the blended 2D/3D films are annealed at 100 °C for 10 min before spin-coating the spiro-OMeTAD layer, then deposit the gold layer by thermal evaporation in high vacuum. The illustration of the PCS is shown in Figure 8.20.

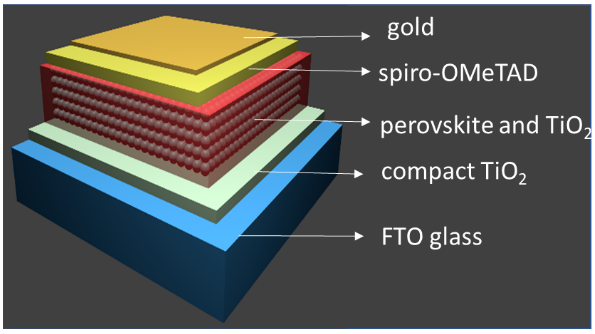

Figure 8.20 *Sketch of perovskite solar cells based on mesoporous titania structure. After deposition of perovskite layer, a thin capping layer is formed on top of mesoporous titania layer.*

Giesbrecht *et al.* reported the micrometer-sized $MAPbBr_3$ based PSCs reached the PCE of 6.08% via controlled solvent drying.[251] 2D $(BA)_2(MA)_3Pb_4I_{13}$ PSCs with a PCE up to 13.7% was achieved by Cs^+ doping, and it demonstrated the grain size, optoelectronic properties, and stability are beneficial by Cs^+ doping.[252] Smith *et al.* report the layered perovskite $(PEA)_2(MA)_2[Pb_3I_{10}]$ exhibit higher stability compare to 3D perovskite with an n open-circuit voltage of 1.18 V and a PCE of 4.73%. Here, we compare the 2D/3D PSCs with pure 2D or 3D PSCs. All the fabrication steps of PSCs are performed in ambient environment. The devices with an active area of 0.18 cm^2 are measured under AM1.5 solar simulator light without preconditioning. The J-V curves of these three devices are plotted in Figure 8.21a. The arrows indicate the scan direction and the device parameters are listed in Figure 8.21b. The isolated perovskite crystallites in 3D perovskite films mainly cause the huge difference between the 2D perovskite (V_{oc}=1.23 V) and 3D perovskite (V_{oc}=0.69 - 0.71 V). The larger bandgap of 2D perovskite affords a higher V_{oc} compared to 3D perovskite. Additionally, since V_{oc} is influenced by the distribution of electronic density of states in conduction band of perovskite and, it implies 2D perovskite has a narrow distribution of the electronic density of states, and a small degree of energy disorder, compared to the 3D perovskite.[253] However, the loss of current density is caused by the bad interconnection between the perovskite and titania layer. To achieve high performance of PSCs, a combination of 2D and 3D perovskite layer is deposited. The V_{oc} of 0.94 V indicates after twice spin-coating, the quasi-2D perovskite remains a well-aligned crystal orientation. The J_{sc} of 4.83 mA/cm^2 reveals that the 2D/3D perovskite is almost fully converted from the precursor. The best performance of 2.97% is obtained from the PCSs based on 2D/3D perovskite. It should be noted that all the PSCs are not optimized toward reaching champion efficiencies. However, the improvement in PCE appears promising for further studies of 2D/3D PSCs.

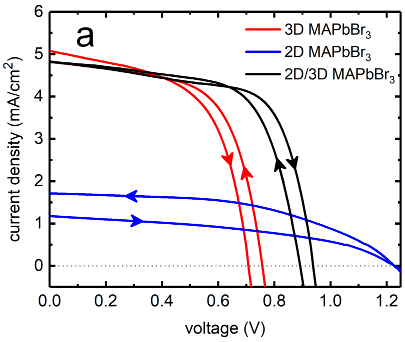

b

series	J_{sc} (mA/cm^2)	V_{oc} (V)	FF (%)	PCE (%)
3D average	4.37 ± 0.61	0. 69 ± 0.02	58.9 ± 3.3	1.78 ± 0.38
3D best fwd.	5.08	0.71	57.6	2.07
3D best rev.	4.85	0.69	62.0	2.26
2D average	1.11 ± 0.59	1.22 ± 0.02	45.1 ± 3.8	0.62 ± 0.33
2D best fwd.	1.18	1.23	42.8	0.62
2D best rev.	1.71	1.23	49.9	1.05
2D/3D average	4.22 ± 0.55	0.91 ± 0.03	62.3 ± 3.0	2.41 ± 0.4
2D/3D best fwd.	4.83	0.94	65.4	2.97
2D/3D best rev.	4.81	0.89	64.4	2.77

Figure 8.21 *a) J-V curves of 3D MAPbBr$_3$ (red curve), 2D MAPbBr$_3$ (blue curve), and 2D/3D MAPbBr$_3$ (black curve), as a perovskite layer in PCSs. b) Characteristic parameters of these three batches of PSCs.*

GIWAXS measurements are performed at the SAXS beamline at the Elettra Sincrotrone Trieste. The PSC based on 2D/3D perovskite layer is measured with an incident angle of 0.4°, X-ray energy of 8 keV, and SDD of 317.5 mm. Debye-Scherrer rings with superimposed Bragg spots are observed, as shown in Figure 8.22a. It implies the perovskite film exhibits randomly orientated crystallites. Considering the high V_{oc} from this device, the formation of 2D/3D perovskite crystallites can be concluded as follows: after annealing of quasi-2D perovskite layer, horizontal orientated nanoplatelets are not well connected with adjacent ones; second spin-coating of 3D perovskite solution partially dissolves the pre-deposited 2D perovskite films, bulk perovskite crystallites incorporates with 2D structure to form a compact layer. The cross-sectional SEM image of this device is shown in Figure 8.22b. It confirms that a compact perovskite capping layer is formed.

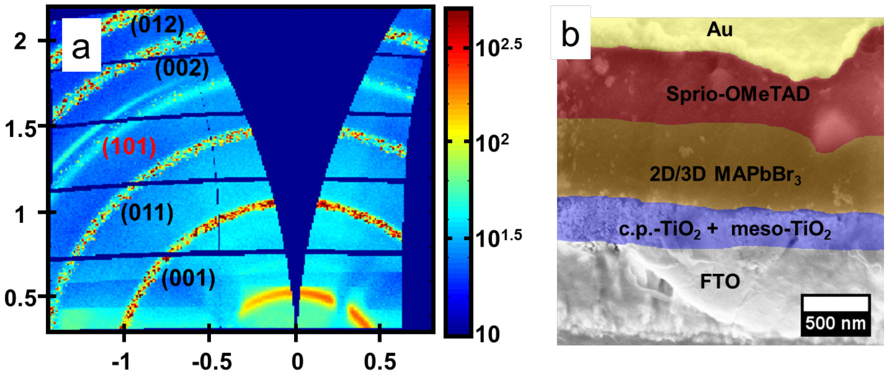

Figure 8.22 *PSCs based on 2D/3D MAPbBr$_3$ films as a perovskite layer a) 2D GIWAXS image, b) cross-sectional SEM image.*

8.3.2 In-operando degradation of PSCs

The perovskite materials, such as MAPbI$_3$ and MAPbBr$_3$, are sensitive to moisture. The interaction with water reduces the device performance. For example, in the case of exposure to warm humid air (relative humidity above 50%), MAPbI$_3$ is decomposed into HI, PbI$_2$ and CH$_3$NH$_2$, and losses to PCE are observed.[254, 255] Leguy *et al*. reported the water molecules can incorporate with perovskite films homogeneously through the whole films, which means the water molecules are highly mobile within the perovskite lattice and along grain boundaries.[138] In contrast to 3D perovskite films, 2D films have shown promising stability.[89, 256, 257] In order to overcome this limitation, it is vital to understand the degradation of perovskite crystal in moisture atmosphere.

In this section, the degradation behavior of PSCs based on 2D/3D MAPbBr$_3$ is studied. FTO glasses are etched with zinc powder and HCl, followed by sequentially sonicating them in a bath of Alconox detergent, DI water, ethanol, acetone, and 2-propanol, respectively. After oxygen plasma treatment, a compact titania film is deposited, which is adapted from Leguy's paper.[138] Then the samples are calcinated at 500 °C for 45 min. The mesoporous titania films are deposited, using the sol-gel method with a weight ratio of 0.92:0.01:0.07 (dioxane: HCl: TTIP), and calcinated at 500 °C for 30 min. TiCl$_4$ bath is used to reduce the trap state on the mesoporous surface. 2D MAPbBr$_3$ is prepared by a molar ratio of 1:0.8:0.2 (PbBr$_2$: MABr: OA). After annealing 2D MAPbBr$_3$ films, 3D MAPbBr$_3$ is prepared by a molar ratio of 1:1 (PbBr$_2$: MABr), then spin coated on top of the samples, followed by another annealing treatment.

Spiro-OMeTAD and gold are used as a hole transport layer and a counter electrode, respectively. More experimental details are described in sections 4.2.4 and 4.2.5.

In-operando GIWAXS measurement is carried out at the SAXS beamline at the Elettra Sincrotrone Trieste. The 2D/3D perovskite solar cell is placed in a hermetic chamber with Kapton windows, and measured with X-rays at 8 keV with an incident angle of 0.4°. A Pilatus3 1M detector is placed 317.5 mm away from the sample. A small area Xenon lamp is calibrated by a certified reference silicon cell to emulate the solar spectrum of AM1.5 conditions. J-V measurement is controlled and measured by a Keithley 2400 with a scan speed of 100 mV/s in forward direction. The chamber is firstly pumped to 1 mbar, then the injection of DI water creates a stable humid atmosphere after the pumping stopped. Through this method, a relative humidity level of around 87% is reached after 50 min (Figure 8.23b). The X-ray (along *x*-direction) is impinged on the area where is near the gold electrode, then move along *y*-direction with a step of 1 mm (Figure 8.23a).

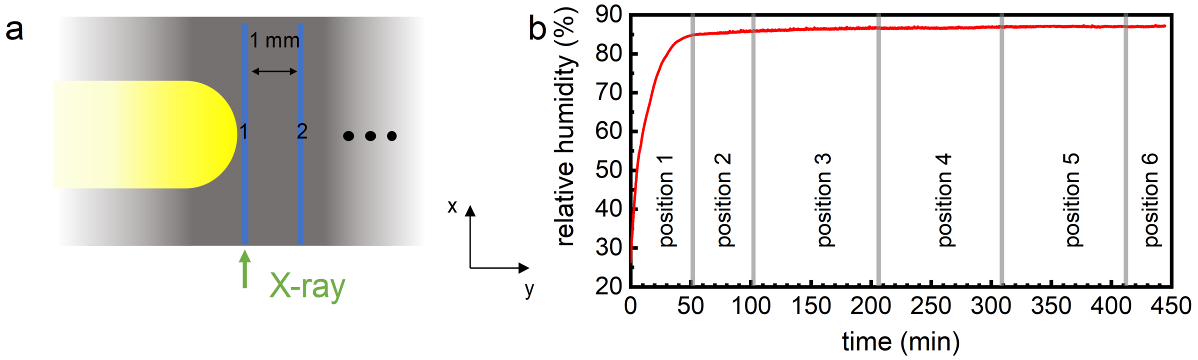

***Figure 8.23** a) Illustration of probed position on PSC device during in-operando GIWAXS measurement. The incoming X-ray beam is along x-direction, and the probed area is marked in blue. The position 1 – 6 are shifted along y-direction with a stepwise of 1 mm. b) The evolution of humidity changes in the chamber during in-operando GIWAXS measurement.*

The operating perovskite solar cell is probed by GIWAXS with a 2D detector. Figure 8.24 shows selected scattering patterns from the in-operando measurements. The orientation of Bragg spots changes with different probe area (after each cycle, a fresh area is probed to avoid beam-damage). However, the Debye-Scherrer rings keep the same position as compared quasi-2D perovskite films. It indicates disordered 2D perovskite crystals are merged into the 3D perovskite matrix with the same lattice spacing. We assume the 2D $MAPbBr_3$ recrystallizes and is more orientated in the 3D matrix. However, due to wrapping with 3D perovskite crystals, this recrystallization and the highly ordered structure cannot be measured by GIWAXS, thus only Bragg spots are observed.

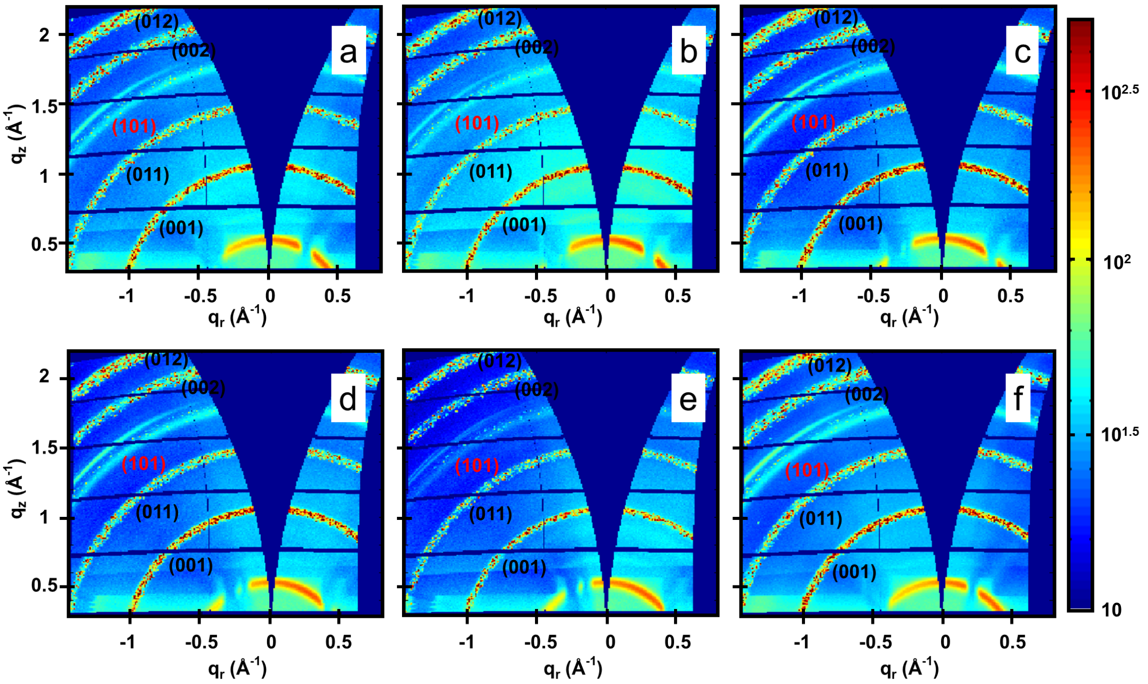

Figure 8.24 *Selected 2D GIWAXS images at a) 0 min, b) 33.3 min, c) 66.8 min, d) 133.5 min, e) 200.1 min, f) 266.8 min. Crystalline profiles of* $MAPbBr_3$ *are labeled in black, and (101) anatase titania phase is labeled in red.*

The integration of GIWAXS data in (001) perovskite reflex peak position is performed. To exclude fluctuation from the X-ray beam, the intensity of each peak is normalized based on the intensity of the Kapton ring around q=0.528 Å^{-1}. The maximums intensity and FWHM of peak (001) as a function of time are shown in Figure 8.25. Due to the inhomogeneity of 2D/3D perovskite films, the maximum intensity and FWHM of peak (001) shows an incoherent jump when move to another position. In the first-time period (position 1), the maximum intensity of peak (001) is nearly constant. In contrast, the increase of FWHM indicates the crystal size is reduced, and the reduction of crystal size is around 1 nm. It can be attributed to the hydrolyzation of the 3D perovskite crystallites, where the hygroscopic and volatile nature of the organic compound leads to water ingress and film degradation. The reduced intensity in the regime of position 2 indicates the number of perovskite crystallites is decreased, and it is owing to the degradation process of $MAPbBr_3$ under the moisture conditions.[258, 259] The growth of crystals is revealed by a slight drop of FWHM. There are no pronounced changes in both intensity and FWHM values after the third-time regime. Thus, the 2D/3D perovskite films degrade slightly in the beginning (0 to 100 min), then exhibit a stable crystal structure under the moisture conditions.

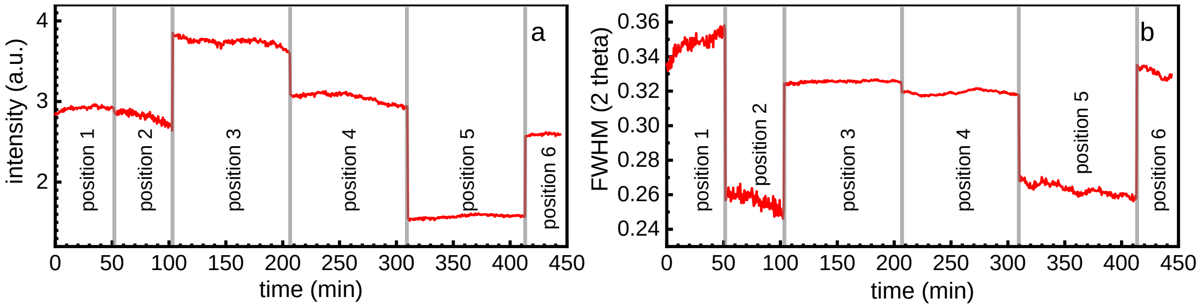

Figure 8.25 *Evolution of perovskite crystallites as a function of time from the (001) peak position. a) Changes of maximum intensity of peak (001). b) Changes of FWHM of peak (001).*

The evolution of the photovoltaic parameters of PSC device as a function of operation time is shown in Figure 8.26. The increase of PCE is observed until the humidity establishes constant conditions in the measurement chamber (in position 1). However, the GIWAXS results reveal the perovskite the size of crystallites is decreased, and it does show the improvement of crystallites. We propose the increase of PCE is correlated to improvement of Au/ HTM interface. Afterwards, a PCE reduces slowly until 100 min is reached, then a subsequent degradation of the device performance is observed. V_{oc}, I_{sc}, FF, R_s (series resistance), and R_{sh} (shunt resistance) are calculated from IV curve. The I_{sc} and FF both reduce to about 50%. In contrast, the V_{oc} degrades to 0, which mainly results in PCE of 0%, although a current is measured to flow through the device. Until the relative humidity stabilizes, both V_{oc} and FF increase until reaching stable humidity, while the I_{sc} linearly decreases and the series resistance R_s remains constant. Before 100 min, the nearly constant R_s attributes to a stabilization of PCE. In the time range from 100 min to 211 min, the R_s increases dramatically, which leads to the fast decrease in PCE. After 211 min, the shunt resistance R_{sh} decreases strongly. It indicates that a high reverse current flow occurs, which leads damages in small spots and increasing a temperature locally. These damages mainly lead to the device not functionalize after 420 min.[260]

After a long exposure time of solar device under the solar simulator, the sample can be considered as continuous heating by solar simulator. Whereas, the Au atoms diffuse across spiro-MeOTAD layer into perovskite layer when temperature exceeds 70 °C. [261] The deep trap states within the device can be formed due to Au atoms diffusing, which results the enhancement of nonradiative recombination and the degradation of V_{oc} and I_{sc}. This nonradiative recombination can cause dramatic performance loss, and the formation of damage spot in the perovskite solar device. Finally, the solar device undergoes a full loss of V_{oc}, even though perovskite crystallites still present in the device. It indicates that the driving factor for the degradation process of 2D/3D perovskite solar cells is not affected by the degradation of perovskite. On the contrary, the influence of Au atoms diffusion and degradation of spiro-OMeTAD may play an important role. S. Kim et al. reported that the conductivity of spiro-OMeTAD can be affected by the diffusion of I^- ions, which is occurred at 85 °C, since the diffused I^- ions prevent the oxidation of spiro-OMeTAD.[262] Furthermore, at temperature range from 60 °C to 120 °C and under a relative humidity up to 50%, the deformation of the spiro-OMeTAD and the unidentified modification at the $MAPbI_3$/ spiro-OMeTAD interface[263] also need to take into account.

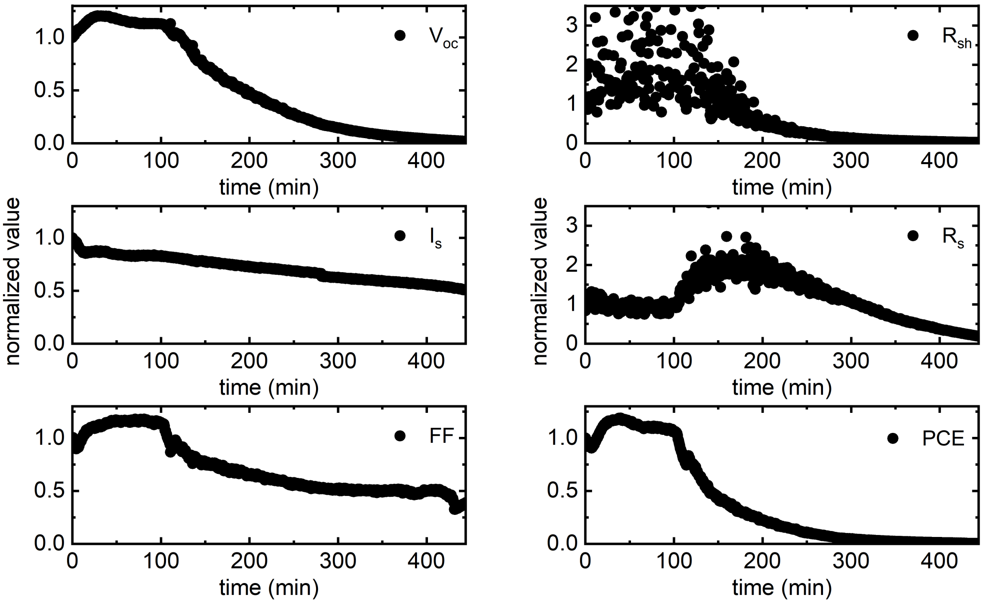

Figure 8.26 *Photovoltaic performance under moisture atmosphere with time. All the parameters (V_{oc}, I_{sc}, FF, R_s, R_{sh} and PCE) are normalized to initial values for clarity.*

8.4 Summary

Imprinted mesoporous titania with Au@TiO_2 NPs is applied in quasi-2D perovskite solar devices. The imprinted mesoporous titania films are fabricated by a photolithography method, and the depth of the grating structure is designed for photovoltaic applications. Angle-resolved absorbance spectra results show the enhancement of light absorption for the sample with the grating structure and addition of plasmonic Au@TiO_2 NPs, when sample is rotated with a certain angle with respect to incident light. From the GISAXS and GIWAXS results, it is concluded that the 2D perovskite films are not affected by grating structure and Au@TiO_2 NPs. However, the shorter exciton lifetime of 6.0 ns, from the 2D perovskite films based on the imprinted mesoporous titania with added Au@TiO_2 NPs, indicates the carrier dissociation efficiency is enhanced by localized surface plasmon resonance. The results reveal the perovskite crystals are not affected by the application of structured titania films or Au@TiO_2 NPs. Therefore, the short carrier-lifetime of the films with periodical structure and Au@TiO_2

NPs, which is observed by time-resolved photoluminescent, is only attributed to faster dissociation rate of carrier by localized surface plasmon resonance effect. PSCs based on 2D/3D perovskite films with PCE of 2.97% are fabricated with a configuration of FTO/ compact titania layer/ mesoporous titania layer/ 2D/3D perovskite/ gold. Finally, the degradation behavior of the 2D/3D PSC under moisture conditions is studied. The crystal size and the number of $MAPbBr_3$ are slightly decreased in the time range from 0 to 100 min. Afterwards, there are no pronounced changes in the perovskite crystallites. Based on the in-operando GIWAXS and the corresponding IV results, there is no correlation between crystal changes of 2D/3D perovskite and degradation of PSC device. It suggests that the degradation of PSCs is not attributed to 2D/3D perovskite, but may be caused by the diffusion of Au atoms into perovskite layer, diffused I^- ions in spiro-MeOTAD layer and instability of spiro-MeOTAD under moisture and illumination conditions.

9. SUMMARY AND OUTLOOK

In the present thesis, mesoporous titania is investigated as an electron-transfer layer in dye-sensitized solar cells (DSSCs) and perovskite solar cells (PSCs). A periodic superstructure and gold noble metal nanoparticles are applied in the aim to enhance the light-trapping property and carrier dissociation efficiency.

For industrial fabrication, scale-up deposition methods are important. Thus, the spray-coating as a large-scale deposition technique is chosen and systematically studied. In general, A controllable pore size for mesoporous titania films can be successfully synthesized via spray coating. The spray ink consists of: PS-*b*-PEO as a structure directing template, TTIP as a titania precursor, HCl as a selective solvent and 1,4 – dioxane as a good solvent for PS-*b*-PEO. In case of increasing the weight fraction of TTIP, the titania structures become bicontinuous, and the pore size decreases slightly. In case of varying spray protocols, the titania film with more uniformed pore sized are obtained. This ordered pore size is crucial for photovoltaic devices. The crystal phase of titania film are mainly affected by the calcination temperature. The XRD results show that the average crystal size of anatase titania is increased slightly with an increase of temperature from 400 °C to 700 °C, and while the titania film in rutile phase can be achieved at a calcination temperature of 800 °C.

The structure evolution mechanism during spray-coating is investigated via *in situ* GISAXS and macroscale-simulation. On a nanoscale, the structure size is decreased after the heating interval time, due to the evaporation of the solvent. When the concentration of diblock copolymer reaches the point of over-saturation, the condensation process occurs spontaneously. In the following spray step, the fresh droplets partially dissolve the film, then form a continuous compact film. On a macroscale, the simulation results match well with the optical microscopy results. It indicates that the initial droplet size is in a range of 25 µm to 28 µm in this spray configuration and the present hot zone regime not only dries the films, but also influences the droplet size. The PSC based on spray-coated titania film via sol-gel route is compared with the one based on spin-coated titania film, which use a diluted conventional commercial titania paste to achieve the same film thickness. The increase of PCE for the former configuration is attributed to the well-controlled titania pore structure. The combination of sol-gel route and spray-coating method present a promising method in achieving an industrial fabrication standard in photovoltaic applications.

The periodical structure has been proven to enhance the light absorption in organic solar cells. However, it is difficult to apply it to titania films, due to their high mechanical hardness. Two different approaches for DSSCs and PSCs are investigated. In the configuration of DSSCs, the PDMS stamp with line grating structure are replicated from CD structure. After blade-coating the commercial titania paste, the grating structure are transferred onto the titania film via wet imprinting at 80 °C in 1 hour. It provides an easy way to structure a titania films without requiring machinery. A higher PCE of 7.12% is observed for structured DSSCs, compared to the PCE of 6.6% for nonstructured DSSCs. The second route is nanoimprinting, and it is related to the whole photolithography processes. Since the height losses of sol-gel prepared titania film always occur during the calcination step, it is crucial to fabricate the stamp with a desired structure depth. In an aim to increase the gold particle density and enhancement of the plasmonic effect in a certain rotated angle, the periodic line structure is transferred to mesoporous titania film for PSC devices. Finally, the structured mesoporous titania film with a structure depth of (85 ± 4) nm is achieved.

As mentioned in the introduction, the mechanism of plasma enhancement is still not clear. In order to study the origins of plasma enhancement, the quasi-2D $MAPbBr_3$ films are deposited on the samples under these conditions: compact titania layer; compact titania layer/ mesoporous titania layer; compact titania layer/ mesoporous titania layer with a periodical line structure; compact titania layer/ mesoporous titania layer with a periodical line structure/ $Au@TiO_2$ nanoparticles. The results reveal that the crystallinity is improved by mesoporous structure, however, the quasi-2D $MAPbBr_3$ film is not affected by periodical line structure and $Au@TiO_2$ nanoparticles. The shorter exciton lifetime for the sample with a line grating structure and $Au@TiO_2$ nanoparticles is observed from time-resolved photoluminescence results. Based on all the results above, this shorter exciton lifetime is only attributed to the faster carrier dissociation efficiency triggered by localized surface plasmon resonance enhancement. For PSCs fabrication, the PSCs based on a combination of 2D/3D perovskite films shows the best performance with a PCE of 2.26%. In the end, the degradation behavior of PSCs based on 2D/3D $MAPbBr_3$ under moisture conditions is studied. From the in-operando GIWAXS and the corresponding IV results, it does not show any correlation between the crystal changes of 2D/3D $MAPbBr_3$ and the degradation of solar device. The degradation of 2D/3D $MAPbBr_3$ occurs in the initial 100 min and the changes of crystal size are around 1 nm, which is mainly caused by the 3D $MAPbBr_3$ component in the films. Afterwards, perovskite films show a stability under the moisture conditions. We propose the dramatic performance loss of PSC device is caused by the diffusion of Au atoms across HTM to perovskite layer, diffused I^- ions in spiro-OMeTAD layer, and the degradation of spiro-OMeTAD at the elevated temperature. However, the perovskite crystallites are still presented in the PSCs till the full loss of V_{oc}. Therefore, in order to achieve long-term stable 2D/3D PSCs, it is necessary to find an efficient way to avoid the Au migration and using another more stable HTM material in future.

BIBLIOGRAPHY

[1] A. Becquerel, "Mémoire sur les effets électriques produits sous l'influence des rayons solaires", *Originalarbeit zur Einwirkung von Licht auf Elektroden*, vol. 9, 1839.

[2] M. A. Green, "The path to 25% silicon solar cell efficiency: History of silicon cell evolution", *Prog Photovoltaics*, vol. 17, pp.183-189, 2009.

[3] M. A. Green, Y. Hishikawa, E. D. Dunlop, *et al.*, "Solar cell efficiency tables (version 51)", *Progress in Photovoltaics: Research and Applications*, vol. 26, pp.3-12, 2018.

[4] V. Fthenakis, "Sustainability of photovoltaics: The case for thin-film solar cells", *Renewable and Sustainable Energy Reviews*, vol. 13, pp.2746-2750, 2009.

[5] B. O'Regan, M. Grätzel, "A low-cost, high-efficiency solar cell based on dye-sensitized colloidal TiO_2 films", *Nature*, vol. 353, pp.737-740, 1991.

[6] S. Ahmad, E. Guillen, L. Kavan, *et al.*, "Metal free sensitizer and catalyst for dye sensitized solar cells", *Energy Environ. Sci.*, vol. 6, pp.3439-3466, 2013.

[7] S. Mathew, A. Yella, P. Gao, *et al.*, "Dye-sensitized solar cells with 13% efficiency achieved through the molecular engineering of porphyrin sensitizers", *Nat. Chem.*, vol. 6, pp.242-247, 2014.

[8] J. Burschka, N. Pellet, S.-J. Moon, *et al.*, "Sequential deposition as a route to high-performance perovskite-sensitized solar cells", *Nature*, vol. 499, pp.316-319, 2013.

[9] H. Zhou, Q. Chen, G. Li, *et al.*, "Interface engineering of highly efficient perovskite solar cells", *Science*, vol. 345, pp.542-546, 2014.

[10] M. Saliba, T. Matsui, J.-Y. Seo, *et al.*, "Cesium-containing triple cation perovskite solar cells: improved stability, reproducibility and high efficiency", *Energy Environ. Sci.*, vol. 9, pp.1989-1997, 2016.

[11] W. S. Yang, B.-W. Park, E. H. Jung, *et al.*, "Iodide management in formamidinium-lead-halide–based perovskite layers for efficient solar cells", *Science*, vol. 356, pp.1376-1379, 2017.

[12] C. Yi, X. Li, J. Luo, *et al.*, "Perovskite photovoltaics with outstanding performance produced by chemical conversion of bilayer mesostructured lead halide/TiO_2 films", *Adv. Mater.*, vol. 28, pp.2964-2970, 2016.

[13] Y. Yue, T. Umeyama, Y. Kohara, *et al.*, "Polymer-assisted construction of mesoporous TiO_2 layers for improving perovskite solar cell performance", *J. Phys. Chem. C*, vol. 119, pp.22847-22854, 2015.

[14] G. Yang, H. Tao, P. Qin, *et al.*, "Recent progress in electron transport layers for efficient perovskite solar cells", *J. Mater. Chem. A*, vol. 4, pp.3970-3990, 2016.

[15] P. Docampo, S. Guldin, T. Leijtens, *et al.*, "Lessons learned: From dye-sensitized solar cells to all-solid-state hybrid devices", *Adv. Mater.*, vol. 26, pp.4013-4030, 2014.

[16] S. D. Burnside, V. Shklover, C. Barbé, *et al.*, "Self-organization of TiO_2 nanoparticles in thin films", *Chem. Mater.*, vol. 10, pp.2419-2425, 1998.

[17] H. J. Snaith, M. Grätzel, "Electron and hole transport through mesoporous TiO_2 infiltrated with spiro-MeOTAD", *Adv. Mater.*, vol. 19, pp.3643-3647, 2007.

[18] P. Tiwana, P. Parkinson, M. B. Johnston, *et al.*, "Ultrafast terahertz conductivity dynamics in mesoporous TiO_2: Influence of dye sensitization and surface treatment in solid-state dye-sensitized solar cells", *J. Phys. Chem. C*, vol. 114, pp.1365-1371, 2010.

[19] M. Rawolle, M. A. Niedermeier, G. Kaune, *et al.*, "Fabrication and characterization of nanostructured titania films with integrated function from inorganic-organic hybrid materials", *Chem. Soc. Rev.*, vol. 41, pp.5131-5142, 2012.

[20] D. Grosso, G. J. de A. A. Soler-Illia, F. Babonneau, *et al.*, "Highly organized mesoporous titania thin films showing mono-oriented 2D hexagonal channels", *Adv. Mater.*, vol. 13, pp.1085-1090, 2001.

[21] S. Jang, J. S. Kang, J.-K. Lee, *et al.*, "Enhanced light harvesting in mesoscopic solar cells by multilevel multiscale patterned photoelectrodes with superpositioned optical properties", *Adv. Funct. Mater.*, vol. 26, pp.6584-6592, 2016.

[22] J. Kim, J. K. Koh, B. Kim, *et al.*, "Nanopatterning of mesoporous inorganic oxide films for efficient light harvesting of dye-sensitized solar cells", *Angew. Chem., Int. Ed.*, vol. 51, pp.6864-6869, 2012.

[23] M. A. Niedermeier, Gro, P. Müller-Buschbaum, "Structuring of titania thin films on different length scales via combining block copolymer assisted sol-gel templating with wet-imprinting", *J. Mater. Chem. A*, vol. 1, pp.13399-13403, 2013.

[24] M. A. Niedermeier, G. Tainter, B. Weiler, *et al.*, "Fabrication of hierarchically structured titania thin films via combining nano-imprint lithography with block copolymer assisted sol-gel templating", *J. Mater. Chem. A*, vol. 1, pp.7870-7873, 2013.

[25] M.-R. Ok, R. Ghosh, M. K. Brennaman, *et al.*, "Surface patterning of mesoporous niobium oxide films for solar energy conversion", *ACS Appl. Mater. Interfaces*, vol. 5, pp.3469-3474, 2013.

[26] S. Y. Heo, J. K. Koh, G. Kang, *et al.*, "Bifunctional moth-eye nanopatterned dye-sensitized solar cells: Light-harvesting and self-cleaning effects", *Adv. Energy Mater.*, vol. 4, 2014.

[27] S. Wooh, H. Yoon, J. H. Jung, *et al.*, "Efficient light harvesting with micropatterned 3D pyramidal photoanodes in dye-sensitized solar cells", *Adv. Mater.*, vol. 25, pp.3111-3116, 2013.

[28] S. Jang, S. M. Kang, M. Choi, "Multifunctional moth-eye TiO2/PDMS pads with high transmittance and uv filtering", *ACS Appl. Mater. Interfaces*, vol. 9, pp.44038-44044, 2017.

[29] F. E. Galvez, P. R. F. Barnes, J. Halme, *et al.*, "Dye sensitized solar cells as optically random photovoltaic media", *Energy Environ. Sci.*, vol. 7, pp.689-697, 2014.

[30] F. Z. Huang, D. H. Chen, X. L. Zhang, *et al.*, "Dual-function scattering layer of submicrometer-sized mesoporous TiO_2 beads for high-efficiency dye-sensitized solar cells", *Adv. Funct. Mater.*, vol. 20, pp.1301-1305, 2010.

[31] H. J. Koo, Y. J. Kim, Y. H. Lee, *et al.*, "Nano-embossed hollow spherical tio2 as bifunctional material for high-efficiency dye-sensitized solar cells", *Adv. Mater.*, vol. 20, pp.195-199, 2008.

[32] I. K. Ding, J. Zhu, W. Cai, *et al.*, "Plasmonic dye-sensitized solar cells", *Adv. Energy Mater.*, vol. 1, pp.52-57, 2011.

[33] X. Li, W. C. H. Choy, L. Huo, *et al.*, "Dual plasmonic nanostructures for high performance inverted organic solar cells", *Adv. Mater.*, vol. 24, pp.3046-3052, 2012.

[34] P. Reineck, G. P. Lee, D. Brick, *et al.*, "A solid-state plasmonic solar cell via metal nanoparticle self-assembly", *Adv. Mater.*, vol. 24, pp.4750-4755, 2012.

[35] K. Chan, M. Wright, N. Elumalai, *et al.*, "Plasmonics in organic and perovskite solar cells: Optical and electrical effects", *Advanced Optical Materials*, vol. 5, 2017.

[36] Q. Luo, C. Zhang, X. Deng, *et al.*, "Plasmonic effects of metallic nanoparticles on enhancing performance of perovskite solar cells", *ACS Appl. Mater. Interfaces*, vol. 9, pp.34821-34832, 2017.

[37] D. Xu, D. Liu, T. Xie, *et al.*, "Plasmon resonance scattering at perovskite $CH_3NH_3PbI_3$ coated single gold nanoparticles: evidence for electron transfer", *Chem. Commun.*, vol. 52, pp.9933-9936, 2016.

[38] B. Su, V. Körstgens, Y. Yao, *et al.*, "Pore size control of block copolymer-templated sol–gel-synthesized titania films deposited via spray coating", *J. Sol-Gel Sci. Technol.*, vol. 81, pp.346-354, 2017.

[39] B. Su, H. A. Caller-Guzman, V. Körstgens, *et al.*, "Macroscale and nanoscale morphology evolution during in situ spray coating of titania films for perovskite solar cells", *ACS Appl. Mater. Interfaces*, vol. 9, pp.43724-43732, 2017.

[40] M. Petrovic, T. Ye, C. Vijila, *et al.*, "Influence of charge transport and defects on the performance of planar and mesostructured perovskite solar cells", *Adv. Energy Mater.*, vol. 7, 2017.

[41] B. Roose, K. C. Gödel, S. Pathak, *et al.*, "Enhanced efficiency and stability of perovskite solar cells through Nd-doping of mesostructured TiO_2", *Adv. Energy Mater.*, vol. 6, pp.n/a-n/a, 2016.

[42] L. Schmidt-Mende, M. Grätzel, "TiO_2 pore-filling and its effect on the efficiency of solid-state dye-sensitized solar cells", *Thin Solid Films*, vol. 500, pp.296-301, 2006.

[43] V. Subramanian, E. E. Wolf, P. V. Kamat, "Catalysis with TiO_2/gold nanocomposites. Effect of metal particle size on the fermi level equilibration", *J. Am. Chem. Soc.*, vol. 126, pp.4943-4950, 2004.

[44] X. B. Chen, L. Liu, P. Y. Yu, *et al.*, "Increasing solar absorption for photocatalysis with black hydrogenated titanium dioxide nanocrystals", *Science*, vol. 331, pp.746-750, 2011.

[45] I. A. Al-Homoudi, J. S. Thakur, R. Naik, *et al.*, "Anatase TiO_2 films based co gas sensor: Film thickness, substrate and temperature effects", *Appl. Surf. Sci.*, vol. 253, pp.8607-8614, 2007.

[46] B. Karunagaran, P. Uthirakumar, S. J. Chung, *et al.*, "TiO_2 thin film gas sensor for monitoring ammonia", *Mater. Charact.*, vol. 58, pp.680-684, 2007.

[47] A. Navrotsky, J. C. Jamieson, O. J. Kleppa, "Enthalpy of transformation of a high-pressure polymorph of titanium dioxide to rutile modification", *Science*, vol. 158, pp.388-+, 1967.

[48] H. Zhang, J. F. Banfield, "Understanding polymorphic phase transformation behavior during growth of nanocrystalline aggregates: Insights from TiO_2", *J. Phys. Chem. B*, vol. 104, pp.3481-3487, 2000.

[49] X. Ye, J. Sha, Z. Jiao, *et al.*, "Thermoanalytical characteristic of nanocrystalline brookite-based titanium dioxide", *Nanostructured Materials*, vol. 8, pp.919-927, 1997.

[50] Y. Zhang, Z. Jiang, J. Huang, *et al.*, "Titanate and titania nanostructured materials for environmental and energy applications: a review", *RSC Adv.*, vol. 5, pp.79479-79510, 2015.

[51] T. Luttrell, S. Halpegamage, J. Tao, *et al.*, "Why is anatase a better photocatalyst than rutile? - Model studies on epitaxial TiO_2 films", *Sci. Rep.*, vol. 4, pp.4043, 2014.

[52] O. Carp, C. L. Huisman, A. Reller, "Photoinduced reactivity of titanium dioxide", *Progress in Solid State Chemistry*, vol. 32, pp.33-177, 2004.

[53] K. Tanaka, M. F. V. Capule, T. Hisanaga, "Effect of crystallinity of TiO_2 on its photocatalytic action", *Chem. Phys. Lett.*, vol. 187, pp.73-76, 1991.

[54] Y. Mi, Y. Weng, "Band alignment and controllable electron migration between rutile and anatase TiO_2", *Sci. Rep.*, vol. 5, pp.11482, 2015.

[55] P. Cheng, C. S. Deng, D. N. Liu, *et al.*, "Titania surface modification and photovoltaic characteristics with tungsten oxide", *Appl. Surf. Sci.*, vol. 254, pp.3391-3396, 2008.

[56] A. D. Jenkins, P. Kratochvil, R. F. T. Stepto, *et al.*, "Glossary of basic terms in polymer science", *Pure Appl. Chem.*, vol. 68, pp.2287-2311, 1996.

[57] F. S. BATES, "Polymer-polymer phase behavior", *Science*, vol. 251, pp.898-905, 1991.

[58] S. B. Darling, "Block copolymers for photovoltaics", *Energy Environ. Sci.*, vol. 2, pp.1266-1273, 2009.

[59] L. Leibler, "Theory of microphase separation in block copolymers", *Macromolecules*, vol. 13, pp.1602-1617, 1980.

[60] G. H. Fredrickson, E. Helfand, "Fluctuation effects in the theory of microphase separation in block copolymers", *The Journal of Chemical Physics*, vol. 87, pp.697-705, 1987.

[61] F. Meyers, A. J. Heeger, J. L. Brédas, "Fine tuning of the band gap in conjugated polymers via control of block copolymer sequences", *The Journal of Chemical Physics*, vol. 97, pp.2750-2758, 1992.

[62] X. L. Chen, S. A. Jenekhe, "Toward quantum-well nanostructures for exploring spatial confinement effects on electronic, optoelectronic, and optical phenomena", *Macromolecules*, vol. 29, pp.6189-6192, 1996.

[63] O. Hagemann, M. Jørgensen, F. C. Krebs, "Synthesis of an all-in-one molecule (for organic solar cells)", *The Journal of Organic Chemistry*, vol. 71, pp.5546-5559, 2006.

[64] F. C. Krebs, O. Hagemann, M. Jørgensen, "Synthesis of dye linked conducting block copolymers, dye linked conducting homopolymers and preliminary application to photovoltaics", *Sol. Energy Mater. Sol. Cells*, vol. 83, pp.211-228, 2004.

[65] A. Isakova, P. D. Topham, "Polymer strategies in perovskite solar cells", *Journal of Polymer Science Part B: Polymer Physics*, vol. 55, pp.549-568, 2017.

[66] J. I. Lee, S. H. Cho, S.-M. Park, *et al.*, "Highly aligned ultrahigh density arrays of conducting polymer nanorods using block copolymer templates", *Nano Lett.*, vol. 8, pp.2315-2320, 2008.

[67] S. Maria, A. S. Susha, M. Sommer, *et al.*, "Semiconductor block copolymer nanocomposites with lamellar morphology via self-organization", *Macromolecules*, vol. 41, pp.6081-6088, 2008.

[68] B. W. Boudouris, C. D. Frisbie, M. A. Hillmyer, "Nanoporous poly(3-alkylthiophene) thin films generated from block copolymer templates", *Macromolecules*, vol. 41, pp.67-75, 2008.

[69] M. Ebelmen, "Recherches sur les combinaisons Des acides borique et silicique avec les e'thers", *Ann. Chim. Phys.*, vol. 16, 1846.

[70] J. Gutierrez, A. Tercjak, I. Garcia, *et al.*, "Hybrid titanium dioxide/PS-*b*-PEO block copolymer nanocomposites based on sol-gel synthesis", *Nanotechnology*, vol. 19, pp.8, 2008.

[71] A. Hagfeldt, M. Grätzel, "Molecular photovoltaics", *Acc. Chem. Res.*, vol. 33, pp.269-277, 2000.

[72] P. R. F. Barnes, L. Liu, X. Li, *et al.*, "Re-evaluation of recombination losses in dye-sensitized cells: the failure of dynamic relaxation methods to correctly predict diffusion length in nanoporous photoelectrodes", *Nano Lett.*, vol. 9, pp.3532-3538, 2009.

[73] Q. Wang, S. Ito, M. Grätzel, *et al.*, "Characteristics of high efficiency dye-sensitized solar cells", *J. Phys. Chem. B*, vol. 110, pp.25210-25221, 2006.

[74] A. Hagfeldt, G. Boschloo, L. Sun, *et al.*, "Dye-sensitized solar cells", *Chem. Rev.*, vol. 110, pp.6595-6663, 2010.

[75] A. Hauch, A. Georg, "Diffusion in the electrolyte and charge-transfer reaction at the platinum electrode in dye-sensitized solar cells", *Electrochim. Acta*, vol. 46, pp.3457-3466, 2001.

[76] N. Papageorgiou, W. F. Maier, M. Gratzel, "An iodine/triiodide reduction electrocatalyst for aqueous and organic media", *J. Electrochem. Soc.*, vol. 144, pp.876-884, 1997.

[77] S. A. Haque, Y. Tachibana, D. R. Klug, *et al.*, "Charge recombination kinetics in dye-sensitized nanocrystalline titanium dioxide films under externally applied bias", *J. Phys. Chem. B*, vol. 102, pp.1745-1749, 1998.

[78] A. Zaban, M. Greenshtein, J. Bisquert, "Determination of the electron lifetime in nanocrystalline dye solar cells by open-circuit voltage decay measurements", *ChemPhysChem*, vol. 4, pp.859-864, 2003.

[79] V. Goldschmidt, "Crystal structure and chemical correlation", *Ber. Dtsch. Chem. Ges*, vol. 60, pp.1263-1296, 1927.

[80] C. Li, X. Lu, W. Ding, *et al.*, "Formability of ABX_3 (X = F, Cl, Br, I) halide perovskites", *Acta Crystallographica Section B*, vol. 64, pp.702-707, 2008.

[81] J. Shamsi, Z. Dang, P. Bianchini, *et al.*, "Colloidal synthesis of quantum confined single crystal $CsPbBr_3$ nanosheets with lateral size control up to the micrometer range", *J. Am. Chem. Soc.*, vol. 138, pp.7240-7243, 2016.

[82] L. Lv, Y. Xu, H. Fang, *et al.*, "Generalized colloidal synthesis of high-quality, two-dimensional cesium lead halide perovskite nanosheets and their applications in photodetectors", *Nanoscale*, vol. 8, pp.13589-13596, 2016.

[83] W. Geng, C.-J. Tong, Z.-K. Tang, *et al.*, "Effect of surface composition on electronic properties of methylammonium lead iodide perovskite", *Journal of Materiomics*, vol. 1, pp.213-220, 2015.

[84] V. A. Hintermayr, A. F. Richter, F. Ehrat, *et al.*, "Tuning the optical properties of perovskite nanoplatelets through composition and thickness by ligand-assisted exfoliation", *Adv. Mater.*, vol. 28, pp.9478-9485, 2016.

[85] C. C. Stoumpos, D. H. Cao, D. J. Clark, *et al.*, "Ruddlesden–popper hybrid lead iodide perovskite 2D homologous semiconductors", *Chem. Mater.*, vol. 28, pp.2852-2867, 2016.

[86] A. Swarnkar, A. R. Marshall, E. M. Sanehira, *et al.*, "Quantum dot–induced phase stabilization of α-$CsPbI_3$ perovskite for high-efficiency photovoltaics", *Science*, vol. 354, pp.92-95, 2016.

[87] G. Grancini, C. Roldán-Carmona, I. Zimmermann, *et al.*, "One-year stable perovskite solar cells by 2D/3D interface engineering", *Nat. Commun.*, vol. 8, pp.15684, 2017.

[88] H. Tsai, W. Nie, J.-C. Blancon, *et al.*, "High-efficiency two-dimensional Ruddlesden–Popper perovskite solar cells", *Nature*, vol. 536, pp.312-316, 2016.

[89] I. C. Smith, E. T. Hoke, D. Solis-Ibarra, *et al.*, "A layered hybrid perovskite solar-cell absorber with enhanced moisture stability", *Angew. Chem., Int. Ed.*, vol. 53, pp.11232-11235, 2014.

[90] A. Marchioro, J. Teuscher, D. Friedrich, *et al.*, "Unravelling the mechanism of photoinduced charge transfer processes in lead iodide perovskite solar cells", *Nat. Photonics*, vol. 8, pp.250-255, 2014.

[91] T. C. Sum, N. Mathews, "Advancements in perovskite solar cells: photophysics behind the photovoltaics", *Energy Environ. Sci.*, vol. 7, pp.2518-2534, 2014.

[92] Y. W. Li, L. Meng, Y. Yang, *et al.*, "High-efficiency robust perovskite solar cells on ultrathin flexible substrates", *Nat. Commun.*, vol. 7, pp.10, 2016.

[93] V. Gonzalez-Pedro, E. J. Juarez-Perez, W.-S. Arsyad, *et al.*, "General working principles of $CH_3NH_3PbX_3$ perovskite solar cells", *Nano Lett.*, vol. 14, pp.888-893, 2014.

[94] E. Edri, S. Kirmayer, A. Henning, *et al.*, "Why lead methylammonium tri-iodide perovskite-based solar cells require a mesoporous electron transporting scaffold (but not necessarily a hole conductor)", *Nano Lett.*, vol. 14, pp.1000-1004, 2014.

[95] H. K. Lin, Y. W. Su, H. C. Chen, *et al.*, "Block copolymer-tuned fullerene electron transport layer enhances the efficiency of perovskite photovoltaics", *ACS Appl. Mater. Interfaces*, vol. 8, pp.24603-24611, 2016.

[96] M. A. Green, A. Ho-Baillie, H. J. Snaith, "The emergence of perovskite solar cells", *Nat. Photonics*, vol. 8, pp.506-514, 2014.

[97] W. T. Doyle, "Optical properties of a suspension of metal spheres", *Phys. Rev. B*, vol. 39, pp.9852-9858, 1989.

[98] Q. Fu, W. Sun, "Mie theory for light scattering by a spherical particle in an absorbing medium", *Appl. Opt.*, vol. 40, pp.1354-1361, 2001.

[99] W. R. Erwin, H. F. Zarick, E. M. Talbert, *et al.*, "Light trapping in mesoporous solar cells with plasmonic nanostructures", *Energy Environ. Sci.*, vol. 9, pp.1577-1601, 2016.

[100] R. Lazzari, "IsGISAXS: A program for grazing-incidence small-angle x-ray scattering analysis of supported islands", *J. Appl. Crystallogr.*, vol. 35, pp.406-421, 2002.

[101] P. Müller-Buschbaum, "Grazing incidence small-angle X-ray scattering: an advanced scattering technique for the investigation of nanostructured polymer films", *Anal. Bioanal. Chem.*, vol. 376, pp.3-10, 2003.

[102] Y. Yoneda, "Anomalous surface reflection of X rays", *Phys. Rev.*, vol. 131, pp.2010-2013, 1963.

[103] J. L. Baker, L. H. Jimison, S. Mannsfeld, *et al.*, "Quantification of Thin Film Crystallographic Orientation Using X-ray Diffraction with an Area Detector", *Langmuir*, vol. 26, pp.9146-9151, 2010.

[104] Z. Jiang, "GIXSGUI: A MATLAB toolbox for grazing-incidence X-ray scattering data visualization and reduction, and indexing of buried three-dimensional periodic nanostructured films", *J. Appl. Crystallogr.*, vol. 48, pp.917-926, 2015.

[105] M. Yan, A. Gibaud, "On the intersection of grating truncation rods with the Ewald sphere studied by grazing-incidence small-angle X-ray scattering", *J. Appl. Crystallogr.*, vol. 40, pp.1050-1055, 2007.

[106] J. Wernecke, F. Scholze, M. Krumrey, "Direct structural characterisation of line gratings with grazing incidence small-angle X-ray scattering", *Rev. Sci. Instrum.*, vol. 83, pp.103906, 2012.

[107] D. R. Rueda, I. Martin-Fabiani, M. Soccio, *et al.*, "Grazing-incidence small-angle X-ray scattering of soft and hard nanofabricated gratings", *J. Appl. Crystallogr.*, vol. 45, pp.1038-1045, 2012.

[108] J. Choi, I. Gunkel, Y. Y. Li, *et al.*, "Macroscopically ordered hexagonal arrays by directed self-assembly of block copolymers with minimal topographic patterns", *Nanoscale*, vol. 9, pp.14888-14896, 2017.

[109] M. Jergel, P. Mikulík, E. Majková, *et al.*, "Structural characterization of lamellar multilayer gratings by X-ray reflectivity and scanning electron microscopy", *Journal of Physics D: Applied Physics*, vol. 32, pp.A220, 1999.

[110] D. Lübbert, T. Baumbach, S. Ponti, *et al.*, "Strain investigation of low strained buried gratings by grazing incidence X-ray diffraction and elasticity theory", *Europhys. Lett.*, vol. 46, pp.479-485, 1999.

[111] M. Pfluger, V. Soltwisch, J. Probst, *et al.*, "Grazing-incidence small-angle X-ray scattering (GISAXS) on small periodic targets using large beams", *Iucrj*, vol. 4, pp.431-438, 2017.

[112] D. Nečas, P. Klapetek, in *Open Physics*, Vol. 10, 2012, 181.

[113] K. M. Coakley, Y. Liu, M. D. McGehee, *et al.*, "Infiltrating semiconducting polymers into self-assembled mesoporous titania films for photovoltaic applications", *Adv. Funct. Mater.*, vol. 13, pp.301-306, 2003.

[114] P. Yang, D. Zhao, D. I. Margolese, *et al.*, "Generalized syntheses of large-pore mesoporous metal oxides with semicrystalline frameworks", *Nature*, vol. 396, pp.152-155, 1998.

[115] M. Templin, A. Franck, A. Du Chesne, *et al.*, "Organically modified aluminosilicate mesostructures from block copolymer phases", *Science*, vol. 278, pp.1795-1798, 1997.

[116] K. M. Coakley, M. D. McGehee, "Photovoltaic cells made from conjugated polymers infiltrated into mesoporous titania", *Appl. Phys. Lett.*, vol. 83, pp.3380-3382, 2003.

[117] Y.-J. Cheng, J. S. Gutmann, "Morphology phase diagram of ultrathin anatase TiO_2 films templated by by a single PS-*b*-PEO block copolymer", *J. Am. Chem. Soc.*, vol. 128, pp.4658-4674, 2006.

[118] E. A. Barringer, H. K. Bowen, "High-purity, monodisperse TiO2 powders by hydrolysis of titanium tetraethoxide. 1. Synthesis and physical properties", *Langmuir*, vol. 1, pp.414-420, 1985.

[119] J. H. Jean, T. A. Ring, "Nucleation and growth of monosized titania powders from alcohol solution", *Langmuir*, vol. 2, pp.251-255, 1986.

[120] D. O. Scanlon, C. W. Dunnill, J. Buckeridge, *et al.*, "Band alignment of rutile and anatase TiO_2", *Nat. Mater.*, vol. 12, pp.798-801, 2013.

[121] K. A. Bush, A. F. Palmstrom, Z. J. Yu, *et al.*, "23.6%-efficient monolithic perovskite/silicon tandem solar cells with improved stability", *Nature Energy*, vol. 2, pp.17009, 2017.

[122] M. K. Nazeeruddin, R. Humphry-Baker, P. Liska, *et al.*, "Investigation of sensitizer adsorption and the influence of protons on current and voltage of a dye-sensitized nanocrystalline TiO_2 solar cell", *J. Phys. Chem. B*, vol. 107, pp.8981-8987, 2003.

[123] M. K. Nazeeruddin, S. M. Zakeeruddin, R. Humphry-Baker, *et al.*, "Acid−base equilibria of (2,2‘-bipyridyl-4,4‘-dicarboxylic acid)ruthenium(ii) complexes and the effect of protonation on charge-transfer sensitization of nanocrystalline titania", *Inorg Chem*, vol. 38, pp.6298-6305, 1999.

[124] T. Horiuchi, H. Miura, K. Sumioka, *et al.*, "High efficiency of dye-sensitized solar cells based on metal-free indoline dyes", *J. Am. Chem. Soc.*, vol. 126, pp.12218-12219, 2004.

[125] D. W. Schubert, T. Dunkel, "Spin coating from a molecular point of view: its concentration regimes, influence of molar mass and distribution", *Materials Research Innovations*, vol. 7, pp.314-321, 2003.

[126] I. J. Kramer, J. C. Minor, G. Moreno-Bautista, *et al.*, "Efficient spray-coated colloidal quantum dot solar cells", *Adv. Mater.*, vol. 27, pp.116-121, 2015.

[127] A. Abdellah, K. S. Virdi, R. Meier, *et al.*, "Successive spray deposition of P3HT/PCBM organic photoactive layers: material composition and device characteristics", *Adv. Funct. Mater.*, vol. 22, pp.4078-4086, 2012.

[128] H. Choi, J. G. Lee, X. D. Mai, *et al.*, "Supersonically spray-coated colloidal quantum dot ink solar cells", *Sci. Rep.*, vol. 7, pp.8, 2017.

[129] C. Zhang, C. J. Li, H. Liao, *et al.*, "Effect of in-flight particle velocity on the performance of plasma-sprayed YSZ electrolyte coating for solid oxide fuel cells", *Surface & Coatings Technology*, vol. 202, pp.2654-2660, 2008.

[130] R. C. Ambare, S. R. Bharadwaj, B. J. Lokhande, "Electrochemical characterization of Mn: Co3O4 thin films prepared by spray pyrolysis via aqueous route", *Current Applied Physics*, vol. 14, pp.1582-1590, 2014.

[131] R. Xiang, H. Zeng, Y. Su, *et al.*, "Spray coating as a simple method to prepare catalyst for growth of diameter-tunable single-walled carbon nanotubes", *Carbon*, vol. 64, pp.537-540, 2013.

[132] N. T. Hahn, S. Hoang, J. L. Self, *et al.*, "Spray pyrolysis deposition and photoelectrochemical properties of n-type BiOI nanoplatelet thin films", *ACS Nano*, vol. 6, pp.7712-7722, 2012.

[133] O. Assad, A. M. Leshansky, B. Wang, *et al.*, "Spray-Coating Route for Highly Aligned and Large-Scale Arrays of Nanowires", *ACS Nano*, vol. 6, pp.4702-4712, 2012.

[134] A. Falco, L. Cina, G. Scarpa, *et al.*, "Fully-sprayed and flexible organic photodiodes with transparent carbon nanotube electrodes", *ACS Appl. Mater. Interfaces*, vol. 6, pp.10593-10601, 2014.

[135] H. Yu, S. Zhang, H. Zhao, *et al.*, "An efficient and low-cost TiO_2 compact layer for performance improvement of dye-sensitized solar cells", *Electrochim. Acta*, vol. 54, pp.1319-1324, 2009.

[136] S. Ito, T. N. Murakami, P. Comte, *et al.*, "Fabrication of thin film dye sensitized solar cells with solar to electric power conversion efficiency over 10%", *Thin Solid Films*, vol. 516, pp.4613-4619, 2008.

[137] S. Ito, P. Liska, P. Comte, *et al.*, "Control of dark current in photoelectrochemical (TiO_2/I^--I_3^-) and dye-sensitized solar cells", *Chem. Commun.*, vol., pp.4351-4353, 2005.

[138] A. M. A. Leguy, Y. Hu, M. Campoy-Quiles, *et al.*, "Reversible hydration of $CH_3NH_3PbI_3$ in films, single crystals, and solar cells", *Chem. Mater.*, vol. 27, pp.3397-3407, 2015.

[139] M. Rawolle, M. A. Ruderer, S. M. Prams, *et al.*, "Nanostructuring of titania thin films by a combination of microfluidics and block-copolymer-based sol–gel templating", *Small*, vol. 7, pp.884-891, 2011.

[140] J. Burschka, A. Dualeh, F. Kessler, *et al.*, "Tris(2-(1h-pyrazol-1-yl)pyridine)cobalt(III) as p-type dopant for organic semiconductors and its application in highly efficient solid-state dye-sensitized solar cells", *J. Am. Chem. Soc.*, vol. 133, pp.18042-18045, 2011.

[141] D. Bi, W. Tress, M. I. Dar, *et al.*, "Efficient luminescent solar cells based on tailored mixed-cation perovskites", *Sci. Adv.*, vol. 2, pp.e1501170, 2016.

[142] L.-M. Chen, Z. Hong, W. L. Kwan, *et al.*, "Multi-source/component spray coating for polymer solar cells", *ACS Nano*, vol. 4, pp.4744-4752, 2010.

[143] D. Vak, S.-S. Kim, J. Jo, *et al.*, "Fabrication of organic bulk heterojunction solar cells by a spray deposition method for low-cost power generation", *Appl. Phys. Lett.*, vol. 91, pp.081102, 2007.

[144] J. Krantz, T. Stubhan, M. Richter, *et al.*, "Spray-coated silver nanowires as top electrode layer in semitransparent P3HT:PCBM-based organic solar cell devices", *Adv. Funct. Mater.*, vol. 23, pp.1711-1717, 2013.

[145] K. Sarkar, E. V. Braden, S. Pogorzalek, *et al.*, "Monitoring structural dynamics of in situ spray-deposited zinc oxide films for application in dye-sensitized solar cells", *ChemSusChem*, vol. 7, pp.2140-2145, 2014.

[146] J. H. Noh, S. H. Im, J. H. Heo, *et al.*, "Chemical management for colorful, efficient, and stable inorganic–organic hybrid nanostructured solar cells", *Nano Lett.*, vol. 13, pp.1764-1769, 2013.

[147] Y. Deng, Y. Cai, Z. Sun, *et al.*, "Multifunctional mesoporous composite microspheres with well-designed nanostructure: A highly integrated catalyst system", *J. Am. Chem. Soc.*, vol. 132, pp.8466-8473, 2010.

[148] J. Nisar, Z. Topalian, A. De Sarkar, *et al.*, "TiO_2-based gas sensor: A possible application to SO_2", *ACS Appl. Mater. Interfaces*, vol. 5, pp.8516-8522, 2013.

[149] Y. Liu, J. Li, B. Zhou, *et al.*, "A TiO_2-nanotube-array-based photocatalytic fuel cell using refractory organic compounds as substrates for electricity generation", *Chem. Commun.*, vol. 47, pp.10314-10316, 2011.

[150] J. A. Chang, J. H. Rhee, S. H. Im, *et al.*, "High-performance nanostructured inorganic-organic heterojunction solar cells", *Nano Lett.*, vol. 10, pp.2609-2612, 2010.

[151] J.-F. Lin, W.-B. Wang, C.-C. Ho, *et al.*, "Enhancing P3HT/TiO_2 hybrid photovoltaic performance by incorporating high surface potential silica nanodots into hole transport layer", *J. Phys. Chem. C*, vol. 116, pp.1955-1960, 2011.

[152] L. Martinez, S. Higuchi, A. J. MacLachlan, *et al.*, "Improved electronic coupling in hybrid organic-inorganic nanocomposites employing thiol-functionalized P3HT and bismuth sulfide nanocrystals", *Nanoscale*, vol. 6, pp.10018-10026, 2014.

[153] H. J. Snaith, A. J. Moule, C. Klein, *et al.*, "Efficiency enhancements in solid-state hybrid solar cells via reduced charge recombination and increased light capture", *Nano Lett.*, vol. 7, pp.3372-3376, 2007.

[154] M. Kettunen, R. J. Silvennoinen, N. Houbenov, *et al.*, "Photoswitchable superabsorbency based on nanocellulose aerogels", *Adv. Funct. Mater.*, vol. 21, pp.510-517, 2011.

[155] M. V. Baryshnikova, L. A. Filatov, A. S. Petrov, *et al.*, "CVD deposited titania thin films for gas sensors with improved operating characteristics", *Chemical Vapor Deposition*, vol. 21, pp.327-333, 2015.

[156] M. Nomura, B. Meester, J. Schoonman, *et al.*, "Improvement of thermal stability of porous titania films prepared by electrostatic sol-spray deposition (ESSD)", *Chem. Mater.*, vol. 15, pp.1283-1288, 2003.

[157] J. M. Szeifert, D. Fattakhova-Rohlfing, D. Georgiadou, *et al.*, ""Brick and mortar” strategy for the formation of highly crystalline mesoporous titania films from nanocrystalline building blocks", *Chem. Mater.*, vol. 21, pp.1260-1265, 2009.

[158] G. K. Mor, O. K. Varghese, M. Paulose, *et al.*, "A review on highly ordered, vertically oriented TiO_2 nanotube arrays: Fabrication, material properties, and solar energy applications", *Sol. Energy Mater. Sol. Cells*, vol. 90, pp.2011-2075, 2006.

[159] P. Roy, S. Berger, P. Schmuki, "TiO_2 nanotubes: Synthesis and applications", *Angew. Chem., Int. Ed.*, vol. 50, pp.2904-2939, 2011.

[160] J. Weickert, C. Palumbiny, M. Nedelcu, *et al.*, "Controlled growth of TiO_2 nanotubes on conducting glass", *Chem. Mater.*, vol. 23, pp.155-162, 2011.

[161] M. H. Kim, J. M. Baik, J. P. Zhang, *et al.*, "TiO_2 nanowire growth driven by phosphorus-doped nanocatalysis", *J. Phys. Chem. C*, vol. 114, pp.10697-10702, 2010.

[162] E. L. Crepaldi, G. J. d. A. A. Soler-Illia, D. Grosso, *et al.*, "Controlled formation of highly organized mesoporous titania thin films: From mesostructured hybrids to mesoporous nanoanatase TiO_2", *J. Am. Chem. Soc.*, vol. 125, pp.9770-9786, 2003.

[163] M. C. Orilall, U. Wiesner, "Block copolymer based composition and morphology control in nanostructured hybrid materials for energy conversion and storage: Solar cells, batteries", *Chem. Soc. Rev.*, vol. 40, pp.520-535, 2011.

[164] Y. J. Cheng, S. Y. Zhou, M. Wolkenhauer, *et al.*, "Effect of sol-gel reaction time on the morphology transition in mesoporous titania/PS-*b*-PEO composite films", *Sci. Adv. Mater.*, vol. 7, pp.924-933, 2015.

[165] J. Veliscek-Carolan, R. Knott, T. Hanley, "Effects of precursor solution aging and other parameters on synthesis of ordered mesoporous titania powders", *J. Phys. Chem. C*, vol. 119, pp.7172-7183, 2015.

[166] S. Sokolov, E. Ortel, R. Kraehnert, "Mesoporous titania films with adjustable pore size coated on stainless steel substrates", *Mater. Res. Bull.*, vol. 44, pp.2222-2227, 2009.

[167] A. M. E. Raj, V. Agnes, V. Bena Jothy, *et al.*, "Spray deposition and property analysis of anatase phase titania (TiO_2) nanostructures", *Thin Solid Films*, vol. 519, pp.129-135, 2010.

[168] L. Song, W. Wang, V. Körstgens, *et al.*, "Spray deposition of titania films with incorporated crystalline nanoparticles for all-solid-state dye-sensitized solar cells using P3HT", *Adv. Funct. Mater.*, vol. 26, pp.1498-1506, 2016.

[169] P. Müller-Buschbaum, "The active layer morphology of organic solar cells probed with grazing incidence scattering techniques", *Adv. Mater.*, vol. 26, pp.7692-7709, 2014.

[170] Z. Sun, J. H. Kim, Y. Zhao, *et al.*, "Morphology-controllable 1D-3D nanostructured TiO_2 bilayer photoanodes for dye-sensitized solar cells", *Chem. Commun.*, vol. 49, pp.966-968, 2013.

[171] J.-Y. Liao, J.-W. He, H. Xu, *et al.*, "Effect of TiO_2 morphology on photovoltaic performance of dye-sensitized solar cells: nanoparticles, nanofibers, hierarchical spheres and ellipsoid spheres", *J. Mater. Chem.*, vol. 22, pp.7910-7918, 2012.

[172] P. Müller-Buschbaum, "Influence of surface cleaning on dewetting of thin polystyrene films", *Eur. Phys. J. E*, vol. 12, pp.443-448, 2003.

[173] J. Perlich, L. Schulz, M. M. Abul Kashem, *et al.*, "Modification of the morphology of P(S-*b*-EO) templated thin TiO_2 films by swelling with PS homopolymer", *Langmuir*, vol. 23, pp.10299-10306, 2007.

[174] G. Kaune, W. Wang, E. Metwalli, *et al.*, "Layered TiO_2: PVK nano-composite thin films for photovoltaic applications", *Eur. Phys. J. E*, vol. 26, pp.73-79, 2008.

[175] M. Rawolle, K. Sarkar, M. A. Niedermeier, *et al.*, "Infiltration of polymer hole-conductor into mesoporous titania structures for solid-state dye-sensitized solar cells", *ACS Appl. Mater. Interfaces*, vol. 5, pp.719-729, 2013.

[176] K. Sarkar, M. Rawolle, M. A. Niedermeier, *et al.*, "A quantitative approach to tune metal oxide network morphology based on grazing-incidence small-angle X-ray scattering investigations", *J. Appl. Crystallogr.*, vol. 47, pp.76-83, 2014.

[177] J. Pan, G. Liu, G. Q. Lu, *et al.*, "On the true photoreactivity order of {001}, {010}, and {101} facets of anatase TiO_2 crystals", *Angew. Chem., Int. Ed.*, vol. 50, pp.2133-2137, 2011.

[178] J.-W. Shiu, C.-M. Lan, Y.-C. Chang, *et al.*, "Size-controlled anatase titania single crystals with octahedron-like morphology for dye-sensitized solar cells", *ACS Nano*, vol. 6, pp.10862-10873, 2012.

[179] A. Kojima, K. Teshima, Y. Shirai, *et al.*, "Organometal halide perovskites as visible-light sensitizers for photovoltaic cells", *J. Am. Chem. Soc.*, vol. 131, pp.6050-6051, 2009.

[180] S. Aharon, S. Gamliel, B. E. Cohen, *et al.*, "Depletion region effect of highly efficient hole conductor free $CH_3NH_3PbI_3$ perovskite solar cells", *Phys. Chem. Chem. Phys.*, vol. 16, pp.10512-10518, 2014.

[181] Y. Zhao, A. M. Nardes, K. Zhu, "Solid-state mesostructured perovskite $CH_3NH_3PbI_3$ solar cells: Charge transport, recombination, and diffusion length", *J. Phys. Chem. Lett.*, vol. 5, pp.490-494, 2014.

[182] H.-S. Kim, N.-G. Park, "Parameters affecting i–v hysteresis of $CH_3NH_3PbI_3$ perovskite solar cells: Effects of perovskite crystal size and mesoporous TiO_2 layer", *J. Phys. Chem. Lett.*, vol. 5, pp.2927-2934, 2014.

[183] J. J. Choi, X. Yang, Z. M. Norman, *et al.*, "Structure of methylammonium lead iodide within mesoporous titanium dioxide: Active material in high-performance perovskite solar cells", *Nano Lett.*, vol. 14, pp.127-133, 2014.

[184] M. Abdi-Jalebi, M. I. Dar, A. Sadhanala, *et al.*, "Impact of a mesoporous titania–perovskite interface on the performance of hybrid organic–inorganic perovskite solar cells", *J. Phys. Chem. Lett.*, vol. 7, pp.3264-3269, 2016.

[185] A. Listorti, E. J. Juarez-Perez, C. Frontera, *et al.*, "Effect of mesostructured layer upon crystalline properties and device performance on perovskite solar cells", *J. Phys. Chem. Lett.*, vol. 6, pp.1628-1637, 2015.

[186] M. Ibrahim Dar, M. Abdi-Jalebi, N. Arora, *et al.*, "Understanding the impact of bromide on the photovoltaic performance of $CH_3NH_3PbI_3$ solar cells", *Adv. Mater.*, vol. 27, pp.7221-7228, 2015.

[187] W. Kim, S. Y. Choi, Y. M. Jeon, *et al.*, "Highly ordered, hierarchically porous TiO_2 films via combination of two self-assembling templates", *ACS Appl. Mater. Interfaces*, vol. 6, pp.11484-11492, 2014.

[188] S. H. Kim, M. J. Misner, T. Xu, *et al.*, "Highly oriented and ordered arrays from block copolymers via solvent evaporation", *Adv. Mater.*, vol. 16, pp.226-231, 2004.

[189] F. H. Schacher, P. A. Rupar, I. Manners, "Functional block copolymers: Nanostructured materials with emerging applications", *Angew. Chem., Int. Ed.*, vol. 51, pp.7898-7921, 2012.

[190] J. Perlich, M. Memesa, A. Diethert, *et al.*, "Preservation of the morphology of a self-encapsulated thin titania film in a functional multilayer stack: An X-ray scattering study", *ChemPhysChem*, vol. 10, pp.799-805, 2009.

[191] A. Sarkar, N. J. Jeon, J. H. Noh, *et al.*, "Well-organized mesoporous tio2 photoelectrodes by block copolymer-induced sol–gel assembly for inorganic–organic hybrid perovskite solar cells", *J. Phys. Chem. C*, vol. 118, pp.16688-16693, 2014.

[192] C.-C. Chung, C. S. Lee, E. Jokar, *et al.*, "Well-organized mesoporous tio2 photoanode by using amphiphilic graft copolymer for efficient perovskite solar cells", *J. Phys. Chem. C*, vol. 120, pp.9619-9627, 2016.

[193] M. Zukalová, A. Zukal, L. Kavan, *et al.*, "Organized mesoporous TiO_2 films exhibiting greatly enhanced performance in dye-sensitized solar cells", *Nano Lett.*, vol. 5, pp.1789-1792, 2005.

[194] S. Guldin, P. Docampo, M. Stefik, *et al.*, "Layer-by-layer formation of block-copolymer-derived TiO_2 for solid-state dye-sensitized solar cells", *Small*, vol. 8, pp.432-440, 2012.

[195] P. Docampo, M. Stefik, S. Guldin, *et al.*, "Triblock-terpolymer-directed self-assembly of mesoporous TiO_2: High-performance photoanodes for solid-state dye-sensitized solar cells", *Adv. Energy Mater.*, vol. 2, pp.676-682, 2012.

[196] K. W. Tan, D. T. Moore, M. Saliba, *et al.*, "Thermally induced structural evolution and performance of mesoporous block copolymer-directed alumina perovskite solar cells", *ACS Nano*, vol. 8, pp.4730-4739, 2014.

[197] J. N. Hart, D. Menzies, Y.-B. Cheng, *et al.*, "TiO_2 sol–gel blocking layers for dye-sensitized solar cells", *C. R. Chim.*, vol. 9, pp.622-626, 2006.

[198] Y. Chiba, A. Islam, Y. Watanabe, *et al.*, "Dye-sensitized solar cells with conversion efficiency of 11.1%", *Jpn. J. Appl. Phys., Part 2*, vol. 45, pp.L638-L640, 2006.

[199] S. V. Roth, "A deep look into the spray coating process in real-time-the crucial role of X-rays", *J. Phys.: Condens. Matter*, vol. 28, pp.37, 2016.

[200] C. Frank, J. Novak, R. Banerjee, *et al.*, "Island size evolution and molecular diffusion during growth of organic thin films followed by time-resolved specular and off-specular scattering", *Phys. Rev. B*, vol. 90, pp.6, 2014.

[201] L. Filipovic, S. Selberherr, G. C. Mutinati, *et al.*, "Methods of simulating thin film deposition using spray pyrolysis techniques", *Microelectron. Eng.*, vol. 117, pp.57-66, 2014.

[202] L. Amirav, E. Lifshitz, "A spray-based technique for the production of mns thin films", *ChemPhysChem*, vol. 16, pp.353-359, 2015.

[203] S. A. Schwartz, G. A. Meyer, "Characterization of aerosols generated by thermospray nebulization for atomic spectroscopy", *Spectrochim. Acta, Part B*, vol. 41, pp.1287-1298, 1986.

[204] J. A. Koropchak, D. H. Winn, "Fundamental characteristics of thermospray aerosols and sample introduction for atomic spectrometry", *Appl. Spectmsc.*, vol. 41, pp.1311-1318, 1987.

[205] S. M. Kang, S. Jang, J.-K. Lee, *et al.*, "Moth-eye TiO_2 layer for improving light harvesting efficiency in perovskite solar cells", *Small*, vol. 12, pp.2443-2449, 2016.

[206] J. H. Lee, J. Kim, T. Y. Kim, *et al.*, "All-in-one energy harvesting and storage devices", *J. Mater. Chem. A*, vol. 4, pp.7983-7999, 2016.

[207] J. S. Kang, J. Lim, W. Y. Rho, *et al.*, "Wrinkled silica/titania nanoparticles with tunable interwrinkle distances for efficient utilization of photons in dye-sensitized solar cells", *Sci. Rep.*, vol. 6, pp.14, 2016.

[208] S. Carretero-Palacios, A. Jiménez-Solano, H. Míguez, "Plasmonic nanoparticles as light-harvesting enhancers in perovskite solar cells: A user’s guide", *ACS Energy Lett.*, vol. 1, pp.323-331, 2016.

[209] A. Usami, "Theoretical study of application of multiple scattering of light to a dye-sensitized nanocrystalline photoelectrichemical cell", *Chem. Phys. Lett.*, vol. 277, pp.105-108, 1997.

[210] S. Foster, S. John, "Light-trapping in dye-sensitized solar cells", *Energy Environ. Sci.*, vol. 6, pp.2972-2983, 2013.

[211] L. I. Halaoui, N. M. Abrams, T. E. Mallouk, "Increasing the conversion efficiency of dye-sensitized TiO_2 photoelectrochemical cells by coupling to photonic crystals", *J. Phys. Chem. B*, vol. 109, pp.6334-6342, 2005.

[212] S. Colodrero, A. Mihi, L. Häggman, *et al.*, "Porous one-dimensional photonic crystals improve the power-conversion efficiency of dye-sensitized solar cells", *Adv. Mater.*, vol. 21, pp.764-770, 2009.

[213] S. Guldin, S. Hüttner, M. Kolle, *et al.*, "Dye-sensitized solar cell based on a three-dimensional photonic crystal", *Nano Lett.*, vol. 10, pp.2303-2309, 2010.

[214] W. Zhang, M. Saliba, S. D. Stranks, *et al.*, "Enhancement of perovskite-based solar cells employing core–shell metal nanoparticles", *Nano Lett.*, vol. 13, pp.4505-4510, 2013.

[215] E. S. Arinze, B. Qiu, G. Nyirjesy, *et al.*, "Plasmonic Nanoparticle Enhancement of Solution-Processed Solar Cells: Practical Limits and Opportunities", *ACS Photonics*, vol. 3, pp.158-173, 2016.

[216] A. Chutinan, S. John, "Light trapping and absorption optimization in certain thin-film photonic crystal architectures", *Phys. Rev. A*, vol. 78, pp.023825, 2008.

[217] T. Pfadler, M. Coric, C. M. Palumbiny, *et al.*, "Influence of interfacial area on exciton separation and polaron recombination in nanostructured bilayer all-polymer solar cells", *ACS Nano*, vol. 8, pp.12397-12409, 2014.

[218] C.-C. Chen, W.-H. Chang, K. Yoshimura, *et al.*, "An efficient triple-junction polymer solar cell having a power conversion efficiency exceeding 11%", *Adv. Mater.*, vol. 26, pp.5670-5677, 2014.

[219] M. A. Niedermeier, *Novel structuring routines of titania films for application in photovoltaics*,Ph.D. Thesis,Technische Universität München,München,2013.

[220] R. J. Sutton, G. E. Eperon, L. Miranda, *et al.*, "Bandgap-tunable cesium lead halide perovskites with high thermal stability for efficient solar cells", *Adv. Energy Mater.*, vol. 6, pp.n/a-n/a, 2016.

[221] B. Conings, J. Drijkoningen, N. Gauquelin, *et al.*, "Intrinsic thermal instability of methylammonium lead trihalide perovskite", *Adv. Energy Mater.*, vol. 5, pp.n/a-n/a, 2015.

[222] Y. Wu, F. Xie, H. Chen, *et al.*, "Thermally stable $MAPbI_3$ perovskite solar cells with efficiency of 19.19% and area over 1 cm^2 achieved by additive engineering", *Adv. Mater.*, vol. 29, pp.1701073, 2017.

[223] J. Cui, C. Chen, J. Han, *et al.*, "Surface plasmon resonance effect in inverted perovskite solar cells", *Advanced Science*, vol. 3, pp.n/a-n/a, 2016.

[224] M. Saliba, W. Zhang, V. M. Burlakov, *et al.*, "Plasmonic-induced photon recycling in metal halide perovskite solar cells", *Adv. Funct. Mater.*, vol. 25, pp.5038-5046, 2015.

[225] Z. Yuan, Z. Wu, S. Bai, *et al.*, "Hot-electron injection in a sandwiched TiO_x–Au–TiO_x structure for high-performance planar perovskite solar cells", *Adv. Energy Mater.*, vol. 5, pp.n/a-n/a, 2015.

[226] S. S. Mali, C. S. Shim, H. Kim, *et al.*, "In situ processed gold nanoparticle-embedded TiO_2 nanofibers enabling plasmonic perovskite solar cells to exceed 14% conversion efficiency", *Nanoscale*, vol. 8, pp.2664-2677, 2016.

[227] V. Soltwisch, A. F. Herrero, M. Pfluger, *et al.*, "Reconstructing detailed line profiles of lamellar gratings from GISAXS patterns with a Maxwell solver", *J. Appl. Crystallogr.*, vol. 50, pp.1524-1532, 2017.

[228] V. Soltwisch, A. Haase, J. Wernecke, *et al.*, "Correlated diffuse X-ray scattering from periodically nanostructured surfaces", *Phys. Rev. B*, vol. 94, 2016.

[229] P. Ayyub, V. R. Palkar, S. Chattopadhyay, *et al.*, "Effect of crystal size reduction on lattice symmetry and cooperative properties", *Phys. Rev. B*, vol. 51, pp.6135-6138, 1995.

[230] J.-F. Wang, L. Zhu, B.-G. Zhao, *et al.*, "Surface engineering of perovskite films for efficient solar cells", *Sci. Rep.*, vol. 7, pp.14478, 2017.

[231] C. Xiao, Z. Li, H. Guthrey, *et al.*, "Mechanisms of electron-beam-induced damage in perovskite thin films revealed by cathodoluminescence spectroscopy", *J. Phys. Chem. C*, vol. 119, pp.26904-26911, 2015.

[232] H. F. Yuan, E. Debroye, K. Janssen, *et al.*, "Degradation of methylammonium lead iodide perovskite structures through light and electron beam driven ion migration", *J. Phys. Chem. Lett.*, vol. 7, pp.561-566, 2016.

[233] K. Miyata, D. Meggiolaro, M. T. Trinh, *et al.*, "Large polarons in lead halide perovskites", *Sci. Adv.*, vol. 3, 2017.

[234] C. Wang, B. R. Ecker, H. Wei, *et al.*, "Environmental degradation of $MAPbBr_3$ single crystal: More unstable than expected", *J. Phys. Chem. C*, vol., 2018.

[235] S. Pathak, N. Sakai, F. Wisnivesky Rocca Rivarola, *et al.*, "Perovskite crystals for tunable white light emission", *Chem. Mater.*, vol. 27, pp.8066-8075, 2015.

[236] J. A. Sichert, Y. Tong, N. Mutz, *et al.*, "Quantum size effect in organometal halide perovskite nanoplatelets", *Nano Lett.*, vol. 15, pp.6521-6527, 2015.

[237] P. Tyagi, S. M. Arveson, W. A. Tisdale, "Colloidal organohalide perovskite nanoplatelets exhibiting quantum confinement", *J. Phys. Chem. Lett.*, vol. 6, pp.1911-1916, 2015.

[238] B.-E. Cohen, M. Wierzbowska, L. Etgar, "High efficiency quasi 2D lead bromide perovskite solar cells using various barrier molecules", *Sustainable Energy & Fuels*, vol. 1, pp.1935-1943, 2017.

[239] N. Wang, L. Cheng, R. Ge, *et al.*, "Perovskite light-emitting diodes based on solution-processed self-organized multiple quantum wells", *Nat. Photonics*, vol. advance online publication, 2016.

[240] G. C. Papavassiliou, I. B. Koutselas, "Structural, optical and related properties of some natural three- and lower-dimensional semiconductor systems", *Synthetic Metals*, vol. 71, pp.1713-1714, 1995.

[241] T. Kenichiro, T. Takayuki, K. Takashi, *et al.*, "Electronic and excitonic structures of inorganic–organic perovskite-type quantum-well crystal $(C_4H_9NH_3)_2PbBr_4$", *Jpn. J. Appl. Phys.*, vol. 44, pp.5923, 2005.

[242] M. D. Smith, A. Jaffe, E. R. Dohner, *et al.*, "Structural origins of broadband emission from layered Pb-Br hybrid perovskites", *Chemical Science*, vol. 8, pp.4497-4504, 2017.

[243] C. Huo, B. Cai, Z. Yuan, *et al.*, "Two-dimensional metal halide perovskites: Theory, synthesis, and optoelectronics", *Small Methods*, vol. 1, pp.1600018-n/a, 2017.

[244] R. Wang, Y. Tong, A. Manzi, *et al.*, "Preferential orientation of crystals induced by incorporation of organic ligands in mixed-dimensional hybrid perovskite films", *Advanced Optical Materials*, vol., 2018.

[245] I. Jeong, Y. H. Park, S. Bae, *et al.*, "Solution-processed ultrathin tio2 compact layer hybridized with mesoporous TiO_2 for high-performance perovskite solar cells", *ACS Appl. Mater. Interfaces*, vol. 9, pp.36865-36874, 2017.

[246] S. Kumar, J. Jagielski, S. Yakunin, *et al.*, "Efficient blue electroluminescence using quantum-confined two-dimensional perovskites", *ACS Nano*, vol. 10, pp.9720-9729, 2016.

[247] H. A. Atwater, A. Polman, "Plasmonics for improved photovoltaic devices", *Nat. Mater.*, vol. 9, pp.205-213, 2010.

[248] X. Wen, R. Sheng, A. W. Y. Ho-Baillie, *et al.*, "Morphology and carrier extraction study of organic–inorganic metal halide perovskite by one- and two-photon fluorescence microscopy", *J. Phys. Chem. Lett.*, vol. 5, pp.3849-3853, 2014.

[249] D. W. deQuilettes, S. M. Vorpahl, S. D. Stranks, *et al.*, "Impact of microstructure on local carrier lifetime in perovskite solar cells", *Science*, vol., 2015.

[250] D. Kiermasch, P. Rieder, K. Tvingstedt, *et al.*, "Improved charge carrier lifetime in planar perovskite solar cells by bromine doping", *Sci. Rep.*, vol. 6, pp.39333, 2016.

[251] N. Giesbrecht, J. Schlipf, L. Oesinghaus, *et al.*, "Synthesis of perfectly oriented and micrometer-sized $MAPbBr_3$ perovskite crystals for thin-film photovoltaic applications", *ACS Energy Lett.*, vol., pp.150-154, 2016.

[252] X. Zhang, X. Ren, B. Liu, *et al.*, "Stable high efficiency two-dimensional perovskite solar cells via cesium doping", *Energy Environ. Sci.*, vol. 10, pp.2095-2102, 2017.

[253] Y. Shao, Y. Yuan, J. Huang, "Correlation of energy disorder and open-circuit voltage in hybrid perovskite solar cells", *Nature Energy*, vol. 1, pp.15001, 2016.

[254] J. M. Frost, K. T. Butler, F. Brivio, *et al.*, "Atomistic origins of high-performance in hybrid halide perovskite solar cells", *Nano Lett.*, vol. 14, pp.2584-2590, 2014.

[255] W. Z. Li, H. P. Dong, L. D. Wang, *et al.*, "Montmorillonite as bifunctional buffer layer material for hybrid perovskite solar cells with protection from corrosion and retarding recombination", *J. Mater. Chem. A*, vol. 2, pp.13587-13592, 2014.

[256] D. H. Cao, C. C. Stoumpos, O. K. Farha, *et al.*, "2D homologous perovskites as light-absorbing materials for solar cell applications", *J. Am. Chem. Soc.*, vol. 137, pp.7843-7850, 2015.

[257] M. Yuan, M. Liu, E. H. Sargent, "Colloidal quantum dot solids for solution-processed solar cells", *Nature Energy*, vol. 1, pp.16016, 2016.

[258] Z.-Y. Zhang, H.-Y. Wang, Y.-X. Zhang, *et al.*, "The role of trap-assisted recombination in luminescent properties of organometal halide $CH_3NH_3PbBr_3$ perovskite films and quantum dots", *Sci. Rep.*, vol. 6, pp.27286, 2016.

[259] C. Wang, B. R. Ecker, H. Wei, *et al.*, "Environmental surface stability of the $MAPbBr_3$ single crystal", *J. Phys. Chem. C*, vol. 122, pp.3513-3522, 2018.

[260] M. Barbato, M. Meneghini, A. Cester, *et al.*, "Influence of Shunt Resistance on the Performance of an Illuminated String of Solar Cells: Theory, Simulation, and Experimental Analysis", *IEEE Trans. Device Mater. Reliab.*, vol. 14, pp.942-950, 2014.

[261] K. Domanski, J.-P. Correa-Baena, N. Mine, *et al.*, "Not all that glitters is gold: Metal-migration-induced degradation in perovskite solar cells", *ACS Nano*, vol. 10, pp.6306-6314, 2016.

[262] S. Kim, S. Bae, S.-W. Lee, *et al.*, "Relationship between ion migration and interfacial degradation of $CH_3NH_3PbI_3$ perovskite solar cells under thermal conditions", *Sci. Rep.*, vol. 7, pp.1200, 2017.

[263] A. K. Jena, Y. Numata, M. Ikegami, *et al.*, "Role of spiro-OMeTAD in performance deterioration of perovskite solar cells at high temperature and reuse of the perovskite films to avoid Pb-waste", *J. Mater. Chem. A*, vol. 6, pp.2219-2230, 2018.

LIST OF PUBLICATIONS

Publications related to the dissertation:

- B. Su, V. Körstgens, Y. Yao, D. Magerl, L. Song, E. Metwalli, S. Bernstorff, P. Müller-Buschbaum, "Pore size control of block copolymer-templated sol–gel-synthesized titania films deposited via spray coating", *J. Sol-Gel Sci. Technol.*, vol. 81, pp.346-354, 2017.
- B. Su, H. A. Caller-Guzman, V. Körstgens, Y. Rui, Y. Yao, N. Saxena, G. Santoro, S. V. Roth, P. Müller-Buschbaum, "Macroscale and nanoscale morphology evolution during in situ spray coating of titania films for perovskite solar cells", *ACS Appl. Mater. Interfaces*, vol. 9, pp.43724-43732, 2017.

Further publications:

- Y. Yao, E. Metwalli, J.-F. Moulin, B. Su, M. Opel, P. Müller-Buschbaum, "Self-assembly of diblock copolymer–maghemite nanoparticle hybrid thin films", ACS Appl. Mater. Interfaces, vol. 6, pp.18152-18162, 2014.
- C. J. Schaffer, J. Schlipf, E. Dwi Indari, B. Su, S. Bernstorff, P. Müller-Buschbaum, "Effect of blend composition and additives on the morphology of PCPDTBT:PC$_{71}$BM thin films for organic photovoltaics", *ACS Appl. Mater. Interfaces*, vol. 7, pp.21347-21355, 2015.
- W. Wang, S. Pröller, M. A. Niedermeier, V. Körstgens, M. Philipp, B. Su, D. Moseguí González, S. Yu, S. V. Roth, P. Müller-Buschbaum, "Development of the morphology during functional stack build-up of P3HT:PCBM bulk heterojunction solar cells with inverted geometry", *ACS Appl. Mater. Interfaces*, vol. 7, pp.602-610, 2015.
- Y. Yao, E. Metwalli, B. Su, V. Körstgens, D. Moseguí González, A. Miasnikova, A. Laschewsky, M. Opel, G. Santoro, S. V. Roth, P. Müller-Buschbaum, "Arrangement of

maghemite nanoparticles via wet chemical self-assembly in PS-b-PNIPAM diblock copolymer films", *ACS Appl. Mater. Interfaces*, vol. 7, pp.13080-13091, 2015.

- Y. Rui, H. Xiong, B. Su, H. Wang, Q. Zhang, J. Xu, P. Müller-Buschbaum, "Liquid-liquid interface assisted synthesis of SnO_2 nanorods with tunable length for enhanced performance in dye-sensitized solar cells", *Electrochim. Acta*, vol. 227, pp.49-60, 2017.
- L. Song, V. Körstgens, D. Magerl, B. Su, T. Fröschl, N. Hüsing, S. Bernstorff, P. Müller-Buschbaum, "Low-temperature fabrication of mesoporous titania thin films", *MRS Advances*, vol. 2, pp.2315-2325, 2017.

Scientific report:

- B. Su, M. A. Niedermeier, M. Rawolle, P. Müller-Buschbaum, "Characterization of oxygen plasma-treated titanium dioxide surfaces with a foam like structure", *Lehrstuhl für Funktionelle Materialien, Annual Report*, 2012.
- B. Su, S. Bernstorff, P. Müller-Buschbaum, "Spray pyrolysis deposition of titanium dioxide with foam like structure for photovoltaic applications", *Lehrstuhl für Funktionelle Materialien, Annual Report*, 2013.
- B. Su, W. Liu, Y. Yao, G. Santoro, S. V. Roth, P. Müller-Buschbaum, "In situ growth study of gold nano domains on p3ht films", *Lehrstuhl für Funktionelle Materialien, Annual Report*, 2014.
- B. Su, V. Körstgens, Y. Yao, D. Magerl, L. Song, E. Metwalli, S. Bernstorff, P. Müller-Buschbaum, "Pore size control of block copolymer-templated sol-gel-synthesized titania films deposited via spray coating", *ELETTRA, Annual Report*, 2015.
- B. Su, T. Haeberle, M. Trunk, P. Lugli, P. Müller-Buschbaum, "Superstructuring titania films via nanoiprinting for photovoltaic applications", *Lehrstuhl für Funktionelle Materialien, Annual Report*, 2015.
- B. Su, V. Körstgens, Y. Yao, D. Magerl, L. Song, E. Metwalli, S. Bernstorff, P. Müller-Buschbaum, "Pore size control of block copolymer-templated sol-gel-synthesized titania films deposited via spray coating", *Lehrstuhl für Funktionelle Materialien, Annual Report*, 2016.
- B. Su, H. A. Caller-Guzman, P. Müller-Buschbaum, "Mathematical modeling of size distribution in wet spray coating", *Lehrstuhl für Funktionelle Materialien, Annual Report*, 2017.

Conference talks:

- B. Su, L. Song, J. Schlipf, "Hybrid perovskite photovoltaics", *E13 summer school. Lehrstuhl für Funktionelle Materialien. Obertauern, Austria*, 21 - 24 Jun 2016.
- B. Su, "Spray deposition study for titania films", *3rd internal biennial science meeting of the MLZ, Grainau*, 15 - 18 Jun 2017.
- B. Su, H. A. Caller-Guzman, V. Körstgens, Y. Rui, Y. Yao, N. Saxena, G. Santoro, S. V. Roth, P. Müller-Buschbaum, "Macro- and nano-scale morphology evolution during in situ spray coating of titania films for perovskite solar cells", *DPG-Frühjahrstagung, Berlin*, 11 - 16 Mar 2018.

Conference posters:

- B. Su, M. A. Niedermeier, M. Rawolle, P. Müller-Buschbaum, "Foam-like structures of titania films for application in hybrid photovoltaics", *DPG Frühjahrstagung, Regensburg*, 10 - 15 Mar 2013.
- B. Su, M. A. Niedermeier, M. Rawolle, P. Müller-Buschbaum, "Foam-like structures of titania films for application in hybrid photovoltaics", *SolTech Workshop, Würzburg*, 11 - 13 April 2013.
- B. Su, M. A. Niedermeier, M. Rawolle, P. Müller-Buschbaum, "Foam-like structures of titania films for application in hybrid photovoltaics", *DPG Frühjahrstagung, Regensburg*, 10 - 15 Mar 2013.
- B. Su, M. A. Niedermeier, M. Rawolle, S. Bernstorff, P. Müller-Buschbaum, "Foam-like structures of titania films for application in hybrid photovoltaics", *3rd Colloquium of the Munich School of Engineering, Garching*, 4 Jul 2013.
- B. Su, M. A. Niedermeier, M. Rawolle, S. Bernstorff, P. Müller-Buschbaum, "Foam-like structures of titania films for application in hybrid photovoltaics", *Nanosystems for Solar Energy Conversion, LMU Munich*, 24 - 26 Jul 2013.
- B. Su, Y. C. Rui, M. A. Niedermeier, V. Körstgens, S. Bernstorff, P. Müller-Buschbaum, "Pore size control of block copolymer-templated sol-gel-synthesized titania films deposited via spray coating", *DPG Frühjahrstagung, Dresden*, 30 Mar - 4 Apr 2014.

- B. Su, Y. C. Rui, P. Müller-Buschbaum, "Light harvesting structured titania films prepared by PDMS molds", *DPG Frühjahrstagung, Berlin*, 15 - 20 Mar 2015.

- B. Su, H. A. Caller-Guzman, V. Körstgens, Y. Rui, Y. Yao, N. Saxena, G. Santoro, S. V. Roth, P. Müller-Buschbaum, "Foam-like structure of spray coated titania films for perovskite solar cells", *5th Colloquium of the Munich School of Engineering, Garching*, 9 Jul 2015.

- B. Su, H. A. Caller-Guzman, V. Körstgens, C. J. Schaffer, Y. Yao, S. V. Roth, P. Müller-Buschbaum, "Titania network structures prepared via spray coating for photovoltaic applications", *DPG Frühjahrstagung, Regensburg*, 6 - 11 Mar 2016.

- B. Su, H. A. Caller-Guzman, V. Körstgens, C. J. Schaffer, Y. Yao, S. V. Roth, P. Müller-Buschbaum, "Titania network structures prepared via spray coating for photovoltaic applications", *4th International SolTech Conference in Munich, Munich*, 5 - 8 Apr 2016.

- B. Su, H. A. Caller-Guzman, V. Körstgens, C. J. Schaffer, Y. Yao, S. V. Roth, P. Müller-Buschbaum, "Foam-like structure of spray coated titania films for perovskite solar cells", *6th Colloquium of the Munich School of Engineering, Garching*, 7 Jul 2016.

- B. Su, H. A. Caller-Guzman, V. Körstgens, Y. Rui, Y. Yao, S. V. Roth, P. Müller-Buschbaum, "Morphology evolution of titania films during in situ spray coating for perovskite solar cells", *DPG Frühjahrstagung, Dresden*, 19 - 24 Mar 2017.

ACKNOWLEDGEMENTS

First of all, I would like to thank Prof. Dr. Peter Müller-Buschbaum for his warm welcome to his group at the start of my Ph.D. at Technische Universität München. Additionally, I want to thank him for giving me this exciting topic relating to the material sciences and photovoltaics, the nice discussions, and all the advice and suggestions throughout my Ph.D. study. Thanks to him for providing me chances to participate in beamtimes and conferences, which broadened my knowledge and improved my organizational experience.

For the beamtime experiments, I am grateful to my beamtime teams and beamline scientists: Dr. Volker Körstgens, Stephan Pröller, Dr. Martine Philipp, Dr. Christoph J. Schaffer, David Magerl, Johannes Schlipf, Markus Trunk, Lorenz Bießmann, Hong Xu, Prof. Dr. Stephan Roth, Dr. Gonzalo Santoro, and Sigrid Bernstorff. They offered lots of help and assistance to overcome the issues encountered during the beamtimes. Without their help, the beamtime experiments could not be efficiently done.

I want to thank Dr. Martin Niedermeier and Dr. Monika Rawolle, who have always provided help with patience, especially when I started my experiments. I want to thank the following people who were involved, in no specific order: Dr. Kuhu Sarkar, Erik Braden, Dr. Yuan Yao, Rui Wang, Dr. Ezzeldin Metwalli, Dr. Volker Körstgens, Johannes Schlipf, Nitin Saxena, Nuri Hohn, Dr. Shuai Guo, Lorenz Bießmann, Christoph Schaffer, Dr. Daniel Moseguí González, Franziska Löhrer, Senlin Xia, Dan Yang, Kun Wang, Sebastian Grott, Lucas Kreuzer, Tobias Widmann. I appreciate their extensive and helpful discussions, and their help over numerous experiments. For the teaching activities, I would like to thank Dr. Ezzeldin Metwalli and Dr. Volker Körstgens. It was my honor to work with them. Not only have my teaching skills improved, but my range of knowledge has also widened with their indispensable help.

I am grateful to have usage access to the instruments from cooperation groups: Rui Wang and Dr. Henrich Frielinghaus for their permission to work in the chemistry lab in Jülich Centre for Neutron science at the FRMII; Peter Weiser and Prof. Dr. Alexander W. Holleitner for the possibility to measure SEM and the permission to work in the clean room; Robin Nagel and Prof. Dr. Paolo Lugli for the possibility to use the nano-indenter for imprinting; Yu Tong, Florian Ehrat and Prof. Dr. Jochen Feldmann for TRPL measurements. Besides that, I want to especially thank Yichuan Rui and Hao Xiong, who provided huge efforts to help me figure out the tricks in the solar cells' fabrications.

Furthermore, I also want to thank my diligent master students: Wei Liu, Herbert A. Caller-Guzman and Markus Trunk. Their high motivation and excellent works contributed to the present thesis. Additionally, I want to acknowledge China Scholarship Council in offering me this scholarship.

For the proofreading of my thesis, I am sincerely grateful to Susan Lai, who carefully and patiently looked through the whole thesis. Also, I am indebted to Dr. Yuan Yao, Johannes Schlipf, Dr. Volker Körstgens, Nitin Saxena, Rui Wang for the scientific revisions. In addition, I want to thank Sebastian Grott, Tobias Widmann and Franziska Löhrer for the attribution of German abstract part in my thesis.

I have very much enjoyed working in the Lehrstuhl für Funktionelle Materialien. Thanks to all E13 colleagues, who created such an excellent working atmosphere. I am thankful to our secretaries: Susanna Fink, Marion Waletzki, and Carola Kappauf, who organized lots of group actives successfully, which are now my unforgettable memories, and also provided help on my enrollment and visa extension. So many happy memories were also created with Stephan Pröller, Dr. Martin Niedermeier, Dr. Kuhu Sarkar, Nuri Hohn, Johannes Schlipf, Nitin Saxena, Lorenz Bießmann, Sebastian Grott, and Shambhavi Pratap in our private activities. Thank them for the wonderful time we spent together, and for having made my life more fun and colorful. Also, I would like to thank Xiaohan Zhang, Wei Chen, Wei Cao, and Nian Li for the private time we shared.

Last but not least, I want to thank my family for supporting me when I met with difficulties and for always believing in me. Special thanks to my wife, Junmiao Li, for understanding and encouraging me throughout my whole Ph.D. period.